Design and deposition of $CaMoO_4$ as host for solar down-converters

Julie Nitsche Kvalvik

A thesis submitted for the degree of

Philosophiae Doctor (Ph.D.)

Department of Chemistry

Faculty of Mathematics and Natural Sciences

University of Oslo

January 2021

Series of dissertations submitted to the
Faculty of Mathematics and Natural Sciences, University of Oslo
No. 2398

ISSN 1501-7710

Cover: Hanne Baadsgaard Utigard.
Print production: Reprosentralen, University of Oslo.

Preface

This dissertation is submitted in partial fulfilment of the requirements for the degree of *Philosophiae Doctor* at the Department of Chemistry, Faculty of Mathematics and Natural Sciences, University of Oslo. The work was carried out at the research group for Nanostructures and Functional Materials (NAFUMA), between September 2015 and September 2020, except for when in parental leave. Dr. Per-Anders Hansen and Prof. Ola Nilsen have supervised the work.

Per-Anders and Ola, there is no way this thesis could be finished without you. Per-Anders, you are truly an excited person and I have never met anyone so passionate about his or her own field as you. That passion is contagious, and so is your cheerfulness and joy to share your knowledge. Ola, you are the most understanding and supporting person on the planet. Your response time is amazingly fast and you take all stupid and not so stupid questions seriously. You see every find as an opportunity, and that is great. When I saw an ALD system not behaving, only depositing on certain surfaces, you saw the chance to explore an area-selective system. I am so deeply grateful to both of you.

I am also very grateful to Øystein Evandt and his insight on Design of Experiments (DoE), that he is always more than willing to share. Moreover, a special thank you goes to Dr. David Wragg for his aid with Pawley refinements and to my co-author on Paper I, Jon Borgersen. Making the world's second smallest university logo would not have been possible without you. Augustinas Galeckas, co-author on Paper III, has my sincere gratitude for a swift response and aiding with various optical measurements. Thank you all.

During my many years at NAFUMA I have had a lot of nice colleagues and even shared office with many of you. I have probably been of the more talkative kind of office mate, but I think most of you managed ok. Thanks for making work-life good. Special thanks go to Kristian x2, Leva, Michael and Katja, for particularly good company.

The largest thank you goes to the people surrounding me. Luckily, that is a lot of people and I am so blessed to have each and every one of you. I am looking forward to times where we can all gather up for large family dinners again, although fitting 25+ people in our house is kind-of tight. Special thanks go to my parents for their endless support and babysitting. You have thought me persistence, perfectionism and hard work, and always taken for granted that I would be able to reach my goals. Thanks for having that belief, also at times where I lost it myself. A huge thank you goes to my in-laws for cheering and babysitting, including my always calm, positive and caring sister-in-law. I also want to thank the engineers in my family, particularly my grandfather, for inspiring me towards a scientific career. Kaja also deserves a huge thank you, simply for existing. Thanks for being my best friend since we started school – and staying with me until now when I finally finish my formal education.

Many times during this process, I have been told that pursuing a PhD whilst having three kids, is something you just don't do. It pisses of my inner feminist, but they do have a point, combining sleepless

nights, dreadful pregnancies and having to make it home before the kindergarten closes whilst pursuing a phd, is not always a primrose path. My favorite counterargument for this is that children give you the best possible mental timeouts from your work. And trust me, in this process, you need mental time outs. Leonora, you ask the cleverest questions and argue annoyingly well. Amelia, you are very passionate and so fast you always keep me on my toes. Edvin, you are the most dedicated two-year old engineer I have ever met. You are outright amazing people, all three of you. Thanks for keeping me distracted.

Lastly, my equally amazing husband deserve a huge thanks. Thanks for understanding my need to go into the lab a Saturday morning in July and for writing instead of spending my evenings with you. You are brave and stand up for others, always make me laugh and you outsmart me and point out my complete stupidity and other shortcomings on many levels on a daily basis (ability to find my car-keys, empty full trash-cans etc.). Thanks for letting me share everything with you and for your full endorsement of this project at a time where your own career is boosting. I am so very proud of you and love you from the bottom of my heart.

Abstract

Whilst silicon solar cells currently are approaching their maximum theoretical conversion efficiency, work is ongoing on many fronts to enhance their efficiency by means outside the classical framework. The efficiency of silicon solar cells in the UV-range of the sunlight is still particularly poor. One approach to enhance the response in the UV-range, is using down-conversion, also known as quantum cutting. In such manner, the energy of a highly energetic photon can be converted into two or more photons with less, but more appropriate energy for silicon based solar cells and increase the overall efficiency. Down-conversion systems are most often based on pairs of lanthanides, for example the very efficient Pr^{3+} / Yb^{3+} which is used here. While they can emit photons that suit silicon solar cells very well, they absorb UV-light poorly and require sensitization by a heavy absorber. However, such sensitizing open for loss of emitted photons through quenching and adds to the overall complexity. This is the foundation of the current thesis where we have tried to balance all these aspects in addition to nanoscale engineering to enhance the overall performance.

Sensitization without quenching is challenging in general and Pr^{3+} is particularly sensitive towards many hosts due to its many energy levels easing various quenching mechanisms. $CaMoO_4$ is launched as a promising host material for Pr^{3+}/ Yb^{3+}, as it absorbs well in the desired region, but is not known to lead to intervalence charge transfer (IVCT) known for other d_0 hosts. We have chosen atomic layer deposition (ALD) as the synthesis technique due to its abilities for conformal thin films, spatial control of where the lanthanide dopants are embedded in the host matrix and since it is a one-step approach, further doping is not required. Spatial control of the embedded dopants is essential as the required energy transfer for down-conversion is efficient only on the sub-nanometer scale.

The natural approach for developing complex oxides such as $CaMoO_4$: Pr^{3+}, Yb^{3+}, by ALD is to combine the binary processes and tune for the optimal composition. However, a compatible ALD process for MoO_x was lacking, as available processes either had special requirements or did not work at required temperatures, and had to be developed (**Paper I**). $MoCl_4O$ has proven to be a suitable Mo-source, in combination with O_3 and H_2O for deposition of complex oxides (**Paper II**), however, does not behave as a conventional ALD process when attempted as a binary oxide. For such a case, the process is area-selective and of numerous attempted substrates, MoO_x only deposits on soda-lime glass and LiF.

We were thus prepared for all types of outcomes when $MoCl_4O$ was combined with $Ca(thd)_2$ to deposit $CaMoO_4$. A path for deposition of $CaMoO_4$ was found with the aid of statistics – in the form of Design of Experiments (DoE) (**Paper II**). DoE methodologies are developed to maximize the amount of information from a given number of experiments, and is a useful tool when optimizing new processes, particularly when several parameters need tuning. Our study aims to serve as a guide on how to use DoE when developing complex ALD processes.

Finally, the complexity was increased by embedding Pr^{3+} and Yb^{3+} in the $CaMoO_4$ matrix (**Paper III**). Both the concentration of Pr^{3+} and Yb^{3+} and annealing parameters were found to highly affect the luminescence properties. We also have observed signs of direct energy transfer from $CaMoO_4$ to Yb^{3+}.

This work reached the goal of making $CaMoO_4$: Pr^{3+}, Yb^{3+} by ALD and studying its optical properties. Optimizing and implementing this coating on an actual silicon solar cell, remains a topic of further studies.

Contents

List of papers

Paper I:

Area-selective atomic layer deposition of molybdenum oxide

Kvalvik, J.N, Borgersen, J., Hansen, P.-A. and Nilsen, O. Journal of Vacuum Science & Technology A **38**, 042406 (2020)

Paper II:

Design of experiments approach to luminescent $CaMoO_4$ by atomic layer deposition

Kvalvik, J.N, Hansen, P.-A. and Nilsen, O. Journal of Vacuum Science & Technology A **38**, 052408 (2020)

Paper III:

Controlling the luminescence of $CaMoO_4$: Pr^{3+}, Yb^{3+} by atomic layer deposition

Kvalvik, J.N., Galeckas, A., Hansen, P.-A. and Nilsen, O. Manuscript ready for submission.

In addition to the papers that are a part of the thesis and listed above, I have also authored the following papers on atomic layer deposition, although not directly on the topic of the thesis.

LiF by atomic layer deposition – Made easy

Kvalvik, J.N, Kvamme, K.B, Almaas, K., Ruud, A., Sønsteby, H.H. and Nilsen, O. Journal of Vacuum Science & Technology A **38**, 050401 (2020)

Single-step approach to sensitized luminescence through bulk-embedded organics in crystalline fluorides

Hansen, P.-A., Zikmund, T., Yu, T., Kvalvik, J.N., Aarholt, T., Prytz, Ø., Meijerink, A. and Nilsen, O. Communications Chemistry **3**, 162 (2020)

1. Introduction

As I am writing this, Australia is on fire with over a trillion animals dead and thousands of people homeless already, Greta Thunberg has just been picked as the "Person of the Year" by *Time* magazine in 2019 for her school strikes for climate and my kids cannot play in the snow as January 2020 is unseasonably warm. The grey, dark Norwegian winter is staring at me from outside the window and I stare back, happy that I have at least tried to give a tiny, little contribution towards making the world a greener place. When I was writing these first sentences of my thesis, I did not know that the largest crisis in 2020 would not be the climate, but rather a virus. With every crisis comes opportunities, and we now have the chance and time to reconsider how we organize our energy economy, and a one-time shot to turn the tides. Even though our energy consumption and thus greenhouse gas emissions temporarily are lower, we cannot go back to our usual ways. This work addresses one of many solutions for more green energy.

Figure 1.1. Photography of Storfossen in Geiranger, Norway, steep and moist as so much of the country. Photo by Diego Delso.

Here in Norway where fish is abundant outside the oil-rich coastline and the combination of heavy topography and plenty of precipitation makes us rich in hydropower (Figure 1.1), it is hard to image that 850 million people worldwide are short on available energy[1]. This energy shortage cannot be met by increased usage of fossil fuels, as it leads to more greenhouse gas emissions. Finding more efficient green energy sources is thus a must. There are already plenty of renewable green options out there, including hydropower, biomass, geothermal power, wind power, wave/ tide power and last, but not least, solar power[2]. The International Energy Agency (IEA) forecasted in their last annual energy outlook that wind and solar power will be the most important green energy sources, and that electricity from photovoltaic solar cells will be the largest source of energy already in 2035[1]. For this to be the case, it is necessary that the photovoltaic cells increase in efficiency.

The most common photovoltaic cells today are the silicon solar cells. In fact, silicon oxide is the most abundant oxide on Earth[3], which is a very good starting point for a technology with large growth ambitions. Silicon, as other semiconductors, has a band gap (E_g), i.e. an energy range without any allowed energy level for the electron (energy levels are heavily discussed in Chapter 2). When sunlight with more energy than the band gap becomes absorbed by the solar cell, the electron gets excited from the valance band, E_v, to the conduction band, E_c, leaving behind a hole in the valance band (Figure 1.2). This excited electron is alone not sufficient to create a current, the electron-hole pair needs to be separated in space to prevent immediate recombination. This is where the p/n-junction comes into play. Silicon solar cells are typically homojunction cells (e.g. cells with the same material on both sides of the junction), where the properties are controlled by the type and level of doping. n-doping introduces local negative charge, and vice versa for p-doping. To induce n-type doping, the dopant has to be a donor, e.g. have more valence electrons than the host. For tetravalent silicon, this should be a dopant with five valance electrons, such as phosphorous. To p-dope silicon, trivalent boron can be used.

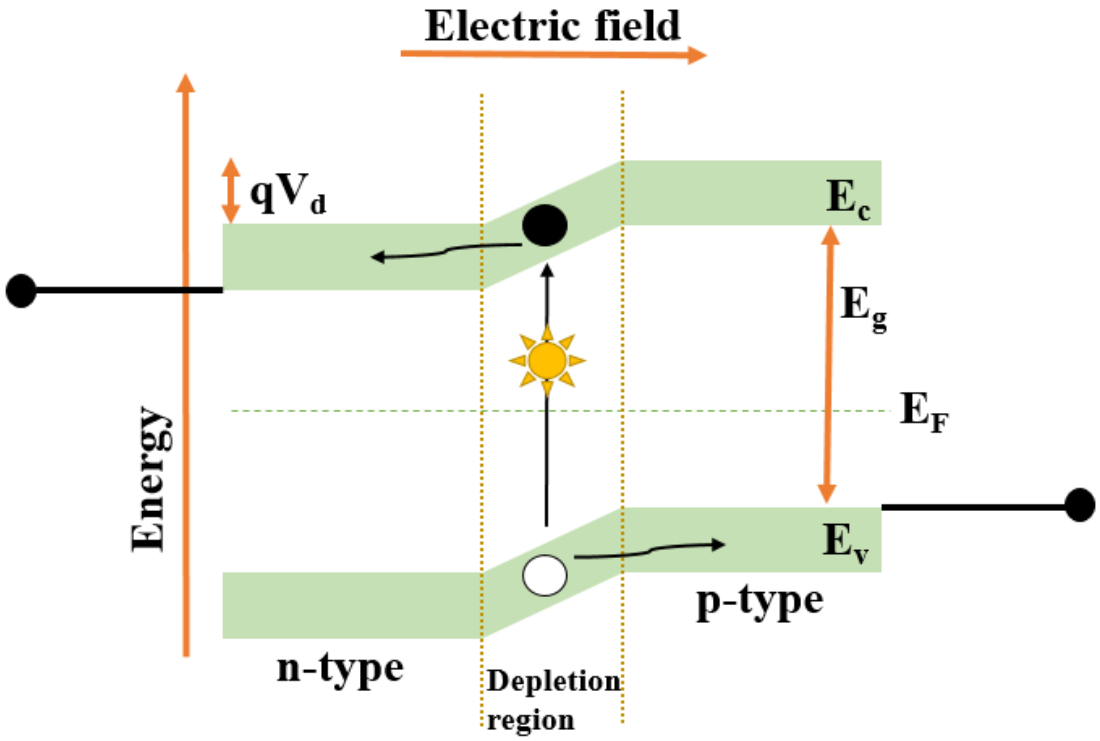

Figure 1.2. Schematic drawing of the p/n-junction of a (silicon) solar cell. E_F is the Fermi-level and qV_d is the amount of energy the bands are bent across the depletion region.

When a p-doped and n-doped region are combined, a depletion region is created. As the name suggests, the depletion region is depleted of carriers. The difference in local charges on each side of the junction creates an electric field across the depletion region. Thus, the bands are bent. When an electron is excited, the electron will be pulled towards the n-doped region and the hole will be pulled towards the p-type region. A current will now run through a wire if we connect it on each side of the solar cell. For

a more comprehensive introduction to photovoltaic cells, the reader is referred to the book by J. Nelson[4].

Massive research on silicon solar cells has provided significant advances in recent years, and we are in fact closing into the theoretical efficiency limit, the Shockley–Queisser limit[5], which is around 32 % efficiency for silicon solar cells. The Shockley-Queisser limit is applicable to single junction solar cells, takes radiative recombination into account as the only loss mechanisms and uses the standards AM 1.5 spectrum for the incoming sunlight. The blue lines in Figure 1.3 denotes advances for silicon solar cells with a current efficiency world record of 27.6 %. This also implies that in order to drastically improve solar cells, we have to reach beyond the conventional framework where the Shockley-Queisser limit rules.

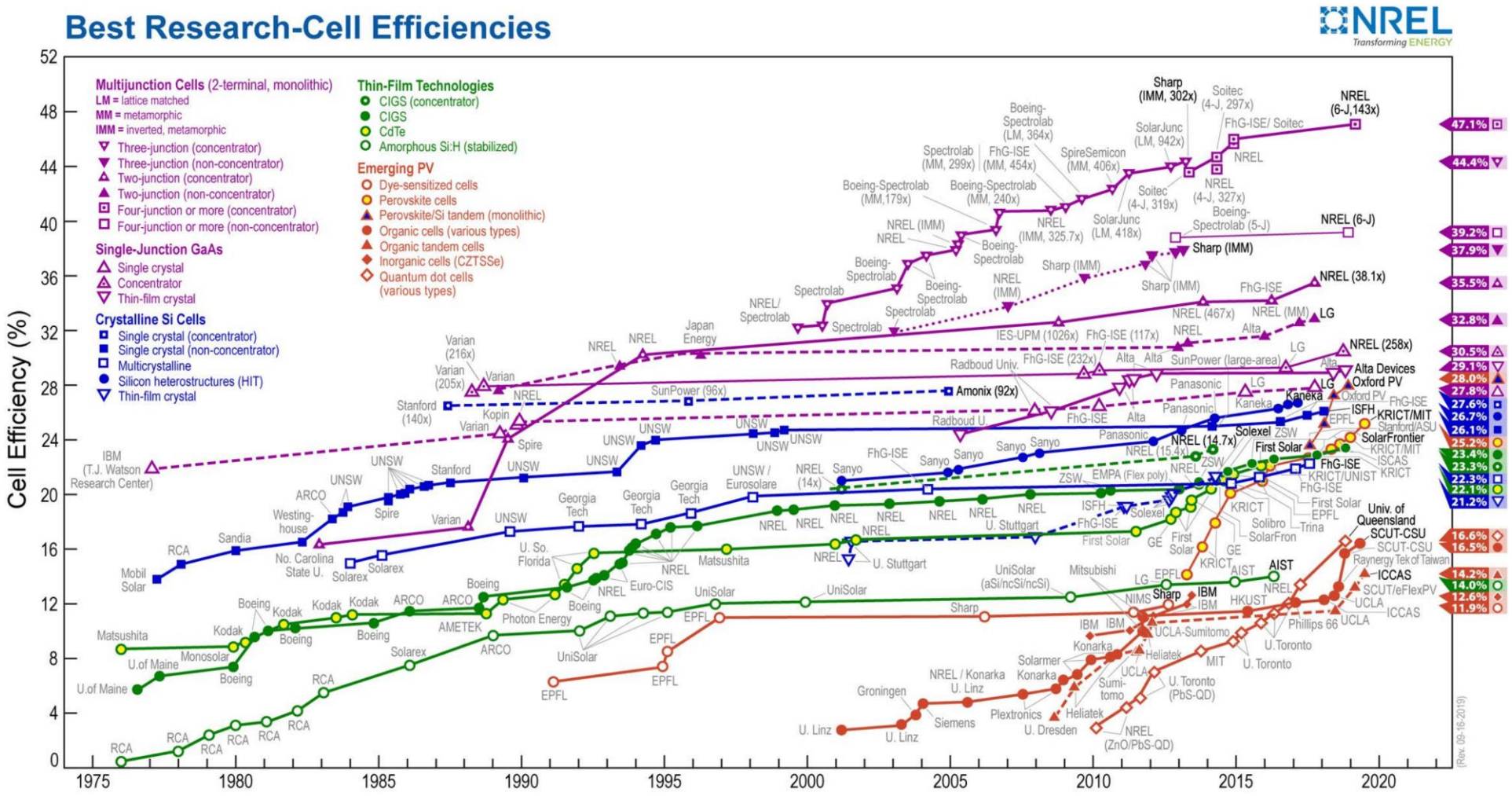

Figure 1.3. NREL's research-cell efficiency chart of 2019. The blue lines denotes conventional silicon solar cells[6].

The fundamentally most limiting factor for solar cells, is the relationship between the energy of the incoming electron and the band gap. The solar cell cannot utilize energy from sub-bandgap photons. Moreover, any excess energy beyond the band gap energy from photons with more energy than the band gap, will also be lost as heat, so-called thermalization losses (see chapter 2.3 – Radiative and non-radiative decay). Thermalization losses heat up the cells – making it even less efficient. The mismatch between incoming photon energy and band gap can be altered in two ways, either by tuning the band gap or by tuning the sunlight itself[7, 8]. There is a lot of current research on the first approach, for example on various types of tandem solar cells enabling the utilization of several band gaps simultaneously[9-16]. My work, however, is concerned with altering the sunlight itself. That can be done in two main ways[17], (i) up-conversion (UC) where the energy of several sub-bandgap photons is combined to a photon with sufficient energy to excite an electron across the band gap or (ii) down-conversion (DC), also called quantum cutting, where the energy of a photon with more than twice the energy to excite an electron across the band gap is split into two suitable photons. Down-conversion decrease thermalization losses.

The potential of either approaches are visualized in Figure 1.4, where the green fraction is the amount of the spectral irradiation that is efficiently utilized by silicon solar cells. The blue hatched areas correspond to energy that could be available if an efficient down-converter or up-converter was put onto the solar cells, being 149 W/m^2 or 164 W/m^2, respectively.

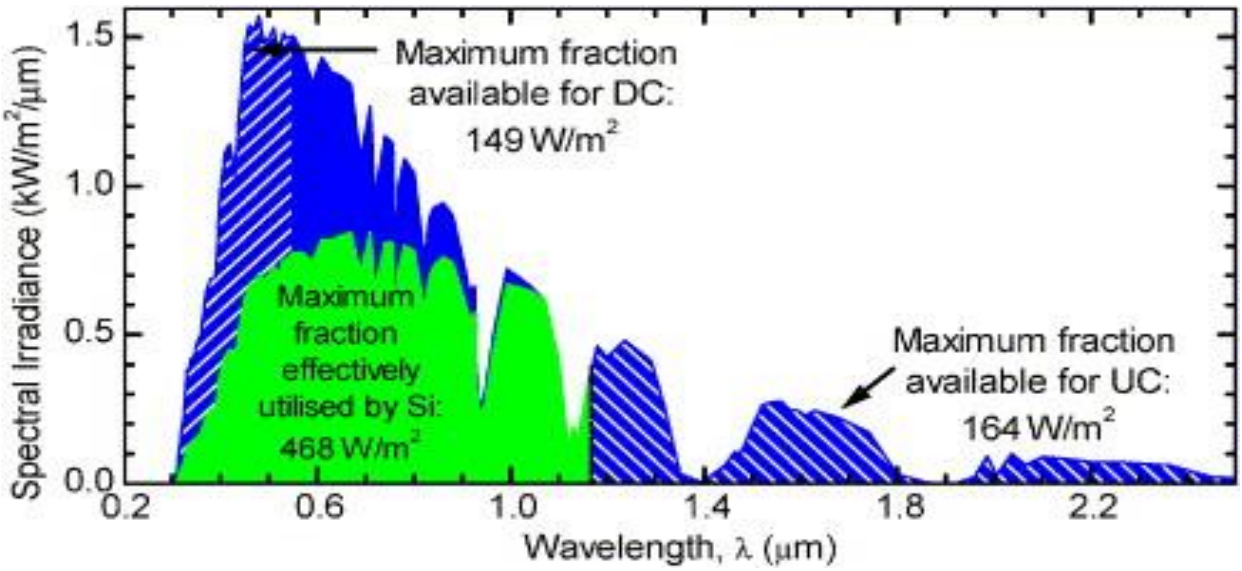

Figure 1.4. Spectral irradiance (AM 1.5) versus wavelength of incoming light, highlighting available energy for direct efficient use by silicon solar cells and available fractions for down-conversion and up-conversion[18].

The majority of down-conversion or up-conversion material systems consists of a host matrix doped with lanthanides. The well shielded partly filled f-orbital of the lanthanides gives rise to narrow, specific emissions – making them highly suitable for applications where tuning specific emission energies is key. The narrow absorption also mean that the lanthanides in general have a low absorption cross-section and thus weak absorption. A down-conversion system that does not absorb the light it is meant to convert, will have a negligible effect, and measures must therefore be taken to ensure sufficient absorption. Strategies to ensure strong absorption include usage of a highly absorbing host-matrix. This, and further strategies are discussed in subchapter 2.5.1 – Sensitization.

1.1 Aim of study

The overall aim of this work has been to make down-converting thin film coatings for silicon solar cells. The relative positions of the lanthanide dopants in the host matrix on a sub-nanometer scale strongly affect the efficiency of the down-conversion process. Moreover, a high local concentration of lanthanide dopants may lead to undesired quenching. To ensure the necessary required control to tune the interatomic distances of the dopants, atomic layer deposition (ALD) has been the synthesis method of choice. The layer-by-layer approach of ALD enables distribution of the lanthanide dopants in the matrix and can also place different lanthanide dopants in close proximity of each other. ALD is already heavily utilized for deposition of ultrathin back passivation layers within the solar industry[19, 20], meaning that important infrastructure is currently established on an industrial scale.

This work has focused on using $CaMoO_4$ as a host material[21]. There are already several studies both on the optical properties and synthesis of $CaMoO_4$[22-30], but few where $CaMoO_4$ is made as a thin film or where measures are taken to control the interatomic distances of the dopants.

In order to make complex oxides by ALD, the binary processes are usually combined. For deposition of $CaMoO_4$, this was challenging, as the available processes for deposition of molybdenum oxide were limited at the start of this project and not compatible with existing processes for CaO, without using customized heating equipment for the Mo-precursor. The first step to synthesize $CaMoO_4$ was therefore to develop a new ALD process for MoO_x. This process for MoO_x was then combined with a process for CaO to deposit $CaMoO_4$. Lastly, the $CaMoO_4$ films was co-doped with Pr^{3+}/ Yb^{3+} to make a down-converting film.

2. Optical properties and luminescence

To aid the discussion on the optical properties of the materials studied in this work, a general introduction to optical properties and luminescence, and down-conversion in particular, is presented in this chapter. First, a brief presentation of the most important interactions between light and matter is given. The chapter then proceeds to describe atomic energy states and their nomenclature, decay paths for excited states, energy transfer mechanisms and up- and down-conversion. The chapter ends by reviewing current down-conversion systems and discuss how these can be realized.

2.1 Interactions between light and matter

Matter is in classical Physics and Chemistry defined as any substance that has mass and takes up volume[31]. Matter can interact with electromagnetic radiation, the manifestation of the electromagnetic force, in various ways. This work is concerned with interactions between matter and wavelengths of electromagnetic radiation within the solar spectrum, which is about 220-2400 nm[32]. The part of the electromagnetic spectrum that is visible to the human eye, is shown in Figure 2.1. The three main interactions between light and matter are refraction, reflection and electronic transitions. Light can also simply be transmitted through the matter. This is why you can look through your window from your corona-quarantine, the visible light from outside is transmitted through it. This work is concerned with electronic transitions, in the form of absorption of light and then down-conversion, but we will start this chapter by a brief description of refraction and reflection.

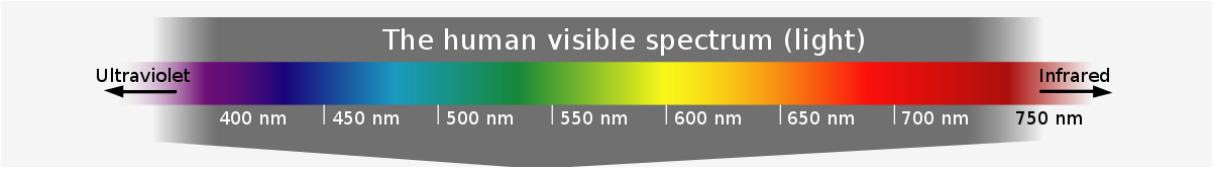

Figure 2.1. The human visible spectrum, a part of the electromagnetic spectrum. Adapted from [33].

Refraction is the change of direction of a wave when it passes from one medium to the other, and was first described by Willebrord Snell from Leiden in the 17th century[34]. Around 1660 the French Pierre de Fermat rewrote Snell's law into its current format we all know from our High School Physics classes, correctly assuming that light travels slower in media than in vacuum[35];

$$n_1 sin_{\theta_1} = n_2 sin_{\theta_2} \qquad \text{Eq. 2.1}$$

where n_1 and n_2 are the refractive indices of medium the light is travelling to and from, respectively, θ_1 is the angle of incidence and θ_2 is the angle of refraction. The refractive index is thus a description of how fast a light wave travels through the medium, where a high refractive index indicates that the light travels slowly. We now know that eq. 2.1 is a simplification, as it says nothing about the wavelength of the light, which the refractive index indeed is related to. We will return to this dependency later in the text, but first the relationship between refraction and reflection will be explored.

The relationship between refraction and reflection was also described by a Frenchman, namely Augustin Fresnel, but also the Scottish David Brewster contributed significantly [36]. For incident light that is travelling normal to an interphase, for example between air and glass, the reflectance, *R*, is given by;

$$R = \left|\frac{n_1 - n_2}{n_1 + n_2}\right| \qquad \text{Eq. 2.2}$$

From eq. 2.2 it becomes apparent that a large difference in refractive indices between two media in an interphase, will lead to a larger proportion of the light being reflected. The refractive index of silicon is around 3.45 and is huge in contrast to 1 for air, and an uncoated silicon solar cell will experience that around 30 % of the incident light is reflected[37]. Designing anti-reflective coatings is therefore of outmost importance to increase the efficiency of solar cells.

Even though the refractive index describes how the incident light is slowed when it enters a medium, it does not describe how the beam is weakened when it propagates through the medium. This is described by the attenuation coefficient, k, which is also dependent on the wavelength of the light beam. The attenuation coefficient is related to the absorption, $\alpha(\lambda)$ of the material, a key property to control for an efficient down-converter[38];

$$\alpha(\lambda) = \frac{4\pi}{\lambda} k(\lambda) \qquad \text{Eq. 2.3}$$

In order to further scrutinize how matter can absorb light, light has to be considered as a particle. The photoelectric effect, that metals will emit photoelectrons if they are illuminated by sufficiently energetic light, suggests that light has some particle properties. This was built upon by Louis de Broglie in 1924 when he proposed the de Broglie relation, claiming that any particle travelling with the linear momentum, $p = mv$, should have an associated wavelength, λ;

$$\lambda = \frac{h}{p} \qquad \text{Eq. 2.4}$$

where h is Planck's constant. We now call the «light particles» photons, and when light is absorbed by a material, the material actually absorbs the photon. This absorption is an electronic transition of the material and leads to an excited state of electrons in the absorber. The atomic energy states that govern what absorbance is possible and likely, are discussed further in subchapter 2.2.

2.2 Atomic energy states

If the atoms were not able to exist in several energy states, absorption would not have been possible. An understanding of these states is therefore an important aspect when studying absorbing solids.

2.2.1 Term symbols

The energy level of an atom is called a term, and the notation used to describe terms is called term symbols[39]. Term symbols occur in every scientific paper about luminescence and are therefore described in detail here. The term symbol is written as $^{2S+1}\mathbf{L}_{J}$*. Typically, they are used to describe energy transitions that result in luminescence. For example, in the current work we discuss the energy transitions concerning the $^3P_0$ level of Pr^{3+}.

The derivation of the term symbol is called Russell-Saunders (RS) coupling[40]. The first step of this derivation is that the spin angular momenta of each electron are combined. Then these momenta of the electrons are coupled to give an overall total angular momentum, L. It is written in upper-case roman letters, with the same letter as the atomic orbital;

L	0	1	2	3
	S	P	D	F

$^3P_0$ therefore describes the energy levels of electrons in the P orbital, with L = 1. In general, L arises from the orbital angular momentum numbers, l_1 and l_2, which in turn describe the shape of the orbital. L is derived using the Clebsch-Gordan series (Eq. 2.5) and is always a positive integer[41];

$$L = l_1 + l_2, l_1 + l_2 - 1, \ldots, |l_1 - l_2| \qquad \text{Eq. 2.5}$$

A high L means that the valance electrons are orbiting in the same direction, whilst a lower L point to the opposite conclusion. The next part of the term symbol comes from the spin angular momentum quantum number, S, but the multiplicity, 2S+1, is what occurs in the term symbol. A high multiplicity means that many electrons are spinning in the same direction. S is derived from individual spin angular momentum numbers, s_1 and s_2, using the Clebsch-Gordan series. In our example of $^3P_0$, S is 1, making the multiplicity, 2S+1 = 3. When the multiplicity is 3, we may call the term a triplet.

The total angular momentum number, J, is in turn derived from L and S, also using the Clebsch-Gordan series. J describes the coupling between the spins of the electrons and their orbit, also called spin-orbit coupling. A large J means that many electrons have spins in the same direction as their orbit. Each value of J is called the **level** of a term. Using the Clebsch-Gordan series to derive the possible J-levels for ^3P (L = 1 and S = 1), gives us J = 1+1, 1+1-1 or 1-1. This means that in addition to $^3P_0$, $^3P_1$ and $^3P_2$ are possible levels. Figure 2.2 summarizes this section.

* L is the total angular momentum number, S is the spin angular momentum number and J is the total angular momentum number derived from L and S.

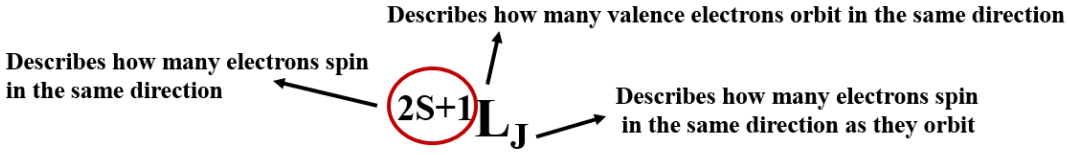

Figure 2.2. Summary of the meaning of 2S+1, L and J in the term symbol notation.

2.2.2 Stark sublevels

For each level, there are 2J + 1 states. These states are called Stark sublevels and are normally degenerate, i.e. they have the same energy. The Stark sublevels were discovered by Johannes Stark in 1913, as he observed splitting of spectral lines in electric fields[42]. Stark was awarded the Nobel Prize in Physics in 1919 for this discovery. The Stark sublevels are affected by crystal field splitting. This is illustrated for Eu^{3+} with a $[Xe]4f^6$ configuration in Figure 2.3. Take notice that these J-levels will be the same regardless of the host material, but that the transition rates between the levels and the crystal field splitting will differ.

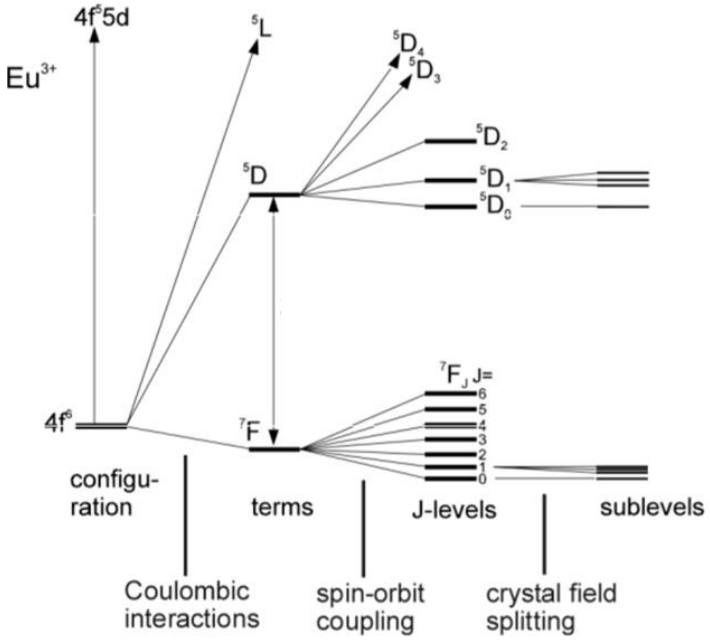

Figure 2.3. Energy levels of Eu^{3+} with a $[Xe]4f^6$ configuration, adapted and modified from [43].

2.2.3 Selection rules

A selection rule is a description about what electronic spectroscopic transitions, i.e. electrons changing from one state to another, are allowed or not. The selection rules are also sometimes referred to as transition rules, and stem from quantum mechanical formalism[39]. Even though many transitions are

labelled *forbidden*, that only means that the probability for these transitions is low[†]. There are also selection rules for other types of quantum mechanical transitions, such as between vibrational states, which are utilized when Fourier transformed infrared (FTIR) spectroscopy[44] or Raman spectroscopy[45] are performed, or for magnetic-dipole transitions seen when performing nuclear magnetic resonance (NMR) spectroscopy[46].

The first important selection rule for electron spectroscopic transitions, is the Laporte selection rule. The Laporte selection rule is related to inversion symmetry and applies only to centrosymmetric structures, and states that transitions are only allowed between molecular orbitals with different parities[47]. Parity can be labelled as either *gerade* (even in German) which means it is symmetric under inversion, and similarly *ungerade* (odd in German) if it is not symmetric under inversion. The parity of the symmetry point group can be looked up in standard character tables. All s and d orbitals are *gerade*, whereas p and f orbitals are *ungerade*. From the Laporte rule it also follows that s-s, p-p, d-d and f-f transitions all are forbidden, whilst for example d→f transitions are allowed. The Laporte rule is also applicable to complexes. Since octahedral complexes have an inversion center, these will be affected by the Laporte rule making transitions between orbitals with the same parity forbidden, but tetrahedral complexes will not be affected by the Laporte rule. Distortion of these octahedra lifts the Laporte rule and make for example f-f transitions, important for lanthanides, allowed. The fact that the Laporte rule can be lifted for distorted octahedral structures and fully lifted for tetragonally coordinated complexes, underlines the importance of the chosen host matrix.

A practical example of the difference between octahedral and tetrahedral complexes, is seen when $CoCl_2$ is dissolved in water, with or without addition of HCl. Dissolving $CoCl_2$ purely in water yields $[Co(H_2O)_6]^{2+}$, which has a pale pink color and is octahedrally coordinated. However, when HCl is also added, $[CoCl_4]^{2-}$ forms and the solution gets a deep blue color, similar to what is seen for the cobalt blue pigment used for centuries in glass staining, painting Chinese pottery and even on the façade of the Blue Mosque in Mazar-e-Sharif, Afghanistan (Figure 2.4).

[†] Theoretically the probability is zero, but that is in a perfectly symmetric, static, ideal world with no thermal vibrations, which we know is not the case in the real world.

Figure 2.4. The Blue Mosque in Mazar-e-Sharif in Afghanistan with cobolt blue used to color the facades. Photo by Sgt. Kimberly Lamb.

Even though it was just stated that d-d and f-f transitions are Laporte forbidden, they still occur to a large extent. Several conditions can lift the transition restrictions that the Laporte rule sets. Firstly, vibronic coupling can temporarily make transitions allowed. The Jahn-Teller effect has a similar influence[48]. Mixing of states may also allow Laporte forbidden transitions.

The other electronic spectroscopic selection rule, is the spin selection rule, sometimes called the Wigner rule, stating that the overall spin cannot change during a spectroscopic transition, $\Delta S = 0$. An illustration of the spin selection rule is seen below in Figure 2.5. Spin-orbit coupling, which is particularly important for heavier atoms such as the lanthanides, may lift the spin selection rule.

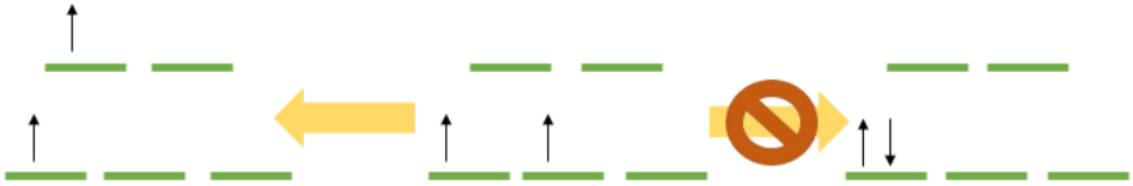

Figure 2.5. Illustration of an allowed (left) and a forbidden (right) electronic transition for a d_2 metal.

Charge transfer (CT) transitions are both Laporte and spin allowed. CT transitions are thus strong, and are also seen in $CaMoO_4$ between Mo and O as a metal-to-ligand charge transfer, explaining $CaMoO_4$'s strong absorption[49, 50].

2.2.4 Dieke diagram

The Dieke diagram is named after its inventor, G.H.Dieke. The original as first published is shown in Figure 2.6, and is a visualization of the various energy levels of the lanthanides[51]. The y-axis of the Dieke diagram is an energy axis. It is a useful tool for planning systems utilizing lanthanide transitions, where the relative energy levels between the lanthanides is important.

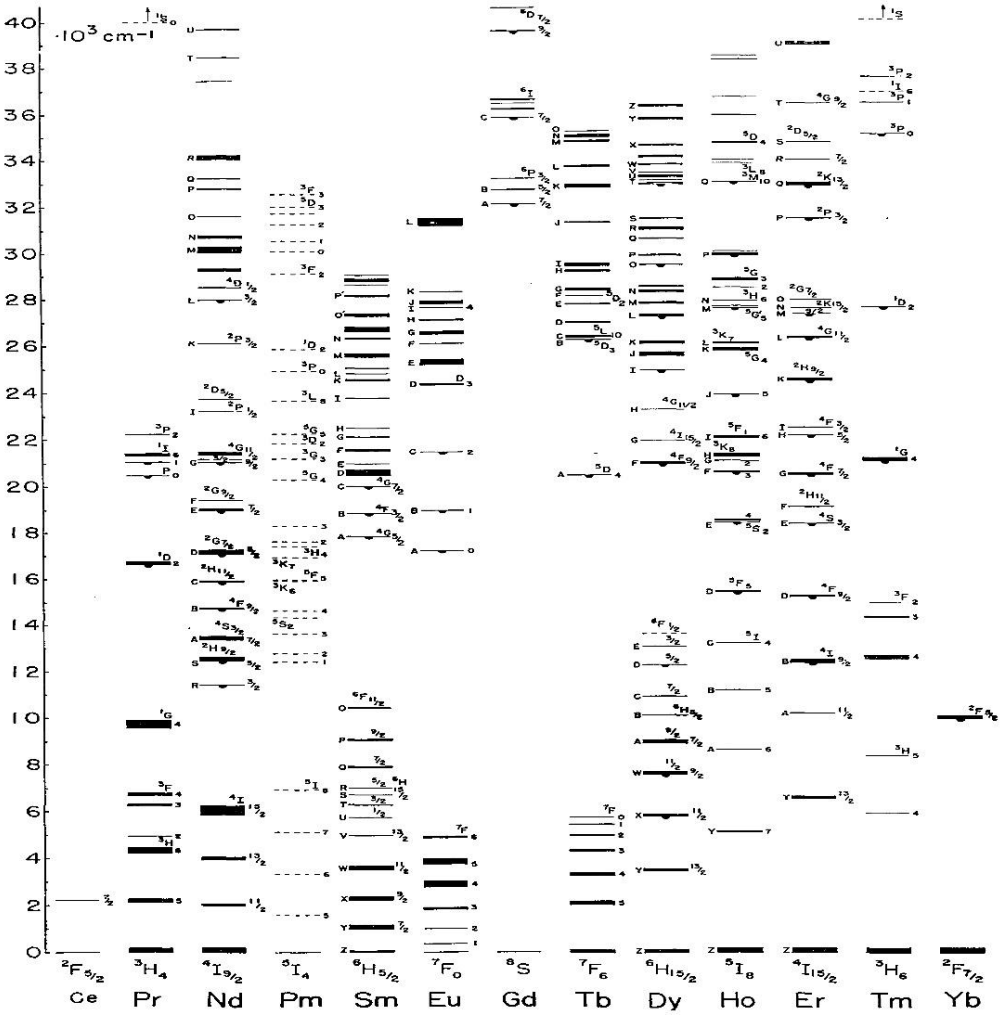

Figure 2.6. The Dieke diagram as first visualized by Dieke.

2.3 Radiative and non-radiative decay

When an atom absorbs light and adapts an excited state, this excited state will relax to a lower energy state. Broadly speaking, this can happen it two ways, either by radiative or non-radiative decay. If an atom relaxes by radiative decay, e.g. by emitting a photon, the material is luminescent. The average time an atom is excited before it relaxes by radiating a photon, is called the radiative lifetime[52]. The rate of the emission can be described by Fermi's Golden Rule, from which it becomes apparent that the transition rates are higher if the coupling between the initial and final states are strong. It is also dependent on the electronic densities of the surroundings, which in turn depends of the refractive index.

There are also other types of luminescence other than photoluminescence as described here, such as electroluminescence where the atoms are excited due to electric fields[53], mechanoluminescence which may occur when a material is subject to mechanical action[54] or chemiluminescene when light is emitted during a chemical reaction[55]. Devices utilizing luminescence include light emitting diodes (LEDs)[56, 57] and electroluminescent displays[58-60].

If a material relaxes by non-radiative decay, it relaxes by producing lattice vibrations, or phonons. The number of emitted photons versus the number of absorbed photons, is termed the quantum efficiency (QE). A QE of 100 % indicates that for every incoming absorbed photon, one photon is re-emitted. Take notice that the energies of the photons are not taken into account here, and some of the energy of the incoming photon is usually relaxed as lattice vibrations. This shift in energy between the absorbed and emitted light is called a Stokes shift and happens because of the parabola offset of the configurational coordinate, Q, between the ground and excited states (Figure 2.7). In certain cases, an anti-Stokes shift may also occur, where the emitted light has higher energy than the absorbed light.

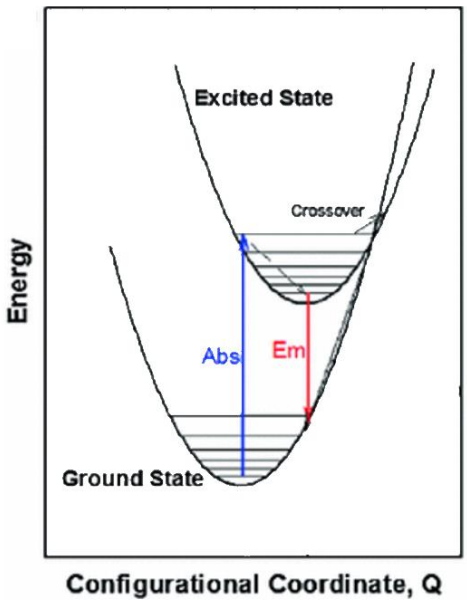

Figure 2.7. Configurational coordinate diagram showing the parabolic offset between the ground and excited states. Vertical transitions are radiative (absorption or emission of photons) whereas horizontal transitions are non-radiative (lattice vibrations). Adapted and modified from ref. [61].

The configurational coordinate describes the distance between the electron and core. The electron may only have energies at the parabolas shown[‡]. Vertical transitions are radiative, i.e. involve a photon, whereas horizontal transitions are lattice vibrations. If the lattice vibrations are large, that is at higher temperatures, the probability of non-radiative decay is larger. At larger Q values, after the crossover, radiative decay is not possible. According to the Frank-Condon principle, the electronic transitions take

[‡] Note that these parabolas are approximations of the bands and that the actual shape of the band may diverge from a parabola, especially far away from the local minima.

place much faster than what the massive nuclei can respond and the configurational coordinates thus remain constant during an electronic absorption and re-emission.

2.3.1 Judd-Ofelt theory

Judd-Ofelt theory, developed in 1962, describes the spectroscopic intensities of transitions of 4f electrons (e.g. the lanthanides) in both solids and solutions, and was in fact the first theory to properly describe the sharp spectra of the lanthanides[62, 63]. The theory is non-relativistic and assumes a static, free-ionic system. Static refers to that although the impact of the surrounding ligands on the central atom is taken into account, the central atom's effect on the surroundings is neglected[64]. With the computer power of today, Judd-Ofelt theory can be readily used to estimate spectra for the f ↔ f transitions. This information may in turn be utilized when planning new optical conversion systems. Note that Pr^{3+} is not as well described by Judd-Ofelt theory as the other lanthanides, with sometimes large deviations between calculations and observed spectra. It is explained by a small energy difference between the $4f^N$ and $4f^{N-1}$ 5d levels[65, 66].

2.4 Energy transfer

The energy of the absorbed light by localized states may travel within the absorbing material. These processes are called energy transfer. Energy transfer is essential for down-conversion systems, which is the main objective to synthesize in this thesis. There are two important energy transfer mechanisms for luminescent materials, Förster resonance energy transfer (FRET)[67] and Dexter energy transfer, also called collisional energy transfer[68] (Figure 2.8). As the name suggests, collisional energy transfer happens when molecules collide. More specifically, the wave functions of the involved orbitals must overlap. As lanthanides have well-shielded f-orbitals, this is unlikely to happen, and will not be considered further. FRET is caused by a long-range dipole-dipole coupling and is a non-radiative process. FRET is moreover dependent on the spectral overlap between the emission spectrum of the donating species and the absorption spectrum of the absorbing species. For practical purposes, it is also vital that transition rate is proportional to $1/R^6$, where R is the distance between the species. Thus, FRET can only occur up to a few nm and mostly between neighboring species. Synthesis approaches that enable precision of where the lanthanide dopants are in the host matrix, are therefore very important.

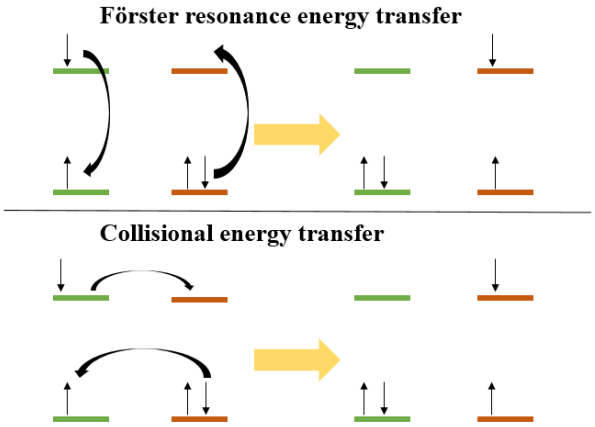

Figure 2.8. Illustration of the two types of energy tranfer; Förster resonance energy transfer (FRET, top) and collisional energy transfer (bottom).

2.4.1 Concentration quenching

Another important aspect with energy transfer, is that very efficient energy transfer may lead to quenching of the excited state, through phenomena called concentration quenching[69]. For higher concentrations of excited dopants, such as lanthanide ions, there is a higher chance that a neighboring species is of the same type. In these cases, the energy may transfer by FRET, between many equal lanthanides ions until it is transferred to a defect, such as grain boundary or a surface, where the excited state relaxes non-radiatively (Figure 2.9). Concentration quenching also includes quenching through cross-relaxation possible for Pr^{3+} among others.

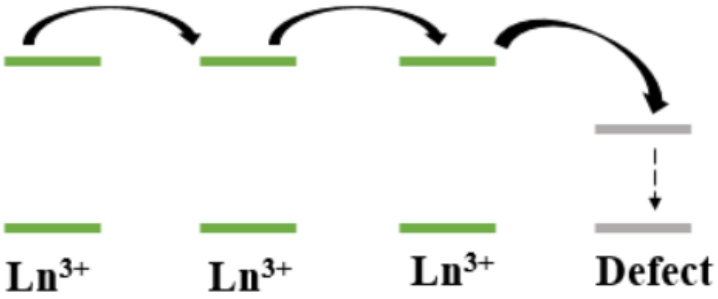

Figure 2.9. Concentration quenching where a high concentration of Ln^{3+} increases the chance of the excited state to find a defect where it relaxes non-radiatively, quenching the excited state.

When designing efficient optical systems with excited lanthanides, it is thus very important to consider the doping concentrations. A too low doping concentration makes it unlikely for the light absorbed by the host to migrate to a lanthanide ion, and also for a lanthanide to transfer energy to another lanthanide, but a higher doping level increase the chance for concentration quenching. Concentration quenching also highlights that defects play a role in quenching, and that well crystalline samples often are preferred. For example, for Eu^{3+}-doped Gd_2O_3 the maximum photoluminescence is found when 3 % Eu^{3+} is

used[70]. Both decreasing and increasing the doping level, reduces the luminescence for this system. Since the Eu^{3+} is inserted at a site without inversion symmetry, the Laporte forbidden $^5D_0 \rightarrow {}^7F_2$ transition is also seen here. The same effect is seen for $CaMoO_4:Pr^{3+}$ in **Paper III**, where using 1 % Pr^{3+} yields the most luminescent samples.

2.5 Up- and down-conversion

Up- and down-converting materials either splice or cut the energy of the incoming photons. In an up-conversion (UC) system the energy of two or more incoming photons is merged, before emission of a more energetic photon[71]. For down-conversion (DC), the opposite process takes place and the down-converting material is thus often referred to as a quantum cutter. A third type of spectral converters are down-shifting materials, where the energy of the emitted photon is lower than of the incoming photon, similar as for down-conversion[72, 73]. However, for down-shifting only one photon is emitted per incoming photon.

In this work, the aim has been to make a down-converting thin film. Down-conversion can occur using only one type of lanthanide ion that stepwise relaxes by emission of photons. For down-conversion with only one type of lanthanide to happen, the lanthanide has to be able to exhibit cascade emission[74]. Since this has not been realized for relevant energies to enhance performance of silicon solar cells, this process will not be considered further, although it is very efficient.

The other processes for down-conversion involve a lanthanide pair, termed a donor and an acceptor. The two processes are cross-relaxation and co-operative energy transfer (CET, Figure 2.10). Since cross-relaxation is a first order process and CET is a second order process, cross-relaxation will dominate if it is possible. This also makes sense when considering the surroundings of the donor in the host matrix. For CET to occur, two acceptors need to be in close enough proximity for FRET to be efficient, whilst only one acceptor is required for cross-relaxation. When down-conversion is used to enhance the performance of silicon solar cells, ytterbium is almost exclusively the acceptor responsible for the emission from the down-converter, since the $^2F_{5/2} \rightarrow {}^2F_{7/2}$ transition of Yb^{3+} has a well matching energy for the band gap of silicon solar cells. Moreover, as we can see from the Dieke diagram in section 2.2.4, this is the only possible transition for Yb^{3+}.

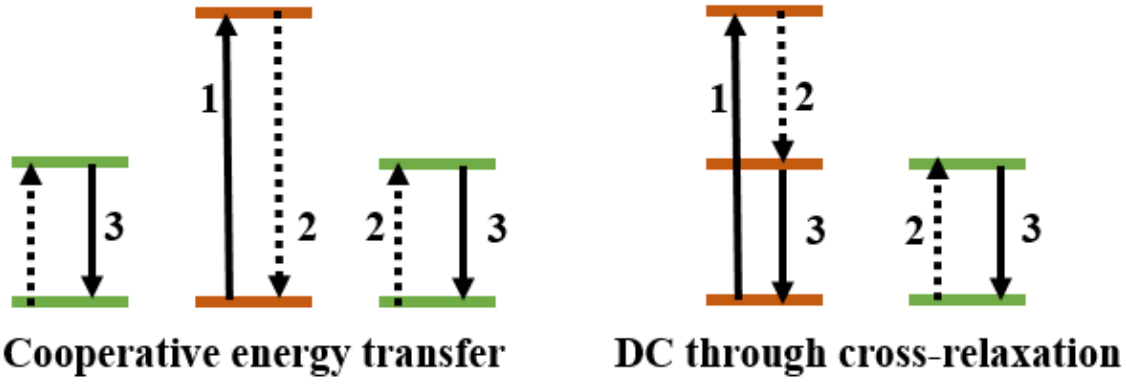

Figure 2.10. Visualization of the two common down-conversion mechanisms involving a lanthanide pair. Red energy levels refer to the donor, whereas green levels refer to the acceptor. Full arrows pointing upwards indicate absorption, whereas full arrows pointing downwards indicate relaxation by emission of a photon. Dotted arrows indicate energy transfer. The numbers refer to the order of the processes.

As donor, many of the lanthanides have been used. There are moreover examples of direct transfer from the host material to Yb^{3+}, which has been claimed to lead to down-conversion[75]. This claim has also been made for Yb^{3+} in $CaMoO_4$, but the articles lack evidence thereof, only showing that energy transfer is indeed taking place[76, 77]. Since the donor must be able to exhibit cascade emission for cross relaxation to take place, this is usually achieved with either the Er^{3+}/ Yb^{3+}[78, 79] or Pr^{3+}/Yb^{3+}[80] lanthanide pairs. The examples of CET are more plentiful and include Tb^{3+}[23, 81-86], Nd^{3+}[87], Tm^{3+}[88, 89], Eu^{2+}[90], Mn^{2+}[91] and Ho^{3+}[92] as donors, all with Yb^{3+} as acceptor. Of these pairs, Tb^{3+}/ Yb^{3+} is particularly extensively studied. Further note that it has been showed by Monte Carlo simulations that Ce^{3+}/ Yb^{3+} is not able to exhibit CET[93], only down-shifting, despite several reports of it[94, 95]. In ref. [96] De la Mora et al. give a comprehensive overview of available material systems for down-converters.

2.5.1 Sensitization

Another vital aspect when designing optical conversion systems, is to ensure that the material absorbs enough of the light it should convert. It does not actually matter much if each incoming and absorbed photon yields two emitted photons – if most of the incoming light is not absorbed at all. Strategies to achieve strong absorption in the desired wavelength region, are termed *sensitization*. Typically, this has been through the use of an absorbing host matrix – host-sensitization. Many materials have been studied for this, often d_0-oxides such as $CaMoO_4$ used in the current work or various vanadates[97-99]. An important parameter of the chosen host matrix in addition to the band gap/ absorbing energy range and absorption strength, is its maximum phonon energies. If these are high, there is an increased probability of non-radiative decay and thus quenching of the desired excited states.

In addition to using an absorbing host, sensitization can also be achieved by co-doping with a strongly absorbing species – such as Bi^{3+}[100, 101], Ce^{3+}[95] or Eu^{2+}[90].

More recently, organic dyes have been reported in sensitization of down-converters and not only for the solar cells themselves, in so-called dye-sensitized systems. Reported used dyes to enhance down-conversion so far include UV-blue absorbing Coumarin[102], fluorescein isothiocyante[103] and a dicyanostilbene derivative[104]. This field is still in its infancy, as it requires advanced synthesis, combining several material classes in a controlled manner. All the investigated systems so far have been on the form of nanoparticles with dyes anchored onto them, but these kinds of systems could potentially be realized through the usage of ALD (Chapter 3). When using ALD, both organics and inorganics may be incorporated in a layer-by-layer manner, also providing the desired positional control of the dyes[105]. Moreover, concentration quenching for the dye itself may also occur. For wet-chemical syntheses, this can be solved through dilution. Regardless if a wet chemical or vacuum-based method is used, strategies for dilution is in essence about reduction of the number of available seats for the dye to adhere or reduction of the number of available dye molecules. Solving this by using ALD, or other vacuum-based techniques, is so far more exotic, but simultaneous pulsing of the absorbing dye and another low-phonon energy organic precursor, could be possible. We also know that larger ALD-precursors often do not pack closely on the surface due to steric hindrance and this effect could be exploited to dilute the dyes. A drawback when using dyes, is that the dyes may easily quench the excited lanthanides, as the phonon energies for vibrations between C and H are high, and thus exact distance control between the dye and lanthanide is crucial.

2.5.2 The Pr^{+3}/ Yb^{3+} down-conversion pair

In the current work, the Pr^{3+}/ Yb^{3+} down-conversion pair has been investigated (Figure 2.11). It is chosen since it is the most well-studied pair exhibiting down-conversion through cross relaxation, as this is a first order and thus more likely process than CET. Moreover, this down-conversion process is very efficient[106]. From the fact that Pr^{3+} may exhibit cascade emission, it also follows that it has many energy levels. This will in turn increase the probability of non-radiative relaxation. From this it follows that sensitization of Pr^{3+} by organic dyes without making it even easier for the excited state to quench, is difficult.

Pr^{3+} is prone to metal-to-metal transfer quenching, also known as intervalence charge transfer (IVCT). This may occur when Pr^{3+} is embedded into a d_0 host, such as titanates, niobiates and vanadates[107-111]. It efficiently quenches the $^3P_0$ level required for use in a down-converter for silicon solar cells. Luckily, $CaWO_4$/ $CaMoO_4$ show promise as hosts for Pr^{3+} with low loss due to quenching through the IVCT state[112, 113]. The Pr^{3+}/ Yb^{3+} down-conversion pair has already been realized in $Gd_3(Al, Ga)_5O_{12}$[114], $LiYF_4$[106] and YF_3[80]. There are moreover a few reports on using organic dyes to sensitize the Pr^{3+}/ Yb^{3+} couple, most successfully done with Coumarin on the surface of $NaYF_4$: Pr^{3+}, Yb^{3+} nanoparticles[102].

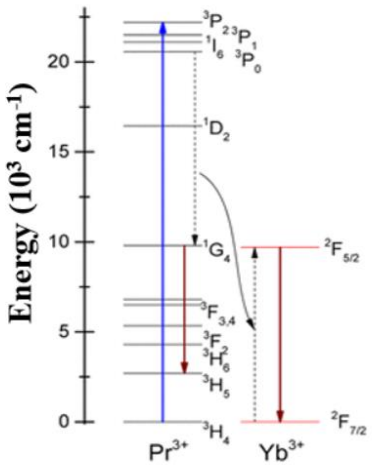

Figure 2.11. Energy level diagram, also known as Jablonski diagram[115] of down-conversion through cross-relaxation with Pr^{3+} as donor and Yb^{3+} as acceptor. Adapted and modified from ref. [114].

3. Atomic layer deposition

This chapter will give a brief account of the history and basic theory of atomic layer deposition (ALD), which is the synthesis method used to make the materials in this work. As this work encounters both area-selective ALD (AS-ALD), oriented growth and develops a new multicomponent ALD-process, these topics are also included and emphasized here.

3.1 History and basic theory

The first reports of ALD came from two independent sources during the Cold War who had no access to each other's work[59]. It was both reported from Soviet researchers in the 1960-70s[116] and patented by Finnish T. Suntola and J. Antson in 1974[117]. The first application for thin films deposited by ALD was as electroluminescent displays based on ZnS:Mn, were uniform coating over larger areas was required[118]. These were later doped with various lanthanides, such as Tb^{3+}[119] and Pr^{3+}[120] for color variations. ALD is classified as a subgroup of chemical vapor deposition (CVD) technique as it is based on chemical reactions, in opposition to physical vapor deposition (PVD) techniques. ALD has a supreme thickness control in comparison to other deposition techniques due to its cyclic, sequential nature. When ALD is performed, the reactant molecules (or precursor as we usually call it) are pulsed sequentially into the reaction chamber containing the substrates, with a flushing (purge) with an inert gas (typically N_2 or Ar) in between the pulses. The precursor molecules are chemisorbed on the surface of the substrate and saturate. For many precursors, exposure in the magnitude of a second is sufficient to saturate the surface. Purging removes the excess precursor. When the next precursor is pulsed, it reacts with the first precursor already present on the surface. To make a layered structure, it is preferable that the precursor has at least two reactive sites. The process is repeated a number of times to produce the desired film thickness. The process is visualized for the trimethylaluminium and water process to deposit Al_2O_3 in Figure 4.1. Besides an initial nucleation delay on the surface, the deposited film thickness should ideally be linear with the number of cycles, making it straightforward to control film thickness with nanometer precision. Typical deposition temperatures for an ALD-process range between 150 ^oC to 450 ^oC, giving a low thermal budget. A disadvantage is that ALD-processes generally are quite slow. The rate of an ALD-process is denoted by the growth rate per cycle (GPC), often given in pm/cycle, Å/cycle or nm/cycle. The GPC is completely process dependent, but often falls into the range of 5 to 300 pm per cycle[121].

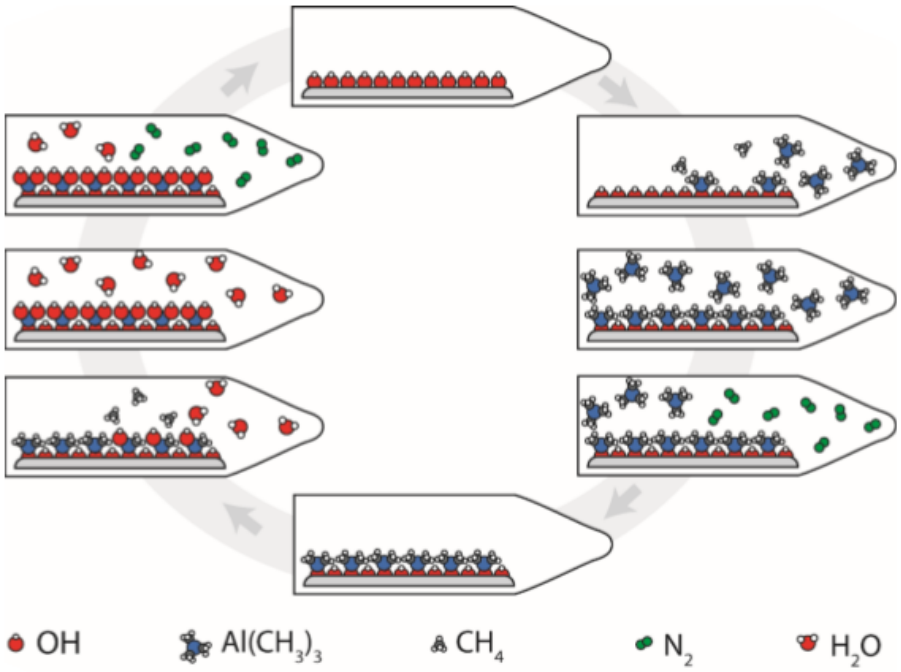

Figure 4.1. A visualization of the trimethylaluminium and water ALD-process with N_2 as the inert carrier gas, to deposit Al_2O_3 thin films. Adapted from ref.[122].

Prerequisites for a chemical to be useful as an ALD-precursor is that it should not react with itself and that it is volatile and thermally stable. Moreover, the precursor must (obviously) react with the other precursor to obtain the desired product. ALD-precursors used in this current work include gases such as O_3, liquids such as H_2O, solid powders that require heating as $Ca(thd)_2$ and solids that can be kept at room temperature as $MoCl_4O$.

Many ALD-processes exhibit a so-called "ALD-window". An ALD-window is a temperature range where the GPC remain relatively constant as a function of deposition temperature. At deposition temperatures below the ALD-window, the GPC may be reduced due to slow kinetics or higher due to condensation of the precursors. Similarly, higher temperatures than the ALD-window may lead to increased growth due to decomposition or decreased growth due to desorption of the surface species[123].

ALD is already used in a range of applications, the first was for deposition of ZnS phosphors for electroluminescent displays[60]. Other applications include deposition of Al_2O_3 as surface passivation layers on c-Si solar cells[124], Pt catalyst on solid oxide fuel cells[125] and HfO_2 for gate dielectrics[126].

3.1.1 Experimental setup

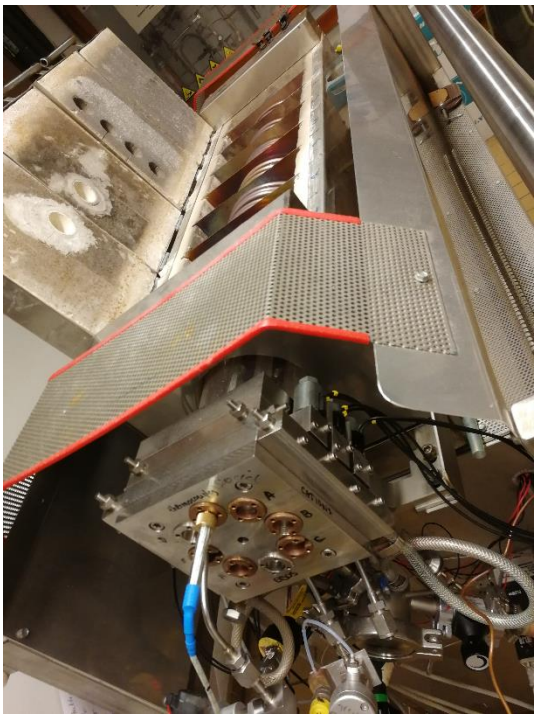

Figure 4.2 The F-120 ALD reactor in which all of the thin films in this thesis are deposited.

The ALD experiments in this work have all been conducted using a F-120 ALD reactor from ASM Microchemistry, a conventional thermal ALD reactor (Figure 4.2). The F-120 reactors are excellent research tools, as they can have up to six precursors used at a time kept at different temperatures. In **Paper III** of this work, the F-120 was really pushed to the limit, when six precursors were used simultaneously. The reactor has a temperature gradient towards the reaction zones, and choosing an appropriate gradient is vital to have appropriate sublimation temperatures for the various precursors.

3.1.2 Post-deposition treatment

In many cases, thin films deposited by ALD require post-deposition treatment to attain the desired properties, often a crystallographic phase required for specific applications. A more exotic example found in our group, was the need to anneal UiO-66 metal-organic frameworks (MOFs) with acetic acid vapor after deposition in order to induce the desired crystallographic phase[127]. In the current work, simple post-deposition annealing in air has been performed. This has been done using rapid thermal processing (RTP), a tool commonly used in our group[128, 129]. RTP uses lamps to heat the samples and was originally developed to anneal silicon wafers in the semiconductor industry, as it has a much more limited thermal budget than traditional furnaces[130]. In addition, RTP annealing is considered reproducible. How much the sample is actually heated will depend on how the sample absorbs the light emitted from the lamps heating it. Since the instrument is set up for silicon wafers, which is also the substrates mainly used in this work, this is not considered as a limitation for the current application. Here, a MTI - UL Standard Compact RTP with halogen lamps has been used.

3.2 Substrate dependency

3.2.1 Area-selective atomic layer deposition

The idea to actively use the differences in nucleation of the thin films on various substrates as means to selectively deposit on a growth surface and not on the non-growth surface by atomic layer deposition,

has been around for about 15 years[131]. For CVD it was proposed already in 1993[132]. Lately, the concept has gained more momentum, as the resolution limit for lithography for semiconductor devices is approaching and edge-placement errors are starting to dominate, despite extreme ultraviolet lithography (EUV)[133] soon being available in high-volume manufacturing. This has led to a search for good bottom-up approaches that can both deposit conformally with sub-nanometer precision and only deposit on the selected growth surfaces to avoid additional later etching steps[134]. Area-selective atomic layer deposition (AS-ALD) seems to be the most promising approach to achieve this so far. In contrast to traditional lithography methods that rely on physical properties, AS-ALD uses chemical information about composition and surface termination that by nature is on an atomic scale already.

Generally, AS-ALD systems can be categorized as either *inherent*, *activated* or *passivated*. For inherent systems, no extra measures are taken to promote the selectivity. An example of an inherently selective system is $MoSi_x$ that deposits selectively on silicon, but not on silicon nitride or silicon oxide[135]. Activated systems include usage of plasma[136], electron beam[137], catalysts[138] or other measures to promote deposition on only the growth surface, such as simply choosing the right substrate containing activation ions diffusing into the structure, which was the case for the $MoCl_4O$ + (H_2O + O_3) process described in **Paper I**. The most widely used method to obtain AS-ALD is to use a passivation strategy. Usually a blocking layer is employed. Lithography is then performed on the blocking layer to obtain the desired pattern with growth and non-growth areas. The blocking layers are often self-assembly monolayers (SAMs)[139, 140]. One challenge with using SAMs is that they may not be compatible with energetic co-reactants like ozone[141]. The last approach to AS-ALD is to include etching steps in the process to etch back all the undesired material deposited on the non-growth surface. This will also etch the material on the growth surface, but since the film is thicker here, some material will still be left in the desired area[142, 143].

A figure of merit to quantify how good an AS-ALD process is, is the selectivity, S. The selectivity, S, is defined as the amount (or rate) of one product relative to the total amount (or rate) of all products formed[144]. It can be calculated from experimental data, using common characterization techniques such as spectroscopic ellipsometry or imaging techniques, like scanning electron microscopy. The selectivity of a process will vary with the number of cycles used.

G. Parsons showed last year (2019) how AS-ALD processes can be modelled using the Johnson-Mehl-Avrami-Kolmogorov model, often just referred to as the Avrami-model[144, 145]. The Avrami-model describes isothermal nucleation and phase change as a function of time. It is originally made for 3D-systems, but G. Parsons shows that it is applicable for modelling 2D thin film growth also. The model uses the number of nucleation sites on the starting surface, $\widehat{N}$, the nucleation generation rate, $\dot{N}_0$, the characteristic number of cycles for nucleation incubation, v_d, and the growth rate, $\dot{G}$, as its input parameters. In contrast to O. Nilsen's previous model of island growth, which is based on geometrical

principles, the Avrami model assumes that the nucleation sites are points with no size and are randomly distributed across the surface[146]. The model enables quantitative comparison of AS-ALD results in between processes. Figure 3.4 shows two cases of nucleation and film growth modelled by the Avrami-model; case *a* with nucleation sites present on the starting surface, but no generation of new sites, and case *b* with no nucleation sites present from the start, but nucleation sites being generated throughout the process. In an ideal AS-ALD-world, the growth surface should have many nucleation sites from the start and new sites should be easily generated immediately. The opposite should be the case for the non-growth surface.

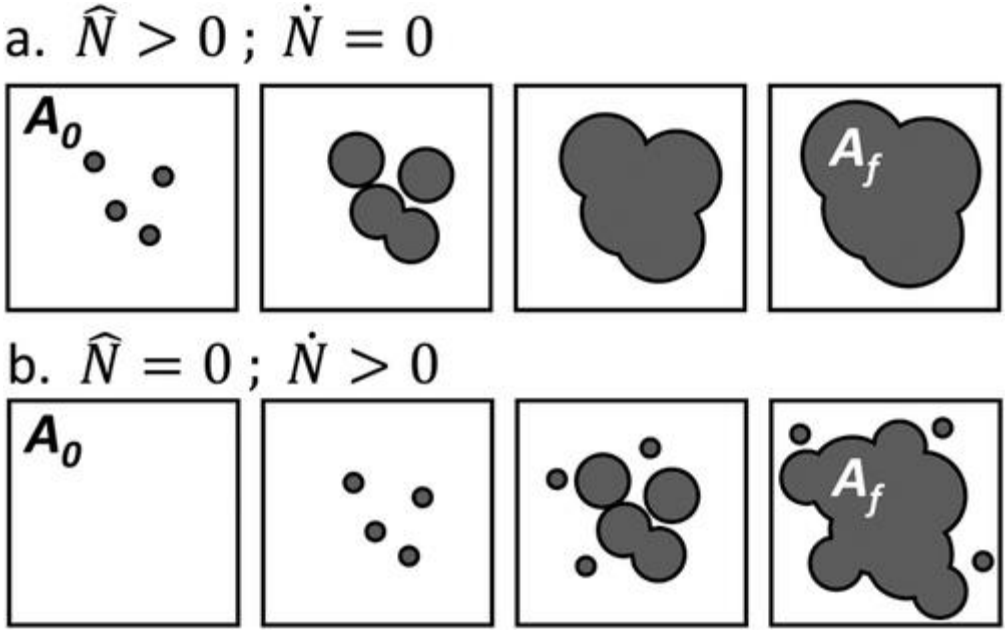

Figure 4.3. Nucleation as a function of time for two cases of (AS-)ALD. A shows the case where there are nucleation sites present on the starting surface, but no new sites are generated. B is the opposite case with no nucleation sites being present from the beginning, but new sites being generated. For an AS-ALD system to exhibit good selectivity over time, both the number of available sites from the start and the generation of new sites should be low. Adapted from ref.[144].

3.2.2 Epitaxial and oriented growth

Although ALD was first known as atomic layer epitaxy (ALE), this did not refer to actual epitaxial growth (crystalline thin films with a lattice match between the substrate and the deposited film that grows in a specific crystallographic direction), but rather to the fact that the atomic layers were arranged upon the surface. However, it has later been shown that ALD can be used to obtain epitaxial grown thin films. The ability to grow thin film crystals was an early motivation for development of the field as a whole[147]. An example of epitaxial growth by ALD is deposition of spinel type-structured (cubic) Co_3O_4 on $SrTiO_3$, MgO and α-Al_2O_3 where the growth direction of Co_3O_4 depends on the lattice match with the substrate[148]. Crystalline thin films grown by ALD may also be oriented even though they are not epitaxial. Oriented films means that the crystallites in the films do not grow in random

crystallographic directions, and that the preferred growth directions do not necessarily match with the lattice of the substrate. An example of an oriented system is found in **Paper II** of this work, where $CaMoO_4$ grows oriented on Si(100).

3.3 Development of multicomponent ALD-processes

This section presents multicomponent ALD-processes, meaning ALD-processes that contain several cations. In ref.[149] Mackus et al review several strategies to obtain doped, ternary or quaternary compounds by ALD. The most common strategy to do this, which is also done in this work, is to use *super-cycles*, or "cycles within cycles". A traditional binary ALD-process follow an A-B-A-B-.. . sequence, such as $TiCl_4$ + H_2O + $TiCl_4$ + H_2O for deposition of TiO_2[150]. In this current work, the deposition sequence used to deposit $CaMoO_4$ contained 17 cation pulses in each super-cycle, in order to attain the appropriate stoichiometry, as visualized in Figure 4.4.

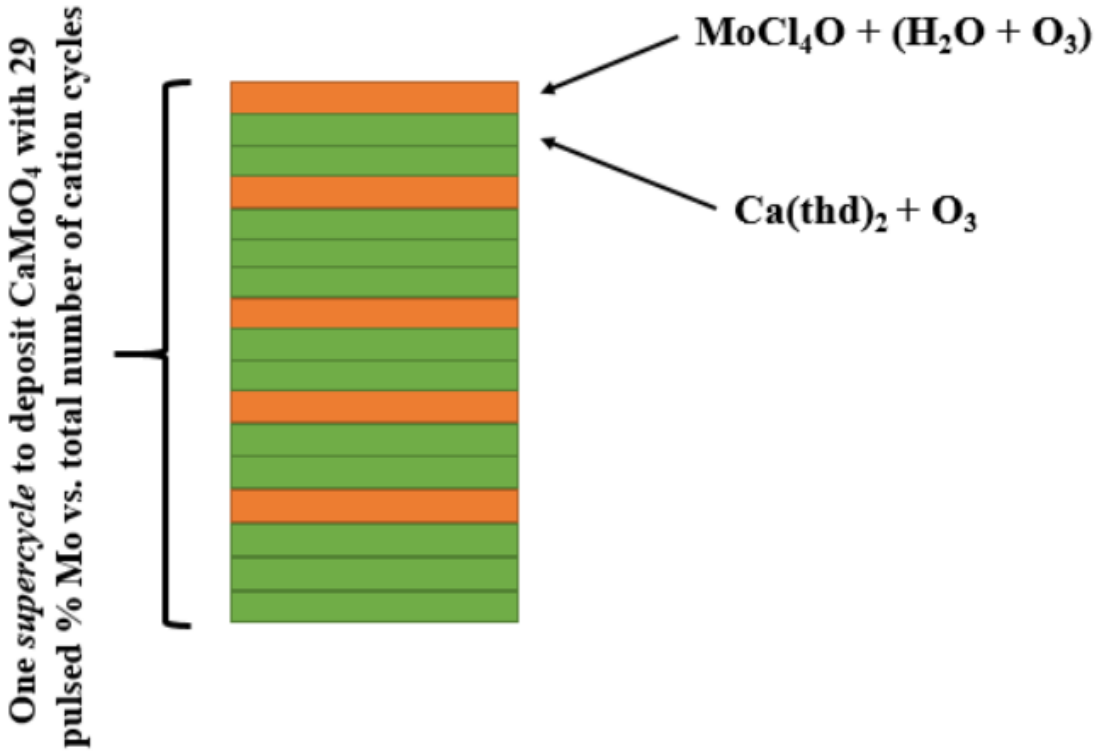

Figure 4.4. Illustration of one supercycle to deposit $CaMoO_4$ with 29 pulsed % Mo versus total number of cation cycles.

Even more complicated pulsing sequences are also found in this work in **Paper III**, when doping $CaMoO_4$ with Pr/Yb. The longest super-cycle contained 272 cation pulses. Choosing an appropriate deposition temperature may also be challenging when developing multicomponent ALD-processes, as it is not given that the multicomponent ALD-process have the same ALD-window as its binary constituents. This may go both ways, the ALD-window may be both larger or smaller. Sensitivity towards deposition temperature can be explained by the varying packing density of the adsorbing precursors on the surface with temperature. Different precursors will have different temperature ranges

were they are arranged in a beneficial manner for further growth. This is for example thoroughly investigated for the $La_{1-x}Ca_xMnO_3$ system[151].

3.3.1 Design of Experiments (DoE)

When developing new, complex ALD-processes, this work has utilized a Design of Experiments (DoE) framework. This type of statistical methodology has traditionally had limited use within the ALD-community, although a few reports prior to this work do exist[152, 153]. Typically, even complicated ALD-processes that require many factors (e.g. precursor and deposition temperatures, pulsing and purging times, pulsing ratios) to be tuned simultaneously, have been developed using one-factor at a time (OFAT) methods. When we, as a scientific community, use OFAT-methods, we tend to claim that we have more control as we only tune one factor at a time and keep the other factors constant. This mindset for efficient and thorough research has significant shortcomings[154]. Firstly, if several factors need tuning, many experiments are required, which may be a bottleneck if access to equipment is limited. Moreover, it neglects interaction effects. For example, when depositing $YbVO_4$, both the pulsed percentage of $Yb(thd)_3$ vs $VO(thd)_2$ and also the total number of cycles have effects on the growth rate, but which factor has the largest effect and if there is any interaction effect in between them, is not investigated in ref.[98]. Another thing we tend to forget when using the OFAT method, is the effect of errors that arise over time, such as slowly clogging tubes or developments in leak. If we at the same time gradually increase the deposition temperature of the process, it is easy to believe that the effect stems from the temperature. Although the skilled experimentalist should know that experiments must be randomized, this is in our experience often not done in practice.

The way to circumvent the limitations of the OFAT method when optimizing ALD processes, is clever usage of DoE. DoE is the application of statistics to set up your experiment to maximize the information that can be retrieved for a given number of experiments. In practice, it means altering several factors at a time for each experiment. The order of the experiments is predetermined and randomized. The concept was first proposed by Sir Ronald Fisher back in the 1930s[155]. Even though Sir Ronald Fisher was a bio-statistician who's original inspiration was the field of *eugenics* (that some human races are superior to others and therefore should be selected over others[156]), he is still viewed as the single most important statistician of the last century[157]. In 1946, Plackett and Burman worked further on the concept and published *The Design of Optimum Multifactorial Experiments*[158], an experimental design we now call the Plackett-Burman designs. This is still widely used, also when developing new synthesis routes[159-161]. Plackett-Burman designs, in addition to factorial designs, are excellent to screen for identifying which factors are active for processes with many factors. However, they omit interaction effects, meaning that they do not probe how, for example, increasing the annealing time and temperature simultaneously would affect a crystallization process.

Sir Ronald Fisher's son-in-law, George Box, was also a central figure in the further development of DoE. In 1951 he, together with Wilson, coined the term response surface methodology (RSM)[162].

When RSM is used, it is postulated that the response can be modelled with polynomials to fit a response surface. The two main types of RSM methods used today are central composite design (CCD) and Box-Behnken designs. In more present time, Draper has been the most dominant statistician publishing about RSM, and his work in ref. [163] written together with Box is a good source for more information on the topic.

DoE as a field has mostly been towards optimizing already established processes, often processes where only one product could be formed, such as studying how various fertilizers and watering affect the yield of a crop. The picture for using DoE in material science is more complex, as the margins between a successful and failed experiment is often small. More experimental outliers should be anticipated and accepted here, than for a simpler and more well-behaved system.

This thesis has used a face-centered CCD design in order to develop a process to deposit luminescent $CaMoO_4$. To describe the CCD design used here, some basic DoE terms must be introduced first. These include *input variables*, which are the variables being tuned and *response variables* which are the variables being measured. For an ALD-process, an input variable may for example be the deposition temperature and a response variable may be the growth rate per cycle. Moreover, the input variables are usually coded between -1 and 1, in order to ease the comparison in between them. For example, if the deposition temperature is between 340 °C and 400 °C, 340 °C is coded as -1, 370 °C is coded as 0 and 400 °C is coded as 1.

CCD experimental designs consist of three types of points/ runs, as visualized in Figure 4.5;

1. *Factorial points.* These are located at -1 and 1 for all the input variables being tuned and consist of all the combinations of these boundary values.
2. *Center points.* The center of the experiment is located at 0 for all the input variables. This run is typically repeated to also obtain a measure of the variance. It is a good practice to design the experiment so the center point is where the optimum is assumed to be. If this assumption holds, it will give good resolution of data around the optimum.
3. *Star/ axial points.* The star points are a distance α from the center along one of the axes. This means that for one of the input variables, the center value is retained for these points. For the face centered design utilized here, α is 1, means that for the star points in these types of experiment, one variable has the center value and the rest are at -1 or 1. If α is more than 1, the star points will correspond to runs where the maximum or minimum values for the input variables are used.

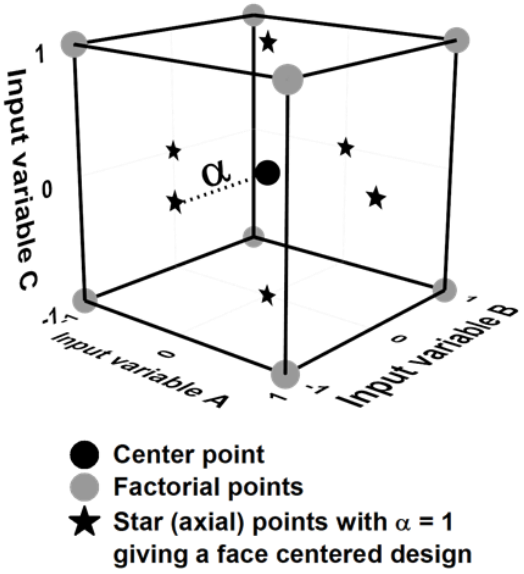

Figure 4.5. Visualization of the experimental points for a face centered central composite design setup. The directions, x1, x2 and x3 represent the various levels of the three input variables. Taken from Paper II.

In the CCD experiment done in this work, deposition temperature, pulsed percentage of the molybdenum precursor versus the calcium precursor, anneal time and anneal temperatures were used as the input variables, whereas the composition as measured by energy dispersive spectroscopy (EDS), the crystallinity measured by X-ray diffraction (XRD) and the photoluminescence (PL) signal were the response variables.

For further Pr^{3+}-doping of $CaMoO_4$ a simple three level, two factorial full-factorial design was used to investigate how the annealing time and temperature affected the Pr^{3+} luminescence. The levels for the annealing time were 30, 45 and 60 min. and the levels for the annealing temperature were 600, 700 and 800 °C. Since this was a full-factorial experiment, all the combinations of annealing time and temperature were tried, giving a total of nine different sets of annealing parameters.

4. $CaMoO_4$

Since this thesis revolves around $CaMoO_4$ as a host for down converters, this chapter is dedicated to describe $CaMoO_4$'s optical properties, how $CaMoO_4$ can be doped and how these doped and undoped structures have been synthesized previously.

4.1 $CaMoO_4$ and its optical properties

$CaMoO_4$ is known under the common name Powellite. It was first reported by W.H. Melville in 1891 where it was found as a by-product in copper and silver mines in Western Idaho[164]. It has a light yellow appearance, as can be seen in Figure 4.1, and is within the Scheelite family. Scheelites have the tetragonal space group $I4_1/a$ O2 (88), and are on the form ABO_4, where A is a divalent metal, often an alkaline earth metal, and B is Mo or W. Other Mo-Scheelites include $SrMoO_4$, $BaMoO_4$ and $PbMoO_4$. As the ionic radii of the A-atom increase from Ca – Sr – Ba – Pb, so does the parabola offset and thus also the possibility of non-radiative electron relaxation[165]. Therefore, this work has focused on $CaMoO_4$, and not on the other Scheelites. They are also easily doped, which will be the topic in subchapter 4.1.1. Visualizations of the unit cell of $CaMoO_4$ are shown in Figure 4.2. From these visualizations it becomes apparent that the molybdenum atoms are tetragonally co-ordinated and that there are six of these tetrahedra and six calcium atoms in each unit cell.

Figure 4.1. Powellite crystal found in Jalgaon, Maharashtra, India. Photo by Rob Lavinsky.

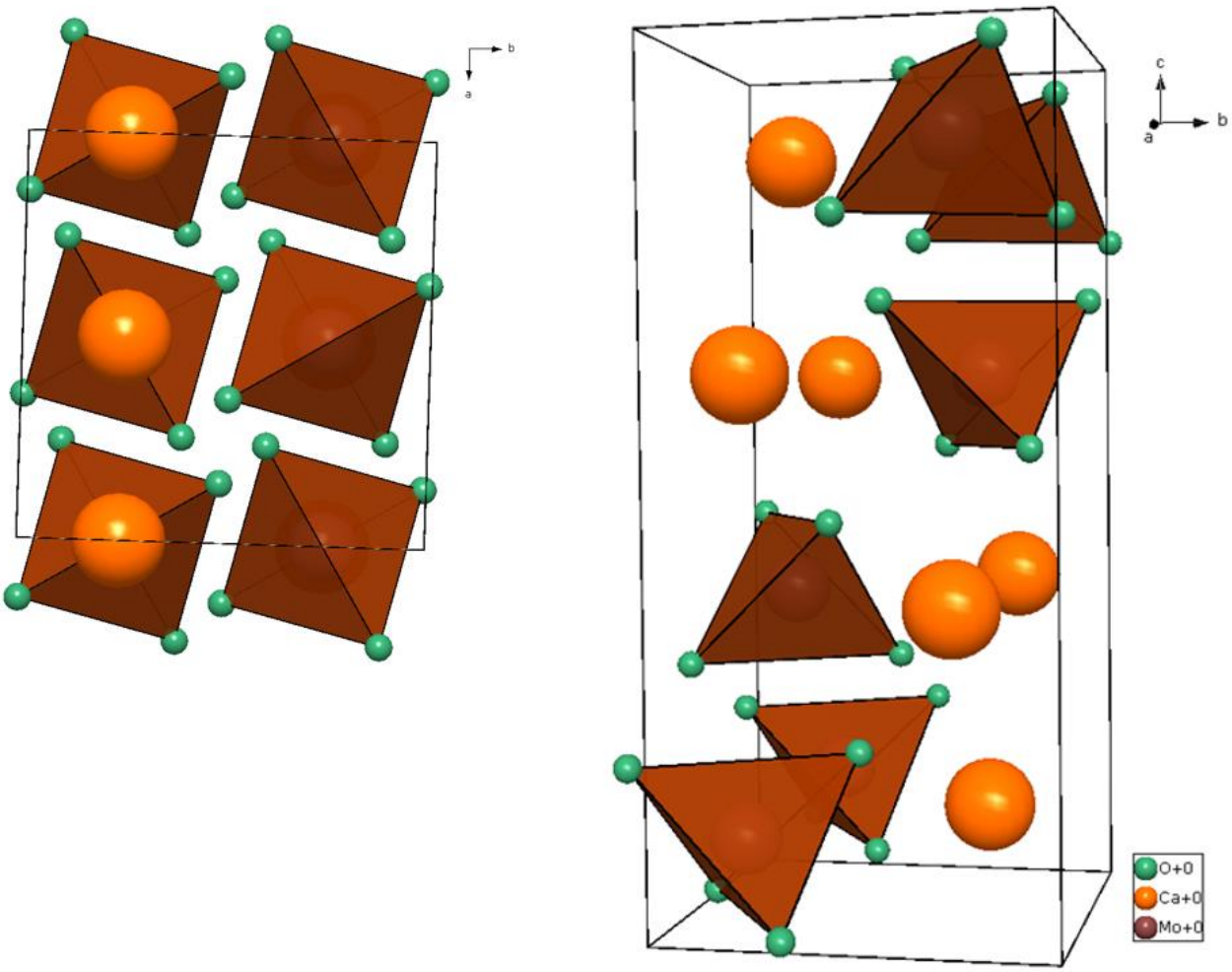

Figure 4.2. Visualizations of the unit cell of tetragonal $CaMoO_4$ where the Ca-atoms are orange, the O-atoms are green and the Mo-atoms are brown and within the tetrahedra.

The luminescence of $CaMoO_4$ was described by J.A. Groenink et al. in 1979, and consists of a green and orange contribution[166]. Whilst the origin of the green emission at 540 nm is clear and attributed to tilting of the $[MoO_4]^{-2}$-tetrahedra and identified as self-trapped exciton emission, the origin of the emission at 605 nm remains to be discussed[167]. It is, though, suggested to stem from tilting of $[MoO_4]^{-2}$-tetrahedra and thus from intrinsic oxygen vacancies. Long time annealing in an O_2-atmosphere has shown to eliminate the visible coloration due to removal of defects in the structure in the form of intrinsic oxygen vacancies and oxidation of Mo^{5+} to Mo^{6+}, assuming the presence of Mo^{5+} as defects in $CaMoO_4$ [28, 167]. In the more recent years, it has also been suggested that increased disorder in various Scheelites at room temperature leads to increased luminescence[27, 168]. This increased luminescence is thought to stem from a situation where units of $[MoO_4]^{-2}$-tetrahedra and $[MoO_3]^{-1}$ are both present in a partly disordered fashion, with the alkaline earth metal being intercalated. This is a pointer to why less crystalline $CaMoO_4$ samples may be more luminescent than more crystalline ones.

4.1.1 Doped $CaMoO_4$

A benefit with using $CaMoO_4$ as a host lattice for luminescent devices, is that it can be doped with lanthanides and at same time retain its crystal structure. The lanthanides are known to occupy the A-sites[169]. This means that a trivalent ion substitutes a divalent ion, requiring charge compensation. This can be achieved through co-doping with an alkaline metal, through vacancies in the A-site or reduction of Mo^{6+}. Ordering is found for both A-site vacancies, for the dopants or both simultaneously, usually as incommensurately modulated structures[170-173]. Lanthanide doping may also decrease site symmetry of the A-site. It is found from examining the Stark splitting for the $^5D_0 \rightarrow {}^7F_J$ transition for Eu^{3+} in $CaMoO_4$ by photoluminescence, that the site symmetry when for Eu^{3+} at the A-site is C_{2V}, and not S_4 as the usual A-site in pure $CaMoO_4$[174]. It is also recently suggested that the superspace approach is most suitable to model incommensurate Scheelites[175].

The intervalance charge transfer (IVCT) states of Scheelites are also high as compared to other possible hosts for luminescent devices such as titanates, niobates and vanadates[107-111, 113], leaving them less prone to for example quenching the $^3P_0$ level in Pr^{3+}, required for usage as spectral converters.

$CaMoO_4$ has previously been doped with all the lanthanides[22, 23, 25, 176-184] (except the radioactive Pm and Lu, which can also be considered as a d-metal even though IUPAC disagrees), either single-doped or co-doped, for a variety of possible applications, such as solar up- or down- converters[21, 183, 185], optical temperature sensors[186], lasers[187], light emitting diodes (LEDs)[30], microwave dielectrics[188] or photocatalysts[189].

4.2 Synthesis of $CaMoO_4$

$CaMoO_4$ has previously been synthesized in a number of ways, in addition to occurring naturally. Several studies report a simple solid state method[190, 191]. The combustion method[50, 192], the citric acid sol-gel method[26, 190], co-precipitation[193], a sonochemical route[194], Czochralski pulling[195] and flux growth[113] have also been used. The chosen approaches usually require a post-annealing step to obtain well-crystalline samples, such as the Czochralski pulled ones, which were annealed at 1000 °C. However, there are exceptions to this, like crystalline $CaMoO_4$ nanoparticles that have been synthesized by a molten salt method at 270 °C without post annealing[196], samples made by the sonochemical route at around 50 °C[194] or by microemulsions[197].

The literature is hugely diverging when it comes to both the optimal annealing parameters for how to obtain well crystalline $CaMoO_4$ samples and also how to obtain the most luminescent samples. For example, $CaMoO_4$ made by a microwave assisted citrate complex method shows more luminescence when annealed at 600 °C than when annealed at 400 °C for 3 h[29]. At the same time, the particle size and crystallinity both increase. On the other hand, a study of Eu^{3+} doped $CaMoO_4$ shows limited influence of the annealing temperature on the crystallinity[190]. The divergence in existing literature is

the main reason why the annealing parameters are explored thoroughly in **Paper II** for pure $CaMoO_4$ and in **Paper III** for $CaMoO_4$: Pr^{3+}, Yb^{3+}.

Even though $CaMoO_4$ has been synthesized in numerous ways previously, no present synthesis methods facilitate making conformal thin films required for usage in PV-systems nor are capable of controlling the placement of the dopants when $CaMoO_4$ is used as a host structure for spectral converters. The principle of tuning the relative position of the dopants in the host has been used for $CaMoO_4$ core-shell particles hitherto[176, 198-200], but not for $CaMoO_4$ thin films. ALD is able to circumvent these limitations, as it produces conformal thin films and can control where the dopants are in the growth direction of the film. This will in turn affect the amount of concentration quenching as we can actively distribute in space the dopant in the $CaMoO_4$ host, but also the FRET between Pr^{3+} and Yb^{3+}, which is indeed very distance dependent. The relationship between position and amount of Pr^{3+} and Yb^{3+} and PL properties is investigated in **Paper III**.

5. Characterization techniques

In this work a range of characterization techniques have been used, most of which are routine type techniques within the materials science community. Emphasis is therefore put on limitations, requirements and special considerations for the various techniques with respect to the thin films studied here, and the readers will be referred to other literature for more in-depth information on the techniques.

5.1 Photoluminescence

Since the photoluminescent properties have been the most important ones for both the doped and un-doped $CaMoO_4$ samples, photoluminescence (PL) measurements, also termed emission spectroscopy, have been key here. When PL measurements are performed, light with a fixed wavelength is shone upon a sample and the light emitted from the photoluminescent sample is then detected. PL gives information about the various radiative transitions of the sample. Inversely, we often use the technique to verify the presence of the lanthanide dopants, as the positions of these peaks are well known. A key parameter when performing PL measurements, is the excitation wavelength. This is often not tunable, but depends on the experimental setup. In the current work, both a 280 nm diode, a 325 nm HeCd-laser and a 405 nm diode have been used. The energy of the excitation source will in turn affect which radiative decay processes are triggered. The reader is referred to refs.[201, 202] for further information on PL.

5.2 Spectroscopic ellipsometry

In this work, spectroscopic ellipsometry (SE) was used as the routine tool to measure the thickness and refractive indices (reported at $\lambda = 632.8$ nm). In order to describe how SE works, we have to – again – shift how we look upon light. Light can also be described as an oscillating electric field with an amplitude, frequency and phase. If the light oscillates in more than one plane, which is usually the case, the light is unpolarized. Polarized light oscillates in one plane. When SE is performed, a polarized light beam is reflected of a thin film on a substrate. This polarized light beam has two components, the s-component (from German "senkrecht" meaning perpendicular) oscillating perpendicular to the plane of incidence, but parallel to the sample surface, and the p-component oscillating parallel to the plane of incidence. When this light is reflected from the surface and interface(s) of the sample, the amplitudes of the s- and p-components will change. Instead of being linear, the light will now oscillate in an elliptical fashion – thus the name of the technique. The amplitude ratio on reflection, Ψ, and the phase shift, Δ, are measured by the ellipsometer, and related to the amplitudes after reflection, R_s and R_p, in the following manner;

$$\frac{R_s}{R_p} = tan\,\Psi e^{i\Delta} \qquad 5.1$$

Ψ and Δ are related to the optical constants of the sample, such as the refractive index, and to the film thickness. However, in order to obtain useful data for the thin film scientist from ellipsometry, the data has to be modelled. The theoretical basis for modelling and thus retrieving information from Ψ and Δ is

found in the Fresnel equations, elaborated in ref.[203]. Especially Δ is sensitive towards the film thickness. The simplest conventional method to model ellipsometry data is to use Cauchy functions, but that assumes transparent films. Since this work aimed at making absorbing films, this was not a suitable model. Therefore, a Tauc-Lorentz model including the band gap of the material has been used. Moreover, several of the films deposited in this study have been very rough. This is taken into account by the modelling when a roughness parameter is included. The film is then assumed to consist of two layers, a dense in the bottom and one with half the optical density on top.

In the current work, a J.A. Woollam alpha-SE ellipsometer with an incident angle of 70° was used. The associated CompleteEASE software was used for data modelling and analysis.

5.3 X-ray diffraction

X-ray diffraction (XRD) has been used to investigate if crystalline phases were present in the samples, and also to identify these. XRD investigates how incoming X-rays are scattered by a sample. If the atoms are arranged in a period manner, the scattered X-rays will have constructive interference for certain incoming wavelengths, as described in Bragg's law below[204];

$$n\lambda = 2d\sin\theta \qquad 5.2$$

where n is a positive integer, λ is the wavelength of the incoming X-rays, d is the separation distance between the crystal planes and θ is the angle between the incoming X-rays and the sample. There are many different XRD configurations, but typically the incoming angle, θ, is varied, and the resulting observed X-ray intensities are plotted versus 2θ. This type of configuration is often referred to as θ-2θ or powder XRD[205].

The specific crystal structure and its symmetry gives rise to a distinct set of crystal planes that diffract the incoming x-ray beam and thus also its own diffraction patterns. These standard patterns are found in various databases, and can be used to identify the present crystalline phases. In this work the Crystallography Open Database (COD) is used[206]. A Bruker AKS D8 Discover diffractometer using Cu Kα radiation and equipped with a Ge(111) monochromator and a LynxEye detector has been used in this work. For more information on XRD, the reader is referred to ref.[207].

5.3.1 Pawley refinements and oriented growth

When developing a synthesis route for $CaMoO_4$, quantification of many XRD diffractograms was required to use this data in further statistical analysis. This raised several challenges. Firstly, there were peaks of undesired phases (calcite and aragonite) in near proximity of some $CaMoO_4$ peaks. This means that simply adding the area under the curves for certain peaks or reading out their maximum levels, may point to the complete opposite conclusion about which crystal phases are present than what is actually the case. Refining the diffractograms for accurate quantifications was therefore necessary. The most common method to refine data from conventional powder XRD measurements, is performing Rietveld refinements[208], using a least squares approach. This method does, however, assume that the measured

pattern indeed stems from a material where the crystallites have random orientations, e.g. is a powder. This assumption does not hold for the $CaMoO_4$ thin films deposited in study. As we can see from Figure 5.1, the peak ratios between the various samples differ – and we can thus assume that the crystallites do have some orientation and that this orientation differs between the samples.

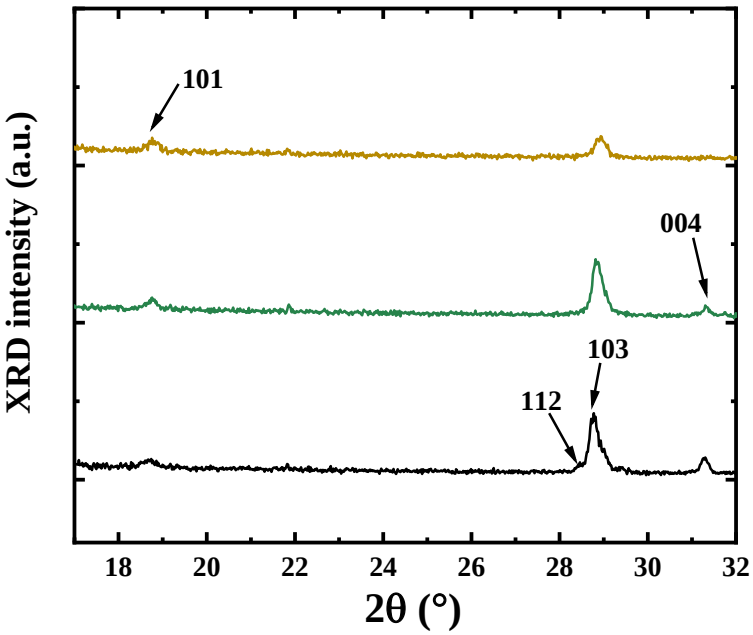

Figure 5.1. XRD diffractograms of three $CaMoO_4$ samples deposited in the same ALD-run at 350 °C using 29 pulsed % Mo, and annealed at 612.5 °C for 15 minutes. The peak ratios between especially the (101) and (103) reflexes differ between the samples, indicating that the orientations of the crystallites differ as well. This difference in diffractograms despite being deposited under the same conditions, underlines the need to perform Pawley refinements to evaluate the crystallinity.

To accommodate the different orientations between the samples, the diffractograms were refined using Pawley refinements[209]. This method has the peak intensities as a free, fitted parameter, and thus take the various orientations into account. To quantify the data for the further central-composite design, the intensities obtained from the refined structure factors for the (101), (112), (103) and (004) peaks were added. These intensities, in addition to the crystallite sizes, were obtained using the Topas 5 software. Please note there was no established method to quantify powder XRD data for further statistical DoE analysis at the start of this work.

5.4 Scanning electron microscopy

When performing scanning electron microscopy (SEM) an electron beam is scanned across the surface of the sample. The electrons can interact with the surface in various ways. In the topmost part of the sample, there may be inelastic interactions between the atoms of the sample and the electron beam. The electrons stemming from this type of interactions are termed secondary electrons (SE). Since this interaction does not penetrate deep into the sample, SE images carry information about the topography of the samples. Another type of electrons that can be detected by the SEM, is back-scattered electrons (BSE). These originate from elastic events between the incoming electron beam and the sample. The

probability of these events is highly related to the atomic number of the sample. Since heavier elements scatter more than lighter elements, they will appear brighter in the micrographs. In the current work a HITACHI TM3000 SEM with a working distance of approximately 9 mm and an acceleration voltage of 15 kV has been used. This SEM is only configured for detecting BSE, and for performing energy-dispersive spectrometry (EDS). SEM has in the current work been used as a routine tool to check the homogeneity of the samples and to obtain a measure of the composition by EDS (see subchapter 5.4.1).

5.4.1 Energy-dispersive spectroscopy

EDS is an "ad-on" to the SEM, and is used to get information of the chemical composition and may also be used to create elemental maps. It is also often referred to as energy-dispersive X-ray spectroscopy (EDX), and is sometimes also abbreviates as EDXS or XEDS. When EDS is performed, the X-rays emitted from the sample after interacting with the electron beam are analyzed. As the x-rays are element specific, EDS can give an overview of which elements are present and also where they are located. This has given valuable information of the homogeneity of the $CaMoO_4$ thin films in this work. It was also useful to visualize the patterning of the area-selective deposition process found for the $MoCl_4O$ + (H_2O + O_3) process. In Figure 5.2 a square "hole" is made in a LiF film on top of a Si(100) substrate. The $MoCl_4O$ + (H_2O + O_3) process grows selectively on LiF and not on Si(100), and this patterning was made to illustrate this on a single substrate. EDS point scans were used to calculate the selectivity of the $MoCl_4O$ + (H_2O + O_3) process (see chapter 6.2). A drawback about EDS is that it is not very accurate, and is unable to find trace elements or dopants of low concentration, such as Pr or Yb in the $CaMoO_4$:Pr, Yb films made in this work. A Quantax70 Energy Dispersive X-ray Spectrometer connected with the HITACHI TM3000 SEM was used for EDS in the current work. Acquisition times ranged from 1 to 5 minutes. The reader is referred to ref.[210] for more information on both SEM and EDS.

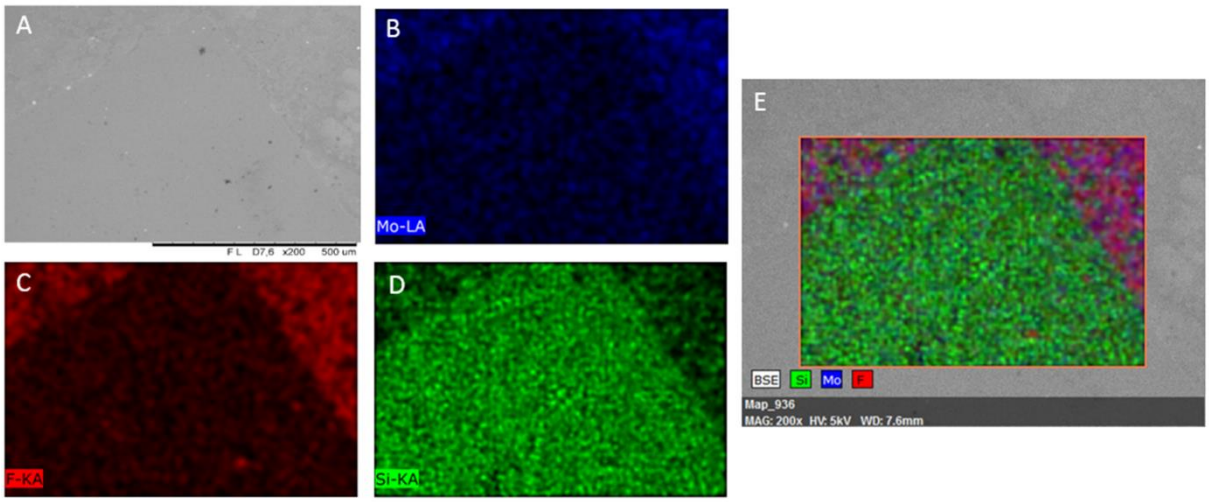

Figure 5.2. BSE micrograph (A) and EDS elemental maps (B, molybdenum, C, fluorine, D, silicon, E, combined EDS map) of a MoOx thin film deposited on a patterned LiF film on a Si(100) substrate. The LiF film in the square pattern is removed by lithography.

5.5 Optical spectroscopy

Optical spectroscopy, also known as absorption spectroscopy or UV-Vis-NIR spectroscopy referring to the used wavelengths, can be used to measure the transmission or reflectivity of a material, and thus also calculate the absorption. In this work, optical spectroscopy has been used to measure the transmission of $CaMoO_4$ deposited on silica. The instrument used here was a Shimadzu UV-3600 spectrometer, with a photomultiplier tube able to detect from 180-900 nm. More information about optical spectroscopy of inorganic materials is found in ref. [211]. In order to estimate the band gap of the materials, UV-VIS transmission spectra have also been used to construct Tauc-plots[212].

5.6 Atomic force microscopy

Since its invention in 1986 by Binnig, Gerber and Quate[213], atomic force microscopy (AFM) has emerged as a prominent tool to investigate the topography on the nanoscale. When AFM is performed, a sharp tip rasters across the investigated surface. The tip is mounted onto a flexible cantilever. When the tip experiences forces from the surface as they approach very close, the cantilever will deflect. This deflection is measured by a laser pointing on top of the cantilever and reflected onto a photodiode detector. A great advantage of AFM versus other methods to investigate surface topography, such as SEM, is that it can be used in air and also for non-conducting samples. Some configurations can even measure samples in liquids. The instrument used in this investigation is a Park Instruments XE-70 in contact mode with a CONTSCR tip. The micrographs were analyzed with the Gwyddion freeware to retrieve RMS rouhgnesses. For further information about AFM, the reader is referred to ref. [214].

5.7 X-ray fluorescence

When performing X-ray fluorescence (XRF), a core electron is excited by an incident X-ray beam. When the excited electron is relaxed, X-rays are emitted, a process called fluorescence. The X-rays energies are element specific, and XRF is thus used for compositional analysis. XRF is very sensitive and can detect content down to 1-10 ppm for well optimized instruments. XRF is not as sensitive for thin film samples, but sensitivities down to 1 % are expected. In this work a Panalytical Axios Max Minerals XRF with Omnian and Stratos softwares was used to obtain information on the Ca:Mo ratio and also possible Cl contamination from the $MoCl_4O$ precursor. Unfortunately, the instrument is not configured with standard samples for accurate measurements of most of lanthanide ions, including Pr and Yb of interest in the current work. The instrument requires sample sizes of around 3x3 cm^2, limiting the possible number of examined samples from a single ALD run. A thorough introduction to XRF is given in ref. [215].

5.8 X-ray photoelectron spectroscopy

When X-ray photoelectron spectroscopy (XPS) is performed, an incident X-ray beam is also used to excite core electrons so much that they are ejected from the atom. These ejected atoms are measured in terms of number and energy. XPS data is presented as the binding energy versus intensity. This binding energy is found by;

$$E_{binding} = E_{photon} - (E_{kinetic} + \Phi) \quad 5.3$$

where Φ is the work function, $E_{binding}$ is the binding energy, E_{photon} is the energy of the incoming X-ray beam and $E_{kinetic}$ is the measured energy of the ejected electrons. As the interaction volume is shallow, this is a surface sensitive technique, limited to approximately the topmost 10 nm of the sample. Depth profiling is possible using Argon sputtering. In addition to giving compositional information, XPS also reveals information about the oxidation and binding state. In the current work a Thermo Scientific Theta Probe instrument equipped with an Al Kα source was used. The C1s peak from adventitious carbon at 284.8 eV was used for calibration. The review in ref. [216] gives more information about XPS.

5.9 Four-point-probe measurements

Four-point-probe measurements is a method to characterize the resistivity of the film. It utilizes, as the name suggests, four small probes on top of the thin film. The four probes are in line, and as a current is sent through the outermost probes, the voltage is measured between the two probes in the middle. Assuming that the film is very thin and using Ohm's law, the specific resistivity of the film can be calculated. More information about four-point-probe measurements can be found in ref. [217].

5.10 Precursor tester

To evaluate new ALD-precursors, our home-built precursor tester has been used (Figure 5.3). In the precursor tester the precursors can be evaluated with similar conditions as in the ALD-reactor. The precursor is loaded on a heating unit and analyzed under vacuum. The precursor is heated in a controlled manner while logging the temperature. Meanwhile, the precursor is monitored with time-lapse photography and a quartz crystal microbalance (QCM) unit nearby, to look for signs of sublimation. Data obtained from the precursor tester is used to determine the sublimation temperature of the precursor when used as an actual ALD-precursor on a later stage. Moreover, may the time- photographs show signs of undesired processes, such as decomposition or polymerization of the precursor. QCM was first described by Sauerbrey[218], and exploits how the resonance frequency of the piezoelectric quartz crystal changes with small variations in the mass. Any increase in mass will here come from the sublimating precursor.

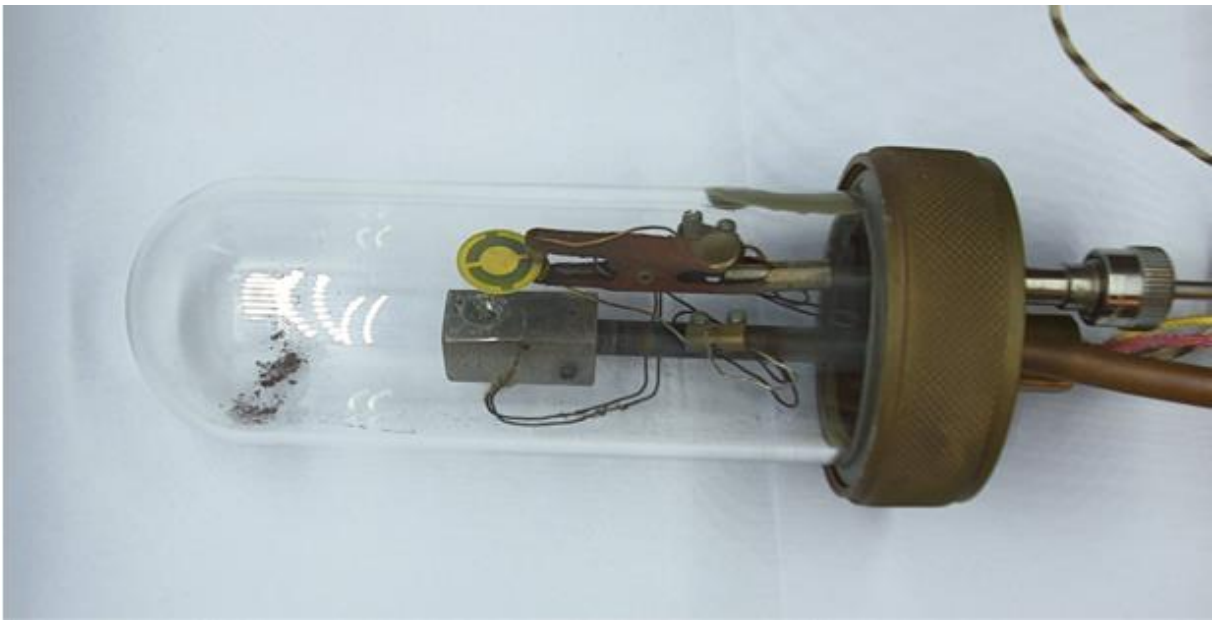

Figure 5.3. The home-built precursor tester used in the current study, equipped with a heating unit and a QCM crystal. The camera was not mounted when this photo was taken.

6. Results and discussion

This section presents and discusses the most important results of this thesis. The three papers are all interconnected and work towards the common goal of making down-converting $CaMoO_4$: Pr^{3+}, Yb^{3+} thin films by ALD. As means for describing the work and its findings, the text will focus on the path towards the goal and emphasize the scientific decision making and research design behind the results. I believe this will provide a more honest and rewarding reading for the PhD students to follow.

6.1 $MoCl_4O$ as an ALD-precursor

The first step towards depositing $CaMoO_4$: Pr^{3+}, Yb^{3+} was to establish an overview of readily available precursors, their sublimation temperatures and their reported ALD-windows (Table 6.1) Already at the initial stages of this work, our group had extensive experience in deposition of both MoO_3[219], CaO/ $CaCO_3$[220] and various lanthanide oxides[221]. Moreover, we were experienced in combining these processes, and others, to deposit complex oxides [97, 151, 222-224]. We therefore thought that settling on which precursors to be used should be trivial. Studying the processes listed in Table 6.1, led us to believe that deposition of $CaMoO_4$:Pr^{3+}, Yb^{3+} would be possible at around 300 °C or slightly less, using $Ca(thd)_2$, $Mo(N^tBu)_2(NMe_2)_2$, $Pr(thd)_3$ and $Yb(thd)_3$.

Initially, unsuccessful attempts on using $Mo(N^tBu)_2(NMe_2)_2$ to deposit MoO_3 were made. This precursor had also previously been tried by other colleagues without obtaining film growth, but we were armed with new hope. At the given time, we had no convenient setup for using precursors such as $Mo(N^tBu)_2(NMe_2)_2$ that both required inert handling and heating. The precursor was placed externally, with heating coils surrounding the gas line towards the reactor. Uneven heating may be the reason why this did not work. Nevertheless, we decided that developing a process for MoO_3 that could withstand deposition temperatures around 300 °C without decomposition, was required for the further progress for this project.

Table 6.1. ALD-processes for Ca, Mo, Pr and Yb oxides already established when the current work started. Thd = 2,2,6,6,-tetramethyl-3,5-heptanedione, iPr = isopropyl, Cp = cyclopentadienyl, Et = ethyl, Ben = benzene, Me = methyl, Bu = buthyl. AMD = tetrakis (N,N'-dimethylacetamidinate).

Precursor	**Co-reactant**	**Sublimation temperature (°C)**	**ALD-window of binary oxide (°C)**	**Reference**
$Ca(thd)_2$	O_3	195	200-450	[220]
$Ca(^iPr_3Cp)_2$	H_2O	100	205-300	[225]

$Mo(CO)_6$	H_2O + O_3	25	152-172	[219]
$Mo(EtBen)_2$	H_2O/ O_3	120	150	[226]
$Mo(NMe_2)_4$	O_3	Not given	60-120	[227]
$Mo(N^tBu)_2(NMe_2)_2$	O_3	50	200-275	[228]
$Mo(SiMe_3Cp)(CO)_2(\eta^3$-2-MeAllyl), (initial grafting required)		90	250-300	[229]
$MoO_2(thd)_2$	O_3	135	240-260	[230]
$MoO_2(^iPrAMD)_2$	O_3	120	175	[231]
$Pr(^iPrAMD)_3$	H_2O	125	200-315	[232]
$Pr(EtCp)_3$	H_2O	130	130-250	[233]
$Pr(^iPrCp)_2(^iPr_2AMD)$	H_2O	125	200-300	[234]
$Pr[N(SiMe_3)_2]_3$	H_2O	140	200-400	[235]
$Pr(thd)_3$	O_3	155	300	[221]
$Yb(thd)_3$	H_2O	125	300-350	[236]
$Yb(MeCp)_3$	O_3	Not given	Not given	[237]

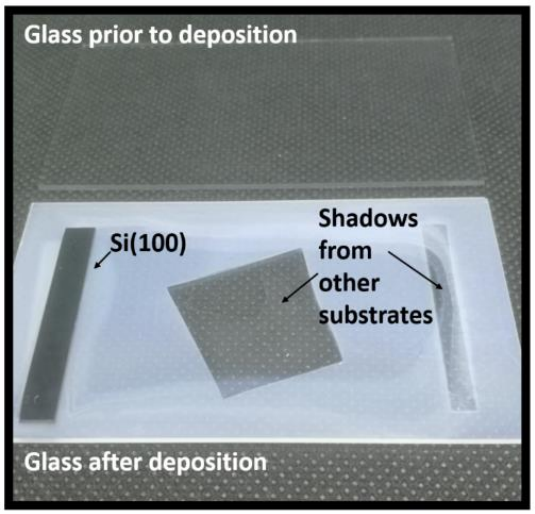

Figure 6.1. First test of $MoCl_4O$ + (H_2O + O_3), showing obvious signs of film growth at the glass plate. Taken from Paper I.

The first step for developing a new MoO_3 process, was to study available precursors that could be easily bought and testing these. In addition to $MoCl_4O$, $(C_7H_8)Mo(CO)_3$ (Cycloheptatrienemolybdenum tricarbonyl) was also purchased, both from Sigma-Aldrich. Both precursors were tested with the precursor tester described in chapter 5.10. $(C_7H_8)Mo(CO)_3$ showed signs of re-sublimation already at 100 °C with a mass reduction at the QCM crystal, and as therefore not investigated further. The results for $MoCl_4O$, however, looked promising. Signs of sublimation were seen at 60 °C and the precursor seemed to withstand temperatures up to the tested maximum of 300 °C without decomposing, which is the major issue for many of the established processes for MoO_3. $MoCl_4O$ was therefore tested together with H_2O and O_3 at 300 °C. Co-pulsing of H_2O and O_3 was chosen as this yields the highest growth rates also when using $Mo(CO)_6$ as the molybdenum source[219]. Since $MoCl_4O$ sublimed at so low temperatures *in vacuo*, it was kept at room temperature externally at the reactor, and introduced into the reactor using extra N_2 carrier gas. The fact that the precursor can be kept externally ease the inert handling significantly. The

initial results where both encouraging and confusing simultaneously – we could obviously see film on the glass plate (Figure 6.1.1), but not measure any film at the silicon substrates. This indicated substrate selective growth, which is the topic of chapter 6.2.

In addition to experimentation in the lab with $MoCl_4O$ as an ALD-precursor, thermodynamical modelling was performed. Eq. (1) shows the proposed reaction between $MoCl_4O$ and H_2O. The physical experiments also used ozone during deposition. Ozone is a difficult compound to treat thermodynamically since it is metastable and thus perturbs the calculations. Our approach is to consider ozone as a species that mainly activates the substrate, and not as a specie taking part in the reaction with $MoCl_4O$. O_3 is therefore not considered in the reaction below.

$$MoCl_4O(g) + 2H_2O(g) \rightarrow MoO_3(s) + 4HCl(g) \quad (1)$$

The calculated equilibrium constant, *K*, of this reaction is $2.3 \cdot 10^8$, $8.4 \cdot 10^7$ and $3.7 \cdot 10^7$ at 200 °C, 250 °C and 300 °C, respectively. This means that the reaction indeed is highly favorable, but becomes slightly less favorable with increased temperatures.

Application of oxychlorides as ALD-precursors have been very limited so far. WCl_4O was slightly investigated in our group previously, but only limited growth was seen[238]. This may be due to the same substrate selectivity as seen for $MoCl_4O$, and its growth should hence be revisited. *In-situ* generated $NbOCl_3$[239] and $TaOCl_3$[240] have been suggested as precursors for deposition of their binary oxides in combination with H_2O. These oxychlorides have however, not been used directly. We hope that our example of using $MoCl_4O$ will open up for more investigations into oxychlorides as ALD-precursors.

6.2 Area-selective growth of MoO_x

When we first realized that $MoCl_4O$ + (H_2O + O_3) had growth rates that depended on the type of substrate, our next move was to map the growth on various substrates. We started to reflect on the difference between glass and Si(100) with a native oxide layer, which were the two inaugural surfaces tried. In addition to silica, conventional soda-lime glass consists of around 15 % sodium oxide. A natural extension was then to investigate our other available sodium containing substrate, a Na_2CO_3 thin film on Si(100). In addition, we added substrates consisting of films with lithium, also an alkali metal. We also added substrates containing Ca, in the form of $CaCO_3$ on Si(100), since we already had plans of using $MoCl_4O$ in a system with Ca to deposit $CaMoO_4$. The results of these investigations are listed in Table 6.2.1, and show that the $MoCl_4O$ + (H_2O + O_3) system grows on glass and LiF and not at all on the other substrates at 300 °C.

Table 6.2. Thicknesses of films before and after deposition of MoO_x as measured with spectroscopic ellipsometry at 300 °C, using 1000 cycles. Besides the glass, Si(100) and silica substrates, the substrates were ALD-films deposited in-house. Taken from Paper I.

Substrate	**Film thickness before deposition (nm)**	**Film thickness after deposition (nm)**
Glass	-	72.3
LiF[241]	45.5	114.2
Si(100)	2.3	3.0
$CaCO_3$[220]	52.2	54.0
Na_2CO_3[242]	73.4	72.1
Li_3PO_3[243]	88.6	90.1
Silica	-	Not able to measure any film

We were surprised to see that our process grew on LiF in addition to glass, particularly since the films did not grow on Li_3PO_3 and we had no reason to believe that Li^+ is more mobile in LiF than in Li_3PO_3. One difference between LiF and $CaCO_3$, Na_2CO_3 and Li_3PO_3, is that it is probably not terminated by a carbonate. We hoped growth of MoO_x on LiF could enable studying the process with a quartz crystal microbalance (QCM) – the tool we normally use to *in-situ* examine pulsing and purging parameters and verify that we indeed have ALD-growth. Using QCM requires the process to grow on gold crystals placed in the ALD-chamber. Numerous attempts were made using LiF as seeding layers on the QCM crystals for further growth and characterization of the $MoCl_4O$ + (H_2O + O_3) process without success. A reason may be that QCM with ozone-depending processes are inherently difficult as the heat released during the ozone pulses leads to thermal fluctuations that may dominate the desired signal. For these attempted investigations, the LiF pulses could be identified in the QCM data, but the MoO_x-sections were dominated by noise. The deposition temperature was lowered to 225 °C from the first attempted 300 °C, but this did not aid the results either.

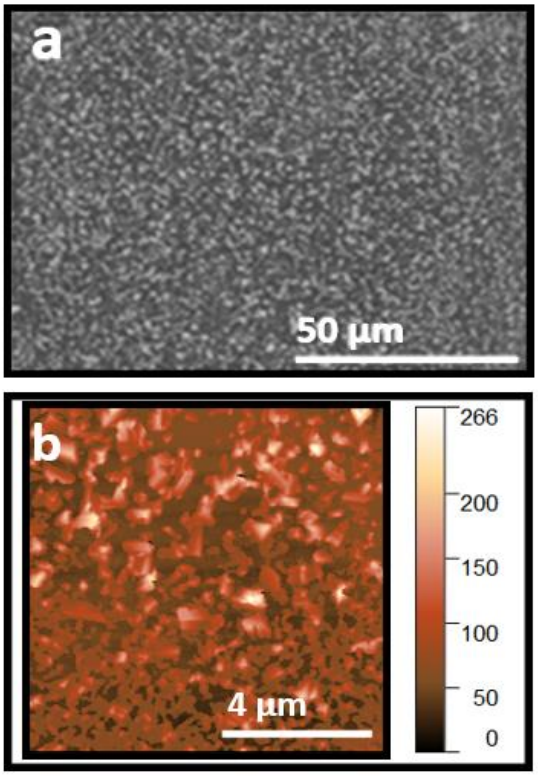

Figure 6.2. SEM micrograph (part a, top) of MoO_x deposited on glass at 250 °C and AFM micrograph (part b, bottom) of MoO_x deposited on glass at 300 °C, both using 1000 cycles. Taken from Paper I.

Since QCM could not be used, pulsing and purging parameters were found using simple trial and error, and the shortest parameters yielding even films along the precursor flow direction, were chosen.

Measuring the film thicknesses of these films with spectroscopic ellipsometry was difficult and spot dependent and Figure 6.2 gives a hint to why. As can be seen from Figure 6.2, part B, the film contains pin-holes and is less dense in the top of this micrograph than in the bottom. Micrographs were taken on samples deposited between 200 and 350 °C, and all looked similar.

The process was investigated between 200 and 350 °C and the growth rates are shown in Figure 6.3. At 300 and 350 °C, using 5000 ALD cycles in addition to 1000 ALD cycles was also attempted, and these results surprisingly show that the growth per cycle (GPC) is not constant, which it should be for a well-behaved ALD-process. These investigations also show that the growth below 275 °C is limited – probably due to poor kinetics, and perhaps challenges in nucleation.

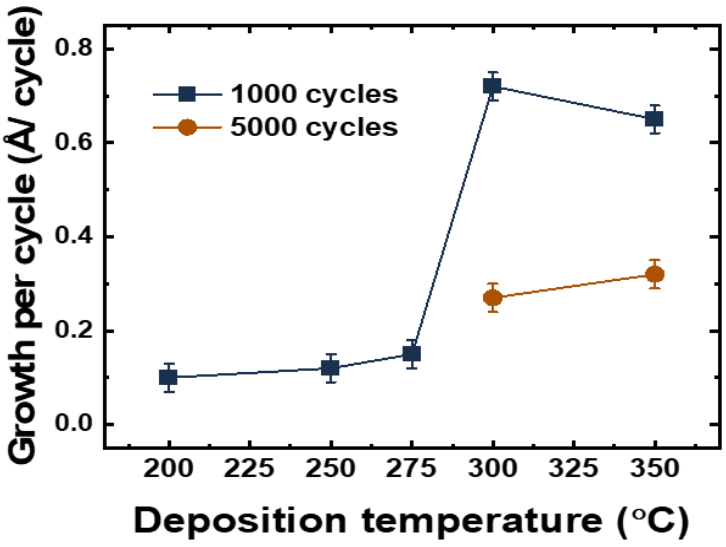

Figure 6.3. Growth per cycle on glass versus deposition temperature of MoOx for the $MoCl_4O$ + (O_3 + H_2O) system using 1000 (blue) or 5000 (purple) ALD cycles. Taken from Paper I.

Since the GPC is not constant and decrease for thicker films, we started to believe that the growth may be aided by diffusion from the substrate. This will in turn explain the substrate selectivity – some substrates contain something that aid growth and other substrates do not. To investigate the contents of the films deposited on glass, XPS was employed. The results of these investigations are shown in Figure 6.4, and reveal that the MoO_3 thin films contain a significant amount of sodium when deposited on glass. The detailed scans around the $3d_{3/2}$ and $3d_{5/2}$ peaks for Mo, show that the valence of Mo is likely 6+, consistent with MoO_3. Survey scans of films deposited on LiF similarly reveal lithium in the films. We know from Fick's second law that diffusion lengths scales with the square root of the time. Therefore, the purging times were increased to allow the system to diffuse from before the next pulse. Increase the purging times indeed led to an increase in the GPC, supporting growth limited by diffusion of either sodium or lithium from the substrate.

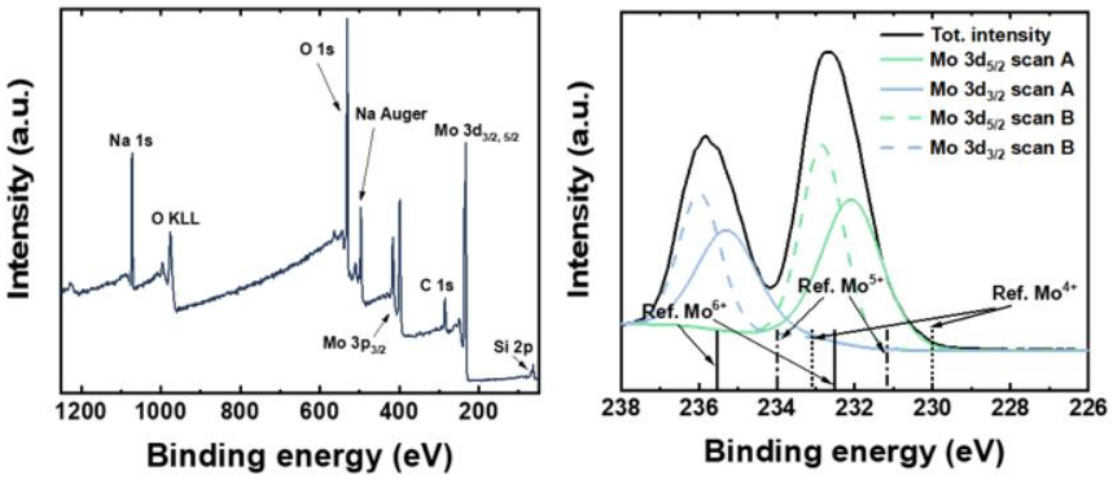

Figure 6.4. XPS of a thin film deposited on glass at 300 °C using 1000 ALD cycles of the $MoCl_4O$ + (H_2O + O_3) process. The figure to the left shows a survey scan, whereas the figure to the right shows scans around the $3d_{3/2}$ and $3d_{5/2}$ peaks of Mo used to identify the valence of Mo. Reference scans are from ref. [244]. Taken from Paper I.

Subsequently, conventional XRD was performed on the thin films, in order to reveal the presence of possible crystalline phases (Figure 6.5). Again, this system surprised us, as the XRD investigations revealed presence of the Magnéli phase Mo_9O_{26} when deposited at 250 °C[245] and MoO_2 when deposited at 300 °C, and none of the known crystalline MoO_3 phases. We have not found other reports of Mo_9O_{26} as thin films, and there seem to be limited consensus in the literature on how these phases can be synthesized reproducibly. Since the XPS data indicate that Mo is mostly 6+ when deposited at 300 °C, we assume the film is in the form of an amorphous MoO_3 matrix containing some MoO_2 crystallites that dominate the diffractogram.

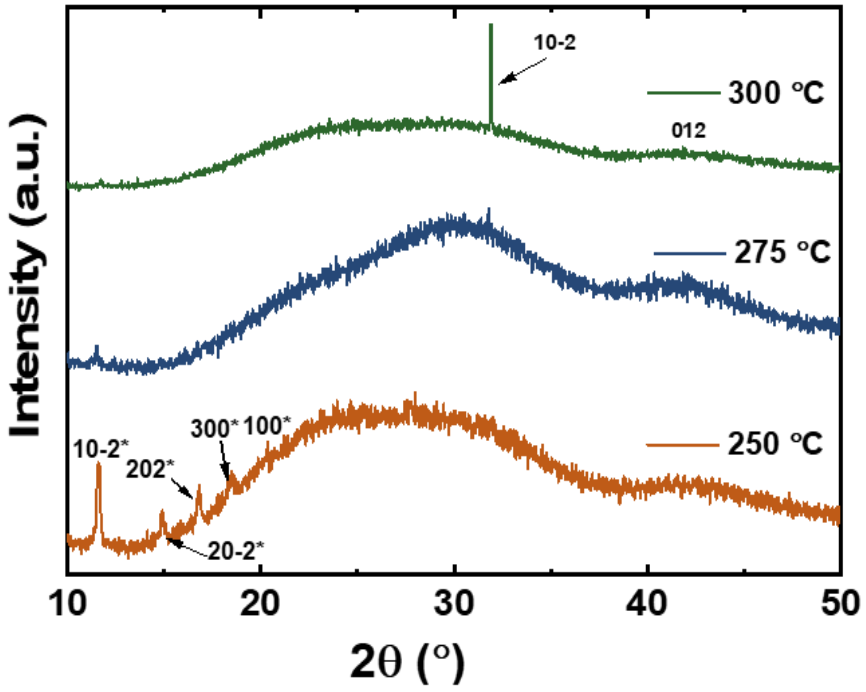

Figure 6.5. XRD diffractograms of molybdenum oxide thin films deposited at varying temperatures using 1000 cycles. Selected reflexes from Mo_9O_{26} (P 2/C, with asterisk)[246] and MoO_2 (C 2/m, tugarinovite, no asterisk)[247] are indexed for comparison. Taken from Paper I.

When investigating area-selective ALD processes, the selectivity should also be quantified[144]. We chose to characterize the selectivity between glass and Si(100) with a native oxide layer, based on EDS measurements. Mo is heavy and small amounts should be detectable by EDS. As described in subchapter 3.2.1 – area-selective atomic layer deposition, the selectivity, S, is defined as the amount (or rate) of one product relative to the total amount (or rate) of all products formed. When depositing thin films on a substrate, the amount of a product formed is in proportion to the measured fraction covered by nuclei, which in turn is in proportion to the deposited film volume. Therefore, the measured amount of Mo vs (Mo+ Si) can be used as a measure of the amount of deposited film. In our case, the investigations of selectivity are for 1000 cycles. The selectivity for area-selective processes is dependent on time, aka the number of cycles. For longer times, the chance of growth on the non-desired growth area increases. After the initial nucleation, the undesired growth will speed up and the growth rate is soon similar to the growth rate for the desired growth area. The selectivity is usually lost after much fewer cycles than used in the current study[144], such as after 50 or 200 cycles at most, which is also the reason why area-selective processes are often combined with atomic layer etching[142, 143]. The results of our selectivity investigation are shown in Figure 6.6, and reveal that no film could be measured at the Si(100) surface when the film was deposited at 300 °C or below.

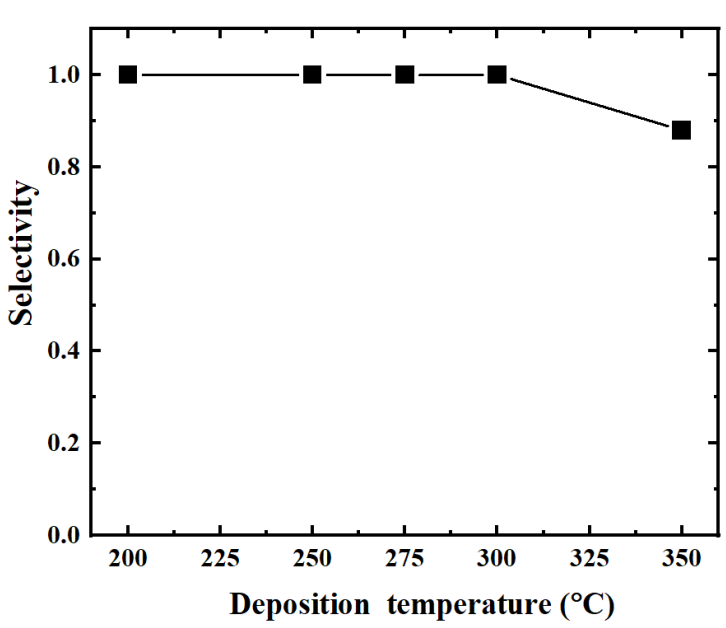

For an AS-ALD process to be truly useful, the selectivity still has to hold on a patterned substrate. Lithography was therefore employed to pattern a LiF film. In order to satisfy our childishness, we chose to attempt using the UiO logo as pattern. This was challenging, since one step of the lithography process requires dissolving the photoresist in water – and LiF also readily dissolves in water. The obtained feature sizes are thus quite large, but nevertheless illustrate how $MoCl_4O$ can be used to selectively deposit MoO_x (Figure 6.7).

Figure 6.6. Selectivity of $MoCl_4O$ + (H_2O + O_3) estimated by EDS on glass vs Si(100) as function of temperature, using 1000 ALD cycles.

Figure 6.7. SEM micrograph of MoO_x deposited on a patterned LiF thin film. The pattern resembles the UiO logo.

6.3 Deposition of $CaMoO_4$

Having established a process for molybdenum containing compounds, the next step was to combine it with $Ca(thd)_2 + O_3$ in an effort to deposit $CaMoO_4$ on Si(100). Considering that the molybdenum process did not grow well on $CaCO_3$, we were open for all types of outcomes when combined with the $Ca(thd)_2 + O_3$ process. Some initial experiments were performed, listed below;

(i) A pulsed ratio of 1:1 between Mo and Ca gave a huge surplus of molybdenum (around 80 mol% Mo vs Mo+Ca) , and showed no signs of $CaMoO_4$ in the diffractograms.

(ii) Increasing the pulsing ratio to 1:2 or 1:3 of Mo:Ca increased the content of calcium to a small surplus and showed signs of $CaMoO_4$ in the diffractograms.

(iii) Annealing the films obtained in (ii) at 1000 °C for one hour gave rise to unwanted molybdenum silicate phases.

From (i) and (ii) it follows that the relationship between pulsed and obtained composition in the final product is far from linear for this system. Fortunately, (ii) gave hope that the deposition of $CaMoO_4$ could be possible using $MoCl_4O$ and $Ca(thd)_2$ as metal precursors, but the pulsed ratio, deposition temperature and possible post-annealing required optimization. In order to maximize the amount of information from a limited number of experiments, DoE was used.

6.3.1 Optimization through central composite design

A significant part of the job when performing a DoE experiment, is to design the experiment itself. First and foremost, we have to decide if a screening or optimization will be performed. This is not as straightforward as it sounds. The major argument for a screening design, is that the process was unexplored prior to this work. From a statistician's point of view screening and optimization differs in how the number and level of input variables are chosen, where screening experiments in general study many input variables, but at a limited number of levels (e.g. two, for example annealing at 600 or 800 °C) and optimizations study fewer input variables, but at more levels. The *resolution* of optimizations is thus higher. We prioritized high resolution and only four input variables for the current work, and hence the toolbox for optimization. A face-centered CCD was chosen over a Box-Behnken design, prioritizing a larger data-density in the central part of the experimental region. A fairly narrow range of pulsed compositions was chosen, but a larger range of deposition temperatures and annealing parameters. The experimental ranges are given in Table 6.3.

Table 6.3. Input variables with ranges used in CCD experiment to optimize deposition of $CaMoO_4$. Taken from Paper II.

Input variable	**Minimum (coded -1)**	**Maximum (coded 1)**
Deposition temperature (°C)	300	400
Pulsed % of Mo	25	33
Anneal temperature (°C)	425	800
Anneal time (min)	0	30

Characterization of the composition, crystallinity and photoluminescence was chosen as quantifiable results. EDS was used to investigate the composition, although less accurate than for example XRF, but more convenient for many samples as it also accepts smaller sample sizes in contrast to XRF. The PL data was quantified by integrating the area under the curves. In a similar manner, the XRD data was quantified performed using Pawley refinements, as described in sub-chapter 5.3.1.

Figure 6.8 shows Pareto charts of what effects the various input variables (factors) have on the measured responses. Effects larger than the red dotted line are considered statistically significant for a confidence level of 95 % (95 % is a typical confidence level for DoE types of experiments). As can be seen from Figure 6.8, only the composition shows significant effects, where the deposition temperature and the secondary effect between deposition temperature and pulsed % Mo are significant. Looking into the raw data, it can be seen that certain depositions only yield $CaCO_3$, for example several at 400 °C. This yields a large deviation on the measured composition and thus show the importance of deposition temperature as an input factor with respect to the composition. Terms containing the deposition temperature are also most important factors for the crystallinity.

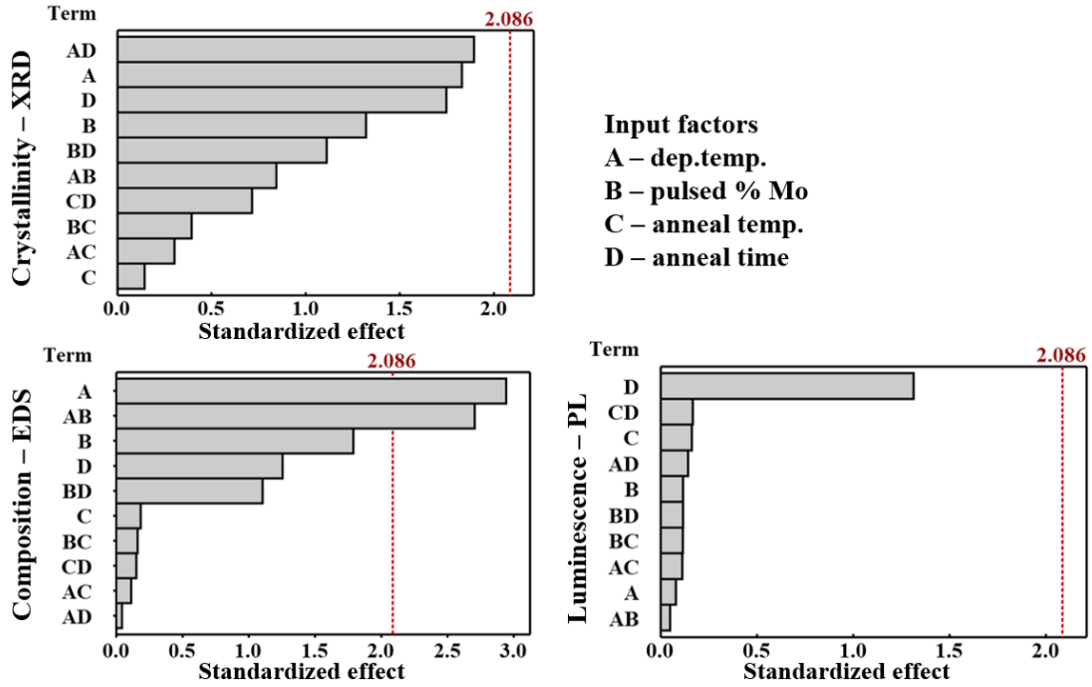

Figure 6.8. Pareto charts showing the direct and secondary standardized effects of the input variables on the three responses. This is a typical way of displaying data from DoE experiments[248]. The red dotted line at 2.086 denotes if the effects are indeed statistically significant or not. Taken from Paper II.

Although Figure 6.8 provides the significance of the different factors, it does not provide insight into the optimal values of the variables. This is typically visualized in main effect plots (Figure 6.9)[249-251]. The PL intensity is at maximum for a deposition temperature of 350 °C. The XRD signal decreases somewhat with deposition temperature. This is best explained when viewing the details of the raw data. The main effect plots are based on averages of several samples. A number of the samples deposited at 400 °C contained only $CaCO_3$ and were thus failed experiments. This is also seen for the measured composition, as the average Ca-content at 400 °C is very high. For the pulsed % Mo, the middle value, aka the center point, which correspond to 29 pulsed % Mo, is best in terms of composition, crystallinity and luminescence. Figure 6.9 moreover shed light on the annealing parameters. Surprisingly, the annealing temperature does not seem to be very important – despite ranging from 400 to 800 °C. For the crystallinity and the composition, the annealing time also has a limited effect. The annealing time is more important for the luminescence, where no annealing at all is in fact better than annealing for 15 minutes. This suggests an ongoing crystal reorganization in the films, and that annealing for 15 minutes is not sufficient to complete this process. The most luminescent samples are obtained when annealing for 30 minutes. This made us decide to attempt longer annealing times when optimizing the annealing step for the $CaMoO_4$: Pr^{3+} system.

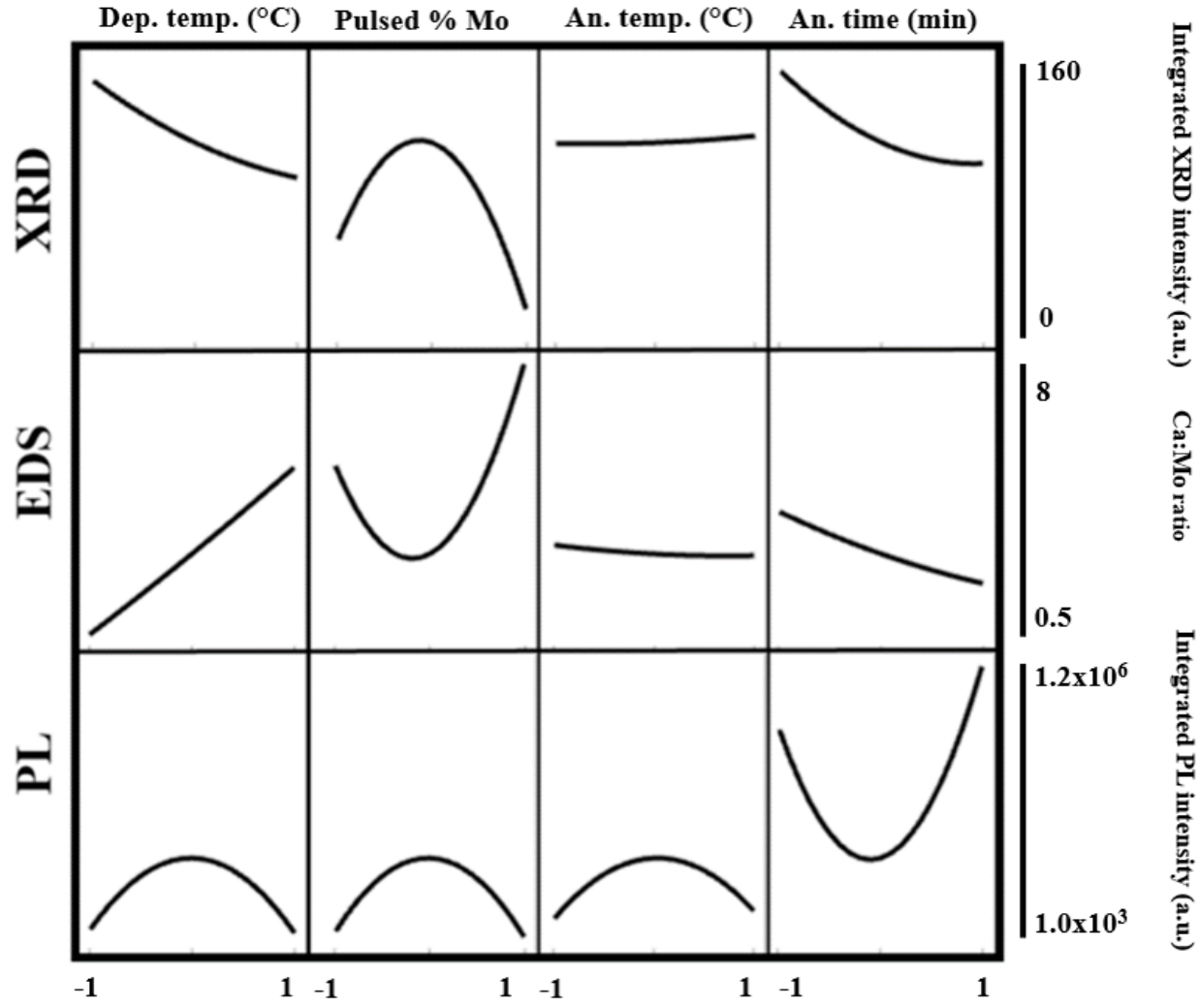

Figure 6.9. Main effect plots showing mean values of all the measured responses (XRD, EDS, PL) for the various levels of the coded (−1 to 1) input parameters (dep. temp., pulsed % Mo and annealing temp. and time). The middle of each x axis represents coded value 0 for each input variable. Taken from Paper II.

Looking further into the raw data behind the Figures 6.8-9, we see that the single most luminescent sample actually deposited was made at 350 °C, using 29 pulsed % Mo and annealing at 800 °C for 15 minutes. The experimental design used here did unfortunately not include a sample deposited at 350 °C, using 29 pulsed % Mo and annealing at 800 °C for 30 minutes, showing that DoE can suggest optimal conditions outside the investigated range. All samples using these deposition parameters (at 350 °C and 29 pulsed % Mo) were crystalline and luminescent and had compositions close to the desired. We therefore concluded that these ALD parameters were the most suitable, while the annealing parameters required further optimization.

6.3.2 $CaMoO_4$ growth characteristics

Figure 6.10a shows the growth per cycle (GPC) as a function of deposition temperature and pulsed composition. The GPC for 25 or 33 pulsed % Mo follows the same dependency of deposition

temperature, with only a minor variation with temperatures, whereas the 29% pulse Mo increases notably with temperature. Such high sensitivity of GPC with pulsed composition is rare and points at a significant composition. To conclude, 29 % pulsed Mo yields the highest content of the desired $CaMoO_4$ phase, also with a higher growth rate than the competing processes for $CaCO_3$ and $CaMoO_3$. For both 25 and 33 pulsed % Mo signs of aragonite and calcite are found in the diffractograms.

Figure 6.10b shows XRD data for samples deposited at 300, 350 and 400 °C, all using 29 % pulsed Mo. The sample deposited at 400 °C contains only $CaMoO_4$, but not very crystalline. Depositions at 350 °C yielded a mixture of $CaMoO_4$, $CaMoO_3$ and calcite, and peaks from all these phases were also obtained when 300 °C was used. Do note that the peak ratios, also from the same phase, vary – indicative of different kinds of oriented growth.

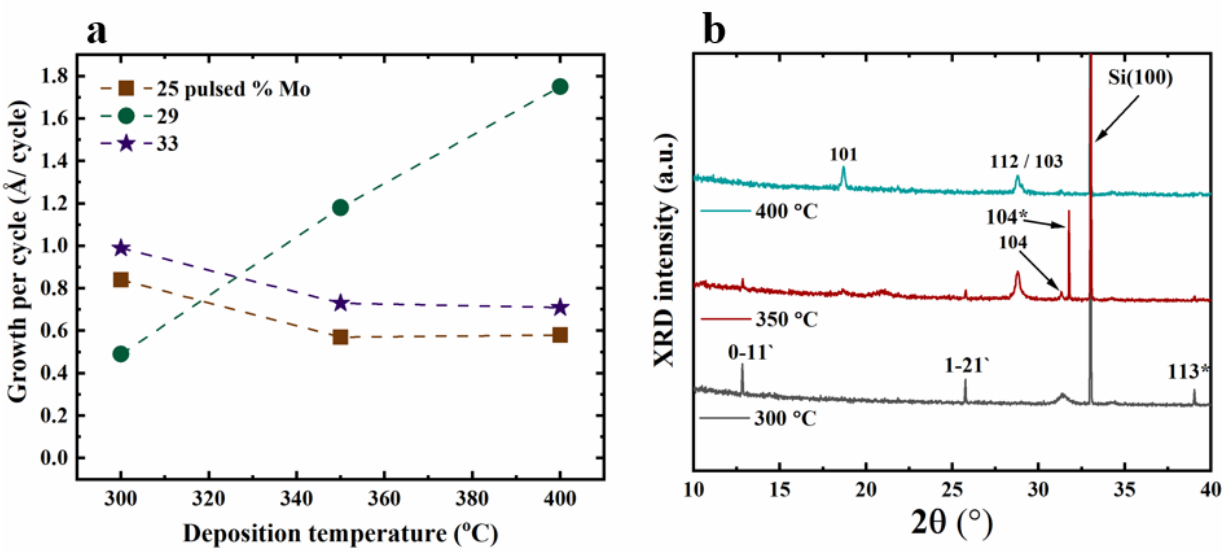

*Figure 6.10. Growth per cycle (GPC) as a function of deposition temperature and pulsed composition (a, left) and diffractograms as a function of temperature for samples deposited using 29 pulsed % Mo (b, right). Unmarked indexed XRD peaks refer to the desired $CaMoO_4$ phase, whereas ` and * refer to $CaMoO_3$ and calcite, respectively.*

Further characterization was performed on samples from the center point of the experimental design. Several of these samples were measured with a variety of techniques, but as they were all very similar, representative data is shown in Figure 6.11. The BSE-SEM micrograph is almost featureless, indicating that a single phased product is obtained. The AFM micrograph does, however, reveal some topography, with a RMS of 16 nm for a 114 nm thick sample. Pawley refinements unveiled crystallite sizes of 30 - 40 nm. In contrast to the diffractograms of the as deposited thin films (Figure 6.10b), the diffractogram for the annealed sample in Figure 6.11d only shows peaks of the desired $CaMoO_4$ phase.

The UV-VIS transmission data should be viewed in the light of an application as a host for solar down converters. The silicon solar cell will efficiently utilize light with wavelengths up to around 1100 nm. Down-converters should absorb in regions with half of this wavelength or less, and be transparent for longer wavelengths[73]. Figure 6.11c shows that the obtained films are mostly transparent for

wavelengths longer than 350 nm, while absorbing strongly around 275 nm. Despite this, we have been able to measure luminescence with a 405 nm laser as the excitation source, meaning that some light is indeed absorbed also here.

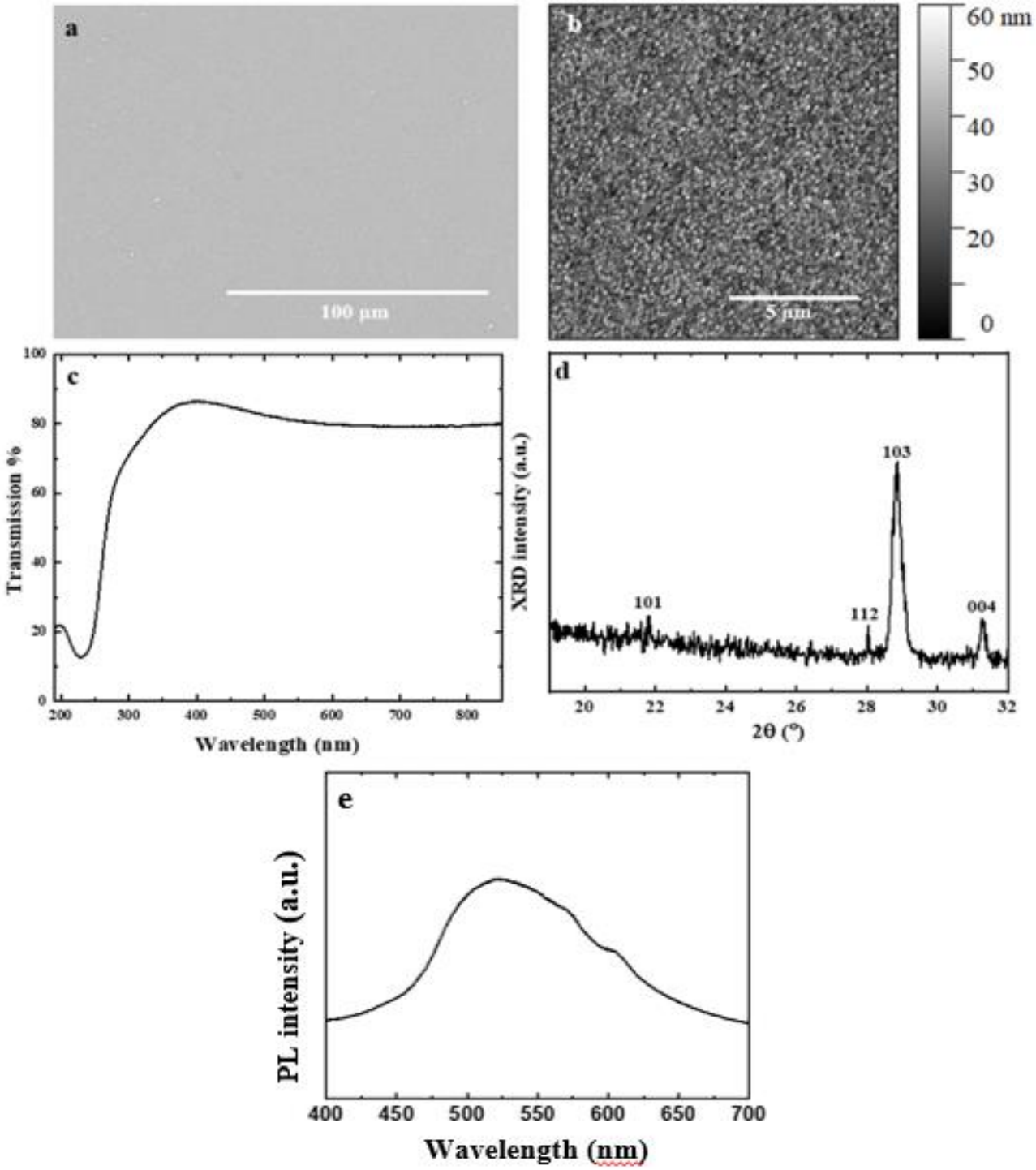

Figure 6.11. BSE-SEM micrograph (part a, top left), AFM micrograph (part b, top right) and $CaMoO_4$-indexed XRD diffractogram (part d, middle right) of a $CaMoO_4$ thin film deposited, annealed at 612.5 °C for 15 min., corresponding to the center point of the experimental design. UV-VIS transmission spectrum of a $CaMoO_4$ thin film on silica (part c, middle left) and PL emission spectrum of $CaMoO_4$ annealed at 800 °C for 60 min. All samples were deposited at 350 °C using 29 % pulsed Mo.

6.4 Deposition of $CaMoO_4$: Pr^{3+}, Yb^{3+}

The obtained process for deposition of $CaMoO_4$, was expanded to include the Pr^{3+} and Yb^{3+}-dopants. A highly luminescent, crystalline film, dominated by Pr^{3+} luminescence over emissions stemming from the host, was coveted prior to co-doping with Yb^{3+}, as we believed that the energy transfer would be from the host to Pr^{3+} to Yb^{3+}. The process needed to be optimized in terms of annealing conditions and design of doping levels. Pr^{3+} is prone to concentration quenching, so high doping levels are usually ill-favored. ALD does have an advantage over other synthesis methods here, since the position of the dopants can be controlled in the growth direction of the film. In the current work the $Pr(thd)_3$ pulses are spread out as much as possible to minimize concentration quenching. As the investigations on $CaMoO_4$ were not completely conclusive with respect to the optimal annealing conditions, we investigated annealing in the range 600 to 800 °C for 30 to 60 minutes annealing time with a three-level two-factorial full factorial design. The design was replicated for five different doping levels of Pr^{3+}.

6.4.1 Optimizing deposition of $CaMoO_4$: Pr^{3+}

$CaMoO_4$ films doped with 0.5 – 1 – 2 – 4 – 8 % Pr^{3+} were made. Due to occurrence of some gradients, only samples situated centrally in the ALD chamber, where even film was obtained, were annealed and characterized.

From Figure 6.12 it becomes apparent that using 1 % Pr and annealing at 800 °C for 1 hour yields the most intense Pr^{3+}-luminescence, as seen by the high intensities at 490 and 610 nm compared to the background from the host. Some luminescence from the host with the broad peak around 525 nm is also seen for most of the spectra. It should be noted that observing Pr^{3+} luminescence for doping levels as high as 8 % Pr^{3+} is unusual, and may be possible due to the nature of the ALD growth, where $Pr(thd)_3$ is pulsed as individual layers. Assuming that the Pr^{3+} ions are distributed equidistant in the growth direction of the film, there is around 16 nm between each Pr^{3+}-containing layer when 1 % $Pr(thd)_3$ is used. For the samples with 8 % Pr^{3+}, this distance is around 2 nm, short enough for concentration quenching through FRET to be likely. For all cases, the Pr^{3+} will though be separated in plane by the size of the thd-ligands and how these pack on the surface.

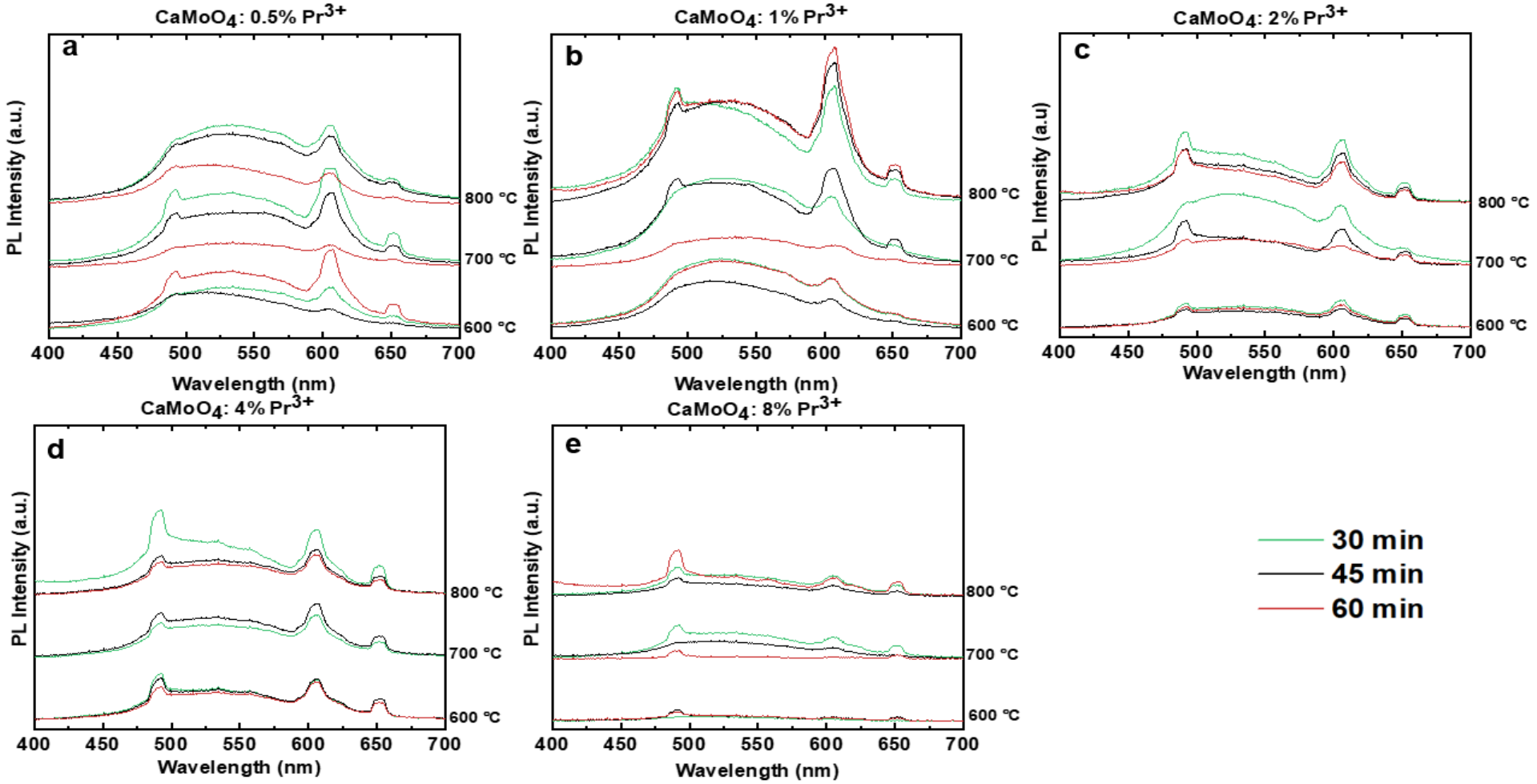

Figure 6.12. PL spectra of $CaMoO_4$: x% Pr^{3+}, annealed at 600, 700 or 800 °C for 30, 45 or 60 min. A 280 nm diode was used as an excitation source and the spectra were recorded with a USB2000+ modular spectrometer. Part a, b, c, d and e show PL spectra for $CaMoO_4$:0.5 % Pr^{3+} $CaMoO_4$:1 % Pr^{3+} $CaMoO_4$:2 % Pr^{3+} $CaMoO_4$:4 % Pr^{3+} and $CaMoO_4$:8 % Pr^{3+}, respectively. Taken from Paper III.

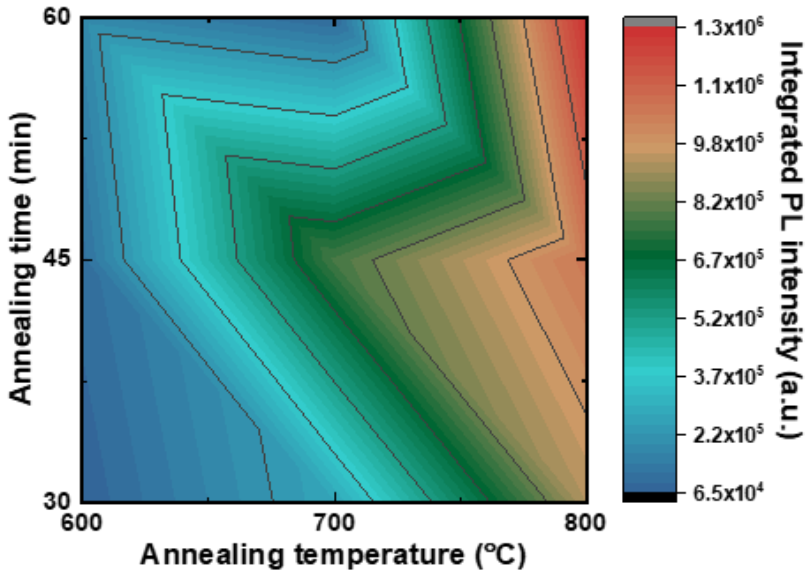

Figure 6.13. Contour plot of integrated intensities of the Pr^{3+} PL peak at 605 nm versus annealing time and annealing temperature. The host luminescence is subtracted as a background using a built-in function in Origin. The integrated range was from 587 to 635 nm. The PL measurements were performed with a 280 nm diode as excitation source and the spectra were recorded with a USB2000+ modular spectrometer. The raw data is found in Figure 6.12b. Taken from Paper III.

For the $CaMoO_4$: 1 % Pr^{3+} samples, the integrated intensities (excluding the host emission) below the peak at 605 nm (from 587 to 635 nm) was further examined in hope of gaining understanding of the importance of the annealing parameters. The integrated intensities were plotted against annealing time and temperature, to attain a contour plot, another typical method to portray DoE-data[250, 251]. From Figure 6.13 it can be deducted that the annealing temperature is more significant for the integrated PL intensity than the annealing time.

The full set of annealed $CaMoO_4$: x% Pr^{3+} samples were also investigated by XRD, $CaMoO_4$: 0.5 % Pr^{3+} shown in Figure 6.14a. Only two crystalline phases were found; the desired $CaMoO_4$-phase for the majority of the samples and monoclinic Pr_5O_9 in a single sample (for $CaMoO_4$: 4% Pr^{3+} annealed at 800 °C for 45 min, see Supplementary Material for **Paper III**). The highly doped samples (8 % Pr^{3+}) were the least crystalline. Note that these samples also showed the lowest host luminescence. The peak positions with respect to doping level are compared in Figure 6.14b. This comparison show that the $CaMoO_4$ structure is able to dissolve around 2 % Pr^{3+}, but not more. Excess Pr may be present as an oxide, but in too small quantities to detect by this XRD investigation.

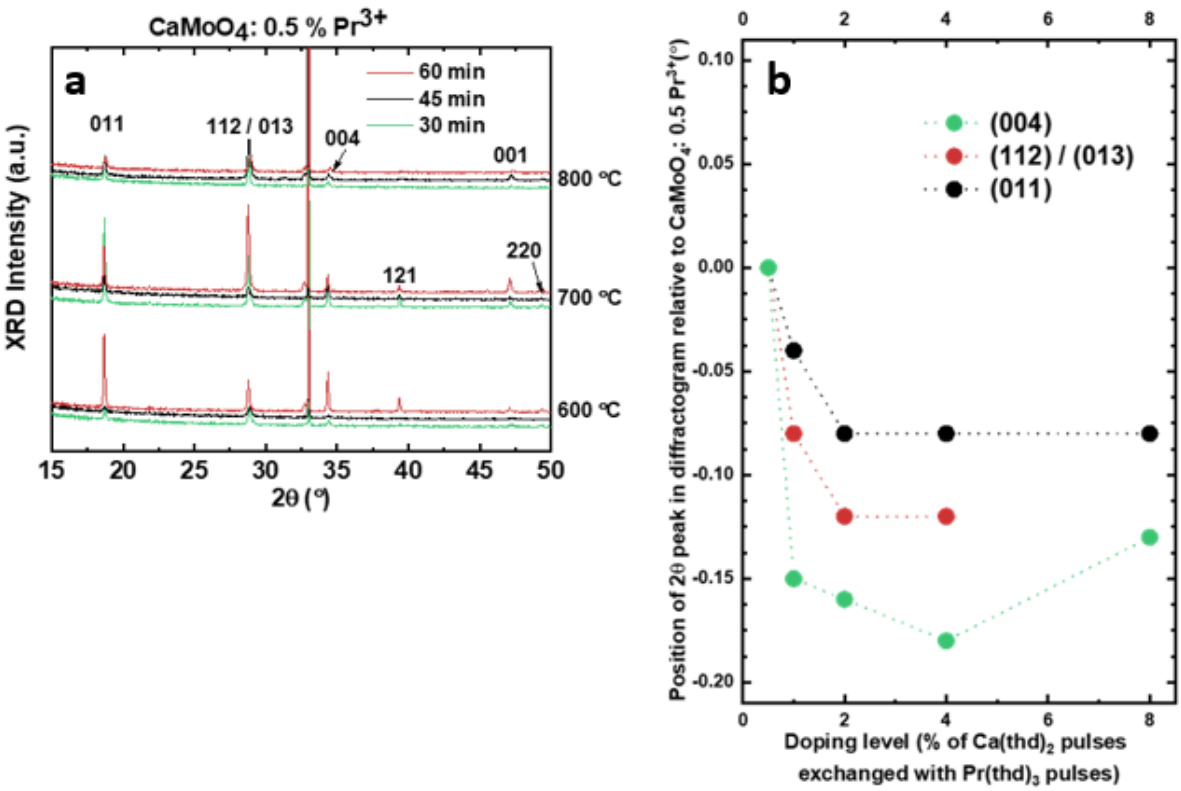

Figure 6.14. XRD diffractograms of $CaMoO_4$: 0.5 % Pr^{3+}, annealed at 600, 700 or 800 °C for 30, 45 or 60 min (part a, left). The intense peak around 33° in all plots is the (200) reflex from the silicon substrate. Position of 2θ XRD peaks in diffractograms relative to the peak for $CaMoO_4$: 0.5 % Pr^{3+} with respect to doping level (part b, right). The samples compared in part b are all annealed at 800 °C for 1 hour. Both parts taken from Paper III.

6.4.2 Deposition of $CaMoO_4$: Pr^{3+}, Yb^{3+}

After establishing that using 1 % Pr^{3+} and annealing at 800 °C for 60 minutes yielded the most luminescent samples, $CaMoO_4$ doped with both Pr^{3+} and Yb^{3+} was deposited and annealed under the same conditions as the most luminescent $CaMoO_4$: 1 % Pr^{3+} sample. The number of $Yb(thd)_3$ pulses versus the total number of $Ca(thd)_2$ + $Pr(thd)_3$ + $Yb(thd)_3$ pulses was varied from 1 – 2 – 4 – 8 %. The amount of $Pr(thd)_3$ was retained at 1 %. The $Yb(thd)_3$ pulses were spaced out as much as possible in the matrix to minimize the effect of concentration quenching. For the lowest doping level, 1 %, the distance between the $Pr(thd)_3$ and $Yb(thd)_3$ pulse was varied, from neighboring pulses to the maximum spacing, around 8 nm assuming equidistant lanthanide-doped layers. Although not being very well crystalline, the diffractograms in Figure 6.15 show presence of $CaMoO_4$ for all the co-doped samples and no other peaks are seen.

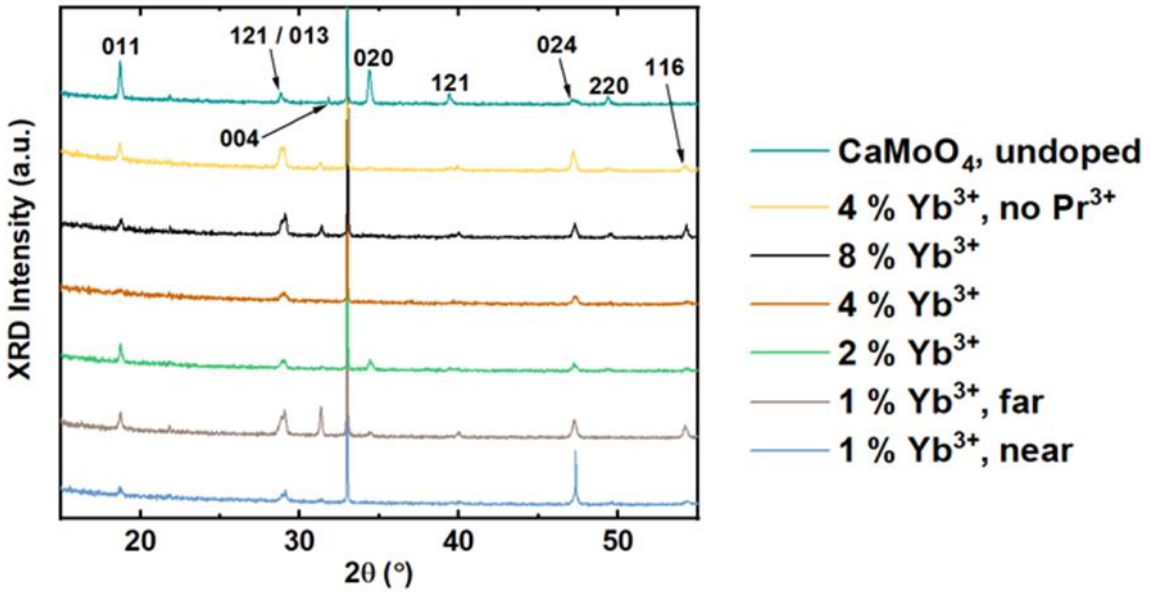

Figure 6.15. XRD diffractograms of $CaMoO_4$: Pr^{3+}, Yb^{3+} samples. The diffractograms denoted with "x% Yb^{3+}" are all co-doped with 1% Pr^{3+}. Near and far indicate whether the $Yb(thd)_3$ ALD pulse is close to or far away from the $Pr(thd)_3$ ALD pulse. The indexed peak positions correspond to the desired $CaMoO_4$ phase. The intense peak around 33° in all plots is the (200) reflex from the silicon substrate. Taken from Paper III.

Figures 6.16a,b show that using 8 % Yb^{3+} yields the most Yb^{3+} luminescence, as seen from the peak at 978 nm. Comparing the position of the host emission to the un-doped sample (Figure 6.11e) shows that the position of the host emission is not changed upon doping. The 1 – 4 % Yb^{3+} co-doped samples all have around the same intensity for the Yb^{3+} luminescence around 978 nm Mono-doped samples are shown in part c. There are clearly stronger Pr^{3+} peaks when no Yb^{3+} is added in the matrix, indicating transfer from Pr^{3+} to Yb^{3+}, but the intensity of the Pr^{3+} peaks appear independent of Yb^{3+} concentration if Yb^{3+} is present. However, we also observe direct transfer from the host to Yb^{3+}, as seen from the Yb^{3+} luminescence in Figure 6.16c at 978 nm when no Pr^{3+} is present. This is a possibility not previously considered in the literature. The direct transfer from the host to Yb^{3+} will be competing with the possible down-conversion process through cross-relaxation also involving Pr^{3+}.

Figure 6.16d shows PL spectra for $CaMoO_4$: 1% Pr^{3+}, 1% Yb^{3+}, at different relative positions between the dopants. It shows that increasing the distance between Pr^{3+} and Yb^{3+} indeed decreases the PL intensity of the Yb^{3+} peak, pointing towards FRET between the ions being less effective at long distances, a proof of Pr^{3+} to Yb^{3+} transition. It also shows less host luminescence when Yb^{3+} and Pr^{3+} are close. If this is due to a less crystalline material when the dopant ions are far apart, is difficult to judge from the XRD data (Figure 6.15). The peak around 490 nm corresponding to emission from the $^3P_0$ level of Pr^{3+} is visible when Yb^{3+} and Pr^{3+} are embedded far apart, but not when they are close. The $^3P_0$ level is crucial for down-conversion between Pr^{3+} and Yb^{3+}, since energy is transferred from there

to Yb^{3+}. The presence of a peak around 490 nm when Pr^{3+} and Yb^{3+} are far apart, is indicative of a less efficient FRET between Pr^{3+} and Yb^{3+} when the distance between them increases. Note that the intensity of the Pr^{3+} peaks appear constant regardless of distance between Pr^{3+} and Yb^{3+}.

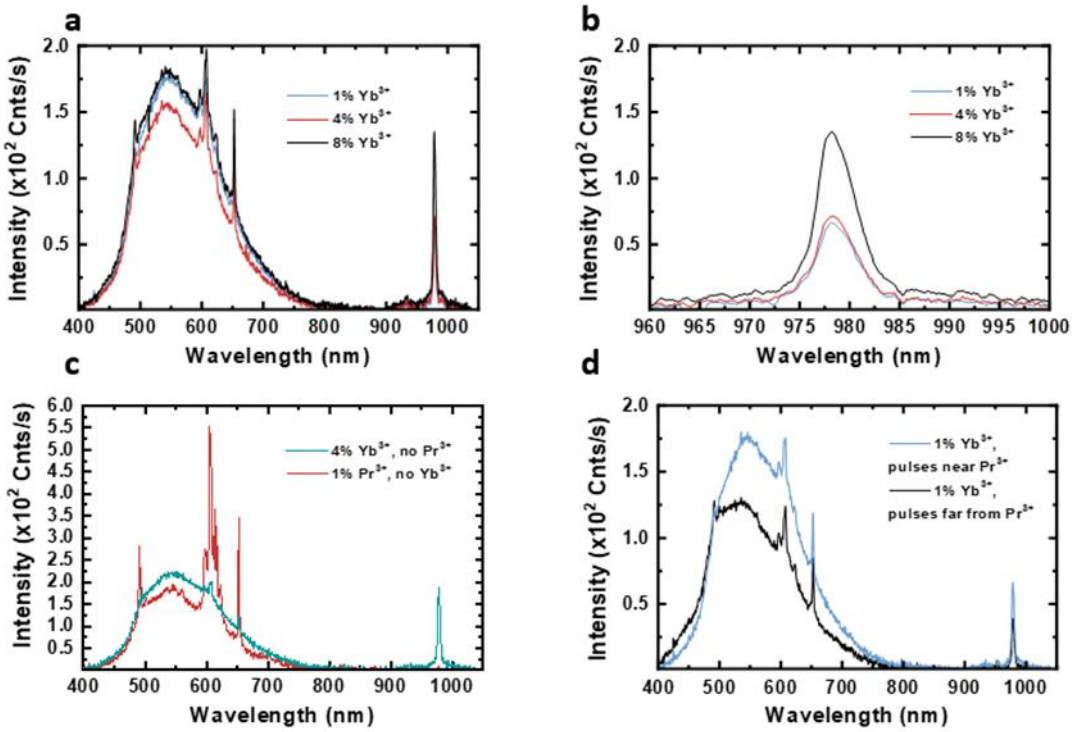

Figure 6.16. PL spectra of $CaMoO_4$ doped with either Yb^{3+}, Pr^{3+} or both. All samples are annealed at 800 °C for 60 min. A 325 nm HeCd laser was used as an excitation source, and the spectra were recorded with a USB4000+ photospectrometer. The spectra denoted with "x% Yb^{3+}" are all co-doped with 1% Pr^{3+}. Near and far indicate whether the $Yb(thd)_3$ ALD pulse is close to or far away from the $Pr(thd)_3$ ALD pulse. Part a shows PL spectra for four selected co-doped samples with varying Yb^{3+}-content. Part b shows the same data as part a, but only in a desired region, in order to highlight the varying intensity of the Yb^{3+} emission around 980 nm. Part c shows PL spectra for mono-doped $CaMoO_4$ samples. Please note the different y-scale in this graph. Part d show PL spectra for two co-doped $CaMoO_4$: 1 % Pr^{3+}, 1 % Yb^{3+} samples, but with different relative positions of Pr^{3+} and Yb^{3+} in the matrix. Taken from Paper III.

6.5 Reflections

More than once through this work, in particular during lonely lab-hours when the ALD-reactor had to be dismantled, I have asked myself the question "why on Earth am I doing this?". (Un)fortunately, we do not have to look far to regain motivation. Yesterday, a stormy September night, we had to secure our outside belongings from yet another storm, while earlier this week it was so dry that the forest nearby spontaneously caught fire. The climate is changing right in front of us. Finding greener alternatives for energy is paramount to combat a change to the worse.

With the urgency of the ongoing climate change, an intuitive reaction is that the scientific fields working on paths out of our current crisis, should really speed up. Rushing science is not good, whether it is on

better lithium ion-batteries or a vaccine for COVID-19, as it increases the probabilities of overlooking important results or creating errors. However, there are strategies for researching more thoroughly also with a reduction in the number of experiments. It all comes down to experimental planning. In this work, DoE from the statistical toolbox, has been used to research faster and better. Personally, the contrast between the number of experiments required to produce fruitful results between preparing **Paper I** and **Paper II & III**, is stark. For me, using DoE, has forced more thorough experimental planning on an early stage and slashed the number of required experiments.

In addition to providing the actual results on the development of the $CaMoO_4$ process, **Paper II** aimed at being a tutorial for other ALD-scientists developing complex systems where many factors require simultaneous tuning. Todays' usage of statistical tools in material science is in my point of view far too limited, and as ALD-systems increase in complexity we should familiarize ourselves with more systematic methods of process optimization. In the ALD-field it has up to now been almost completely absent[152, 153], even though we often statistically analyze our results. The current COVID19-situation with the overhanging threat of lab-lockdowns, further emphasize the importance of thorough experimental planning. A major hope for this work, is that especially chapter 3.3.1 on Design of Experiments should be widely read. There is currently some movement in the field, and DoE has recently been successfully combined with machine learning[252]. DoE-inspired machine learning has also been used alone[253-255]. I believe these types of studies will be more plentiful in the not so far future, as especially artificial intelligence is a hot research topic. A possible outcome of the combination of DoE and machine learning may be more sophisticated experimental designs taking complex material systems with many possible outcomes into account.

A reason into why it is easy to get lost when researching new ALD-processes and using methods to plan experiments is wise, is also the thing I adore most about ALD, namely the close-to endless possible combinations to produce novel materials. I highly prize how easy it is to combine different material classes and how many precursors we have available. For the ALD-scientist, the periodic table is like a playground, and the question is turning more into what materials it makes sense to make. In this work, exploring $CaMoO_4$ as an absorbing host for down-conversion coatings for silicon solar cells, is sensible, as it absorbs in the desired region and was thought compatible with the Pr^{3+} / Yb^{3+} down-conversion pair. I anticipate that more of the future ALD-research will be on "what should we make" rather than "how can we make it", as the latter becomes easier through developments like the establishment of the $MoCl_4O$ + (H_2O + O_3) process (**Paper I**). Finding meaningful materials to deposit do require a higher level of expertise in other fields than just ALD itself.

I believe that exploiting ALD to attain complex materials or utilizing the possibility of positional control of dopants is just in its infancy, although our group has demonstrated several works utilizing this type of control recently[105, 256]. An intrinsic challenge when attempting to control the dopant

concentration of structures made by ALD, is that the dopant concentration in planes corresponding to the dopant pulse may be too high and similarly too low far away from the dopant pulse, for the desired application. One strategy to counter this is post-deposition annealing and/ or using higher deposition temperatures, both increasing the mobility of the ions in the film. A more sophisticated approach is the use of an inhibitor pulse prior to the dopant pulse, allowing a smaller fraction of the dopant precursor molecules to adsorb and thus a lower in-plane concentration of dopants. Ethanol has for example been used as an inhibitor prior to the trimethylaluminium (TMA)-pulse to reduce growth of Al_2O_3 from TMA and O_3[257]. Although this was not for a doped structure, it illustrates the possibility of using inhibitors to reduce the growth rate in a controlled manner.

In relation to this it should be re-mentioned that despite it not being utilized in the current work, organic building blocks may also be used in ALD. Organic-inorganic hybrid ALD is maturing as a field and many organic precursors are available. This can allow for using a dye-sensitization strategy for down-converting systems made by ALD, not relying on an absorbing host such as $CaMoO_4$. In general, strongly absorbing materials are important when the materials are as ultrathin films, so it can be assumed that incoming light indeed is absorbed. Organic dyes are often strongly absorbing. For example is the most intense luminescence observed in our laboratory from benzendicaroxylate-Tb organic-inorganic hybrids.

A last reflection upon this work, is on if it was all worth it. On a personal note, the answer is an overwhelming yes, as pursuing a phd is an once in a lifetime-learning experience. In particular, dealing with involuntarily home-schooling, two preschoolers to occupy whilst writing up papers and performing the final required experiments with a partially closed lab, has been the kind of once in a lifetime-experience I never wish to repeat, but has taken my skills in time-management and ability to persevere, to a whole new level. On a strictly scientific note, I am filled with more uncertainty if it was worth it, as we are still far from having a prototype silicon solar cell with a down-conversion coating ready for mass production. My hope is that my colleagues will continue to study the doped $CaMoO_4$ films when performing in-device testing on actual silicon solar cells, and that the samples produced for **Paper III** will be taken along when travel to collaborators with more advanced optical test equipment is allowed. I also think this work has substantially added to the consciousness on experimental planning in our group, and I know that DoE methods are currently being used in other projects at NAFUMA. To conclude, valuable knowledge has come out of this work, but there is still plenty of remaining work to attain a functional device.

7. Concluding remarks

The overall aim of this work has been to develop a process for deposition of down-converting $CaMoO_4$ doped with Pr^{3+}, Yb^{3+} by ALD. Although deposition of the material itself was achieved, the development has still opened for several other research directions, and there are also possibilities for further characterization of the obtained samples. The available characterization methods could not determine whether the samples indeed were down-converting or not.

The initial process developed in this work, was the area-selective $MoCl_4O$ + (O_3 + H_2O) process. This was the first reported area-selective process for MoO_x and usage of $MoCl_4O$ as an ALD-precursor, and moreover one of only a few reported oxychlorides used to deposit oxides[239, 240]. Bergum et al. had previously described usage of WCl_4O in combination with H_2O to deposit WO_3, but the process seemed to stop after a few cycles according to their QCM data[238]. The current work opens for more investigations of WCl_4O as an ALD-precursor as well, as this may also lead to area-selective deposition of WO_3 on selected surfaces when it is combined with H_2O and O_3. Area-selective deposition of WO_3 may be beneficial for fabrication of proposed devices such as sensors[258], as a photo-catalyst or in the emerging application as antimicrobial surfaces[259].

The possible role of $MoCl_4O$ as a Mo-source for deposition of other complex Mo-oxides must also be emphasized. Although it should be kept inert, $MoCl_4O$ is easily handled as it does not require heating above room temperature. Moreover, it may be utilized from at least 200 to 400 °C, which is the full investigated span here, meaning that it can potentially be combined with many other ALD precursors, in addition to $Ca(thd)_2$, $Pr(thd)_3$ and $Yb(thd)_3$ tried here. Possible future complex Mo-oxides where $MoCl_4O$ may be used, include investigated catalysts such as Mo-V-Te-Nb-O[260, 261] or $A_2Mo_3O_8$ (A = Co, Mn and Zn) as an anode material for lithium ion batteries[262]. There are also other possible functional scheelites that could be deposited in addition to $CaMoO_4$, such as $SrMoO_4$ or $BaMoO_4$[193]. Studying what chemistries $MoCl_4O$ would be compatible with and not, can possibly shed more light on the reasons behind its substrate selectivity. How suitable $MoCl_4O$ is to deposit other complex oxides cannot be determined without actually trying.

The ALD-process to deposit $CaMoO_4$ was well-optimized using DoE in this work. The development revealed a system highly sensitive towards the pulsed composition. A major drawback with this sensitivity concerning using this process on an industrial scale, is that it requires supreme control of the gas flows in the reaction chamber. The larger the substrates and thus reaction chamber, the more difficult it is to attain this level of control. The sensitivity alongside with the selectivity of the binary system, are challenging to fully explain. The ternary system is also sensitive towards deposition temperature, together pointing towards packing density and distribution of beneficial configurations of the precursors on the surfaces being important factors[146].

In this work, DoE was also used to optimize the annealing conditions for $CaMoO_4:Pr^{3+}$. Previous studies on $CaMoO_4:Pr^{3+}$ have lacked a systematic approach to study both the doping levels and annealing conditions[21, 112, 176, 263, 264]. We here show that the latter also have an influence on the luminescence and therefore should not be neglected. As using $CaMoO_4$: 1 % Pr^{3+} and annealing at 800 °C for 60 min. gave the most Pr^{3+}-luminescence, this was used as a foundation for further doping with Yb^{3+}. The ratio of the Pr^{3+}/ Yb^{3+} emissions scaled with their relative concentrations. As a control, $CaMoO_4$: 4 % Yb^{3+} was also investigated. To our surprise, this sample showed the most Yb^{3+}-luminescence of them all, meaning that direct transfer from the host to Yb^{3+} is indeed taking place. In the existing literature on $CaMoO_4$-based materials as optical converters, there seems to be an assumption that this does not take place, without it actually being investigated[21, 265]. A major contribution from our work is that this possibility must also be considered. In practice, this implies that concentration quenching may not be the only reason for avoiding very high doping levels of Yb^{3+} in $CaMoO_4$, since more Yb^{3+} in the host also will increase the chance of direct transfer from $CaMoO_4$ to Yb^{3+}. A theoretical possibility is that there is CET between $CaMoO_4$ and Yb^{3+}, in which case the donating species, such as Pr^{3+} here, is redundant. Possible CET between $CaMoO_4$ and Yb^{3+} can be investigated by quantum efficiency measurements, i.e. by using an integration sphere. Quantum efficiency investigations should also be conducted on the $CaMoO_4$: Pr^{3+}, Yb^{3+} samples when this infrastructure becomes available again.

Another take-home message from this work, is that the positional control that ALD has of how the dopants are placed in matrix actually has an effect on the optical properties. ALD is a unique thin film technique with respect to this – and we do see more Yb^{3+} luminescence in samples were Yb^{3+} is embedded in close proximity of Pr^{3+}. This difference in PL intensity is there despite a quite harsh post-deposition annealing step, which could allow larger re-arrangements of the ions in the matrix in addition to crystallization. Moreover does the spreading of the $Pr(thd)_3$ pulses seem to prevent concentration quenching, as we observe that even samples with 8 % pulsed $Pr(thd)_3$ still show Pr^{3+} luminescence.

The work conducted is this thesis is summarized in Figure 7.1. All-in-all the goal of depositing $CaMoO_4$: Pr^{3+}, Yb^{3+} was achieved, also with an interesting side-path investigating the area-selective growth of MoO_x. The obtained samples can be further characterized and scaling this process up will be challenging as supreme flow-control is required. This should not discourage more investigations on the topic – it rather underlines the importance of it.

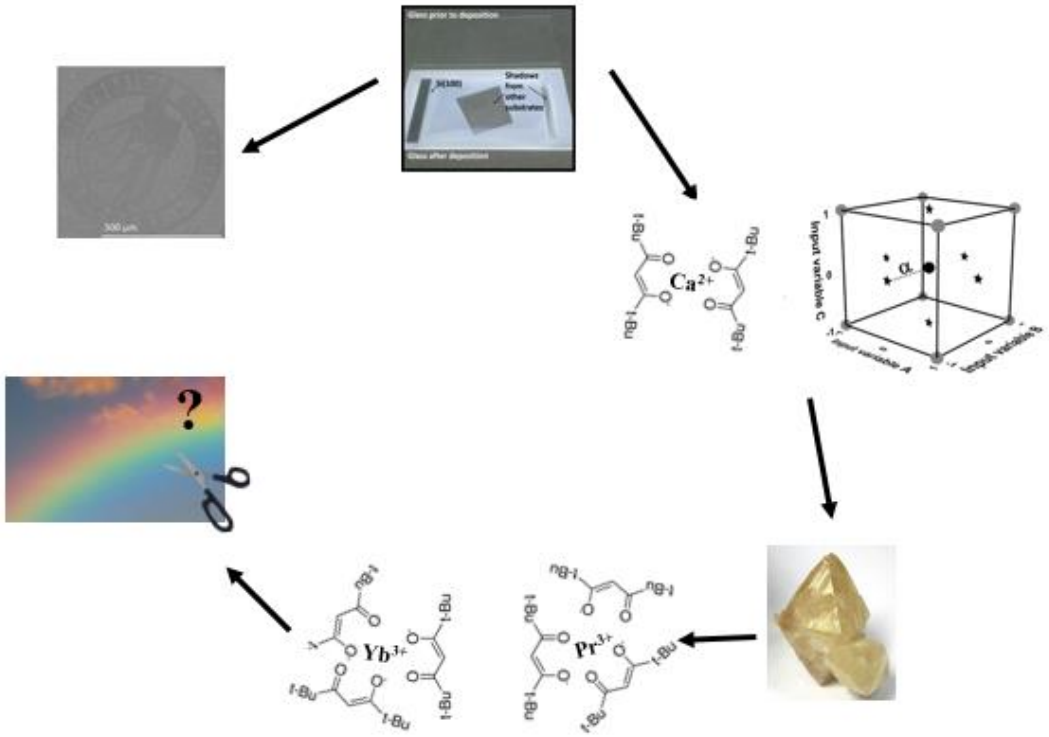

Figure 7.1. Graphical abstract of thesis, starting with $MoCl_4O$ as an ALD-precursor and area-selective growth of MoO_x, evolving towards deposition of possibly down-converting $CaMoO_4$: Pr^{3+}, Yb^{3+}.

8. References

1. IEA, *World Energy Outlook 2019*. 2019, IEA: Paris.
2. Owusu, P.A. and S. Asumadu-Sarkodie, *A review of renewable energy sources, sustainability issues and climate change mitigation.* Cogent Engineering, 2016. **3**(1): p. 1167990.
3. Taylor, S.R., *Abundance of chemical elements in the continental crust: a new table.* Geochimica et Cosmochimica Acta, 1964. **28**(8): p. 1273.
4. Nelson, J., *The Physics of Solar Cells*. 2003: Imperial College Press.
5. Shockley, W. and H.J. Queisser, *Detailed Balance Limit of Efficiency of p-n Junction Solar Cells.* Journal of Applied Physics, 1961. **32**(3): p. 510.
6. NREL. *https://www.nrel.gov/pv/cell-efficiency.html*. [cited 15.05.2020.
7. Richards, B.S., *Luminescent layers for enhanced silicon solar cell performance: Down-conversion.* Solar Energy Materials and Solar Cells, 2006. **90**(9): p. 1189.
8. Shalav, A., B.S. Richards, and M.A. Green, *Luminescent layers for enhanced silicon solar cell performance: Up-conversion.* Solar Energy Materials and Solar Cells, 2007. **91**(9): p. 829.
9. Ameri, T., N. Li, and C.J. Brabec, *Highly efficient organic tandem solar cells: a follow up review.* Energy & Environmental Science, 2013. **6**(8): p. 2390.
10. Essig, S., S. Ward, M.A. Steiner, D.J. Friedman, J.F. Geisz, P. Stradins, and D.L. Young, *Progress towards a 30% efficient GaInP/Si tandem solar cells.* Energy Procedia, 2015. **77**(NREL/JA-5J00-64775).
11. Gevaerts, V.S., A. Furlan, M.M. Wienk, M. Turbiez, and R.A. Janssen, *Solution processed polymer tandem solar cell using efficient small and wide bandgap polymer: fullerene blends.* Advanced Materials, 2012. **24**(16): p. 2130.
12. Nattestad, A., M. Ferguson, R. Kerr, Y.-B. Cheng, and U. Bach, *Dye-sensitized nickel (II) oxide photocathodes for tandem solar cell applications.* Nanotechnology, 2008. **19**(29): p. 295304.
13. Sugiura, H., C. Amano, A. Yamamoto, and M. Yamaguchi, *Double heterostructure GaAs tunnel junction for a AlGaAs/GaAs tandem solar cell.* Japanese journal of applied physics, 1988. **27**(2R): p. 269.
14. Werner, J., B. Niesen, and C. Ballif, *Perovskite/silicon tandem solar cells: Marriage of convenience or true love story?–An overview.* Advanced Materials Interfaces, 2018. **5**(1): p. 1700731.
15. Werner, J., C.-H. Weng, A. Walter, L. Fesquet, J.P. Seif, S. De Wolf, B. Niesen, and C. Ballif, *Efficient monolithic perovskite/silicon tandem solar cell with cell area> 1 cm2.* The journal of physical chemistry letters, 2016. **7**(1): p. 161.
16. Yamaguchi, M., K.-H. Lee, K. Araki, and N. Kojima, *A review of recent progress in heterogeneous silicon tandem solar cells.* Journal of Physics D: Applied Physics, 2018. **51**(13): p. 133002.
17. Richards, B.S., *Enhancing the performance of silicon solar cells via the application of passive luminescence conversion layers.* Solar Energy Materials and Solar Cells, 2006. **90**(15): p. 2329.
18. Nunzi, J.-M., *Requirements for a rectifying antenna solar cell technology.* Proceedings of SPIE - The International Society for Optical Engineering, 2010. **7712**.
19. Huang, H., J. Lv, Y. Bao, R. Xuan, S. Sun, S. Sneck, S. Li, C. Modanese, H. Savin, A. Wang, and J. Zhao, *20.8% industrial PERC solar cell: ALD Al2O3 rear surface passivation, efficiency loss mechanisms analysis and roadmap to 24%.* Solar Energy Materials and Solar Cells, 2017. **161**: p. 14.
20. Vermang, B., H. Goverde, A. Uruena, A. Lorenz, E. Cornagliotti, A. Rothschild, J. John, J. Poortmans, and R. Mertens, *Blistering in ALD Al2O3 passivation layers as rear contacting for local Al BSF Si solar cells.* Solar energy materials and solar cells, 2012. **101**: p. 204.
21. Verma, A. and S.K. Sharma, *Rare-earth doped/codoped CaMoO4 phosphors: A candidate for solar spectrum conversion.* Solid State Sciences, 2019. **96**: p. 105945.

22. Andrade, L.H.C., D. Reyes Ardila, L.B. Barbosa, J.P. Andreeta, M. Siu Li, A. Brenier, Y. Guyot, and G. Boulon, *Spectroscopic study of floating zone technique-grown Nd3+-doped CaMoO4.* The European Physical Journal - Applied Physics, 2005. **29**(1): p. 55.
23. Bai, W., Y. Liu, Y. Wang, X. Qiang, and L. Feng, *Cooperative down-conversion and near-infrared luminescence of Tb3+–Yb3+ co-doped CaMoO4 broadband phosphor.* Ceramics International, 2015. **41**(10, Part A): p. 12896.
24. Li, J., T. Zhang, G. Zhu, and Z. Hairong, *Up-conversion photoluminescence emissions of CaMoO4:Pr3+/Yb3+ powder.* Journal of Rare Earths, 2017. **35**(7): p. 645.
25. Li, S., Q. Meng, S. Lü, and W. Sun, *Optical properties of Sm3+ and Tb3+ co-doped CaMoO4 phosphor for temperature sensing.* Spectrochimica Acta Part A: Molecular and Biomolecular Spectroscopy, 2019. **214**: p. 537.
26. Li, X., M. Dong, F. Hu, Y. Qin, L. Zhao, X. Wei, Y. Chen, C. Duan, and M. Yin, *Efficient sensitization of Tb3+ emission by Dy3+ in CaMoO4 phosphors: Energy transfer, tunable emission and optical thermometry.* Ceramics International, 2016. **42**(5): p. 6094.
27. Marques, A.P.d.A., V.M. Longo, D.M.A. de Melo, P.S. Pizani, E.R. Leite, J.A. Varela, and E. Longo, *Shape controlled synthesis of CaMoO4 thin films and their photoluminescence property.* Journal of Solid State Chemistry, 2008. **181**(5): p. 1249.
28. Mikhailik, V.B., S. Henry, H. Kraus, and I. Solskii, *Temperature dependence of CaMoO4 scintillation properties.* Nuclear Instruments and Methods in Physics Research Section A: Accelerators, Spectrometers, Detectors and Associated Equipment, 2007. **583**(2): p. 350.
29. Ryu, J.H., J.-W. Yoon, C.S. Lim, W.-C. Oh, and K.B. Shim, *Microwave-assisted synthesis of CaMoO4 nano-powders by a citrate complex method and its photoluminescence property.* Journal of Alloys and Compounds, 2005. **390**(1): p. 245.
30. Yang, Y.-L., X.-M. Li, W.-L. Feng, W.-L. Li, and C.-Y. Tao, *Synthesis and characteristic of CaMoO4: Eu3+ red phosphor for W-LED by co-precipitation.* Journal of Inorganic Materials, 2010. **10**(25): p. 1015.
31. Penrose, R., *The mass of the classical vacuum.* The Philosophy of Vacuum. Clarendon, 1991.
32. Harder, J.W., G. Thuillier, E.C. Richard, S.W. Brown, K.R. Lykke, M. Snow, W.E. McClintock, J.M. Fontenla, T.N. Woods, and P. Pilewskie, *The SORCE SIM Solar Spectrum: Comparison with Recent Observations.* Solar Physics, 2010. **263**(1): p. 3.
33. Frank, H., *Electromagnetic spectrum*. 2019: Wikimedia commons. p. https://commons.wikimedia.org/wiki/File:Electromagnetic_spectrum_.
34. Bryant, F., *Snell's Law of Refraction.* Physics Bulletin, 1958. **9**(12): p. 317.
35. Joyce, W.B. and A. Joyce, *Descartes, Newton, and Snell's law.* Journal of the Optical Society of America, 1976. **66**(1): p. 1.
36. Brewster, D., *On the Laws Which Regulate the Polarisation of Light by Reflexion from Transparent Bodies.* Philosophical Transactions of the Royal Society of London Series I, 1815. **105**: p. 125.
37. Abdullah, M.F., M.A. Alghoul, H. Naser, N. Asim, S. Ahmadi, B. Yatim, and K. Sopian, *Research and development efforts on texturization to reduce the optical losses at front surface of silicon solar cell.* Renewable and Sustainable Energy Reviews, 2016. **66**: p. 380.
38. *https://www.pveducation.org/pvcdrom/pn-junctions/absorption-coefficient*. 15.03.2020].
39. Atkins, P. and J. de Paula, *Quantum chemistry: atomic structure*, in *Elements of Physical Chemistry*. 2009, Oxford University Press: Oxford, United Kingdom p. 314.
40. Hyde, K.E., *Methods for obtaining Russell-Saunders term symbols from electronic configurations.* Journal of Chemical Education, 1975. **52**(2): p. 87.
41. *SPHERICAL HARMONICS*, in *Quantum Theory of Angular Momentum*. p. 130.
42. Stark, J., *Observation of the Separation of Spectral Lines by an Electric Field.* Nature, 1913. **92**(2301): p. 401.
43. Werts, M.H.V., *Making sense of lanthanide luminescence.* Science Progress, 2005. **88**(2): p. 101.
44. Berthomieu, C. and R. Hienerwadel, *Fourier transform infrared (FTIR) spectroscopy.* Photosynthesis research, 2009. **101**(2-3): p. 157.
45. Long, D.A., *Raman spectroscopy.* New York, 1977: p. 1.

46. Sannigrahi, A., *Derivation of selection rules for magnetic dipole transitions.* Journal of Chemical Education, 1982. **59**(10): p. 819.
47. Laporte, O. and W.F. Meggers, *Some rules of spectral structure.* JOSA, 1925. **11**(5): p. 459.
48. Jahn, H.A. and E. Teller, *Stability of polyatomic molecules in degenerate electronic states-I—Orbital degeneracy.* Proceedings of the Royal Society of London. Series A-Mathematical and Physical Sciences, 1937. **161**(905): p. 220.
49. Chandrasekhar, B. and W.B. White, *Luminescence of single crystal CaMoO4.* Materials research bulletin, 1990. **25**(12): p. 1513.
50. Yang, P., G.-Q. Yao, and J.-H. Lin, *Photoluminescence and combustion synthesis of CaMoO4 doped with Pb2+*. Inorganic Chemistry Communications, 2004. **7**(3): p. 389.
51. Dieke, G.H., H.M. Crosswhite, and H. Crosswhite, *Spectra and energy levels of rare earth ions in crystals.* 1968.
52. Bünzli, J.-C.G., A.-S. Chauvin, H.K. Kim, E. Deiters, and S.V. Eliseeva, *Lanthanide luminescence efficiency in eight-and nine-coordinate complexes: Role of the radiative lifetime.* Coordination Chemistry Reviews, 2010. **254**(21-22): p. 2623.
53. Mitschke, U. and P. Bäuerle, *The electroluminescence of organic materials.* Journal of Materials Chemistry, 2000. **10**(7): p. 1471.
54. Chandra, B., *Mechanoluminescence*, in *Luminescence of solids*. 1998, Springer. p. 361.
55. Zhuravlev, A. and M. Asonov, *Sensitivity and functional characteristics of modern chemoluminescence meters.* Biofizika, 1991. **36**(3): p. 489.
56. Li, S., S.-C. Tan, C.K. Lee, E. Waffenschmidt, S. Hui, and K.T. Chi, *A survey, classification, and critical review of light-emitting diode drivers.* IEEE Transactions on Power Electronics, 2015. **31**(2): p. 1503.
57. Bedyal, A., V. Kumar, O. Ntwaeaborwa, and H. Swart, *A promising orange-red emitting nanocrystalline NaCaBO3: Sm3+ phosphor for solid state lightning.* Materials Research Express, 2014. **1**(1): p. 015006.
58. Ono, Y.A., *Electroluminescent displays*. Vol. 1. 1995: World Scientific.
59. Puurunen, R.L., *A Short History of Atomic Layer Deposition: Tuomo Suntola's Atomic Layer Epitaxy.* Chemical Vapor Deposition, 2014. **20**(10-11-12): p. 332.
60. Rack, P.D., A. Naman, P.H. Holloway, S.S. Sun, and R.T. Tuenge, *Materials Used in Electroluminescent Displays.* MRS Bulletin, 1996. **21**(3): p. 49.
61. Tian, Y., *Development of phosphors with high thermal stability and efficiency for phosphor-converted LEDs.* Journal of Solid State Lighting, 2014. **1**(1): p. 11.
62. Judd, B.R., *Optical absorption intensities of rare-earth ions.* Physical Review, 1962. **127**(3): p. 750.
63. Ofelt, G.S., *Intensities of Crystal Spectra of Rare-Earth Ions.* The Journal of Chemical Physics, 1962. **37**(3): p. 511.
64. Smentek, L., *Judd—Ofelt theory: past, present and future.* Molecular Physics, 2003. **101**(7): p. 893.
65. Neto, J.M., D. Hewak, and H. Tate, *Application of a modified Judd-Ofelt theory to praseodymium-doped fluoride glasses.* Journal of non-crystalline solids, 1995. **183**(1-2): p. 201.
66. Walsh, B.M., *Judd-Ofelt theory: principles and practices*, in *Advances in spectroscopy for lasers and sensing*. 2006, Springer. p. 403.
67. Forster, T., **ZWISCHENMOLEKULARE ENERGIEWANDERUNG UND FLUORESZENZ.* Annalen Der Physik, 1948. **2**(1-2): p. 55.
68. Dexter, D.L., *A Theory of Sensitized Luminescence in Solids.* The Journal of Chemical Physics, 1953. **21**(5): p. 836.
69. Dexter, D.L. and J.H. Schulman, *Theory of Concentration Quenching in Inorganic Phosphors.* The Journal of Chemical Physics, 1954. **22**(6): p. 1063.
70. Meza, O., E.G. Villabona-Leal, L.A. Diaz-Torres, H. Desirena, J.L. Rodríguez-López, and E. Pérez, *Luminescence Concentration Quenching Mechanism in Gd2O3:Eu3+*. The Journal of Physical Chemistry A, 2014. **118**(8): p. 1390.
71. van Sark, W.G., J. de Wild, J.K. Rath, A. Meijerink, and R.E.I. Schropp, *Upconversion in solar cells.* Nanoscale Research Letters, 2013. **8**(1): p. 81.

72. van Sark, W.G.J.H.M., *Simulating performance of solar cells with spectral downshifting layers.* Thin Solid Films, 2008. **516**(20): p. 6808.
73. van Sark, W.G.J.H.M., A. Meijerink, R.E.I. Schropp, J.A.M. van Roosmalen, and E.H. Lysen, *Enhancing solar cell efficiency by using spectral converters.* Solar Energy Materials and Solar Cells, 2005. **87**(1): p. 395.
74. Piper, W.W., J.A. DeLuca, and F.S. Ham, *Cascade fluorescent decay in Pr3+-doped fluorides: Achievement of a quantum yield greater than unity for emission of visible light.* Journal of Luminescence, 1974. **8**(4): p. 344.
75. Sani, E., A. Brugioni, L. Mercatelli, D. Parisi, E.V. Zharikov, D.A. Lis, and K.A. Subbotin, *Yb-doped double tungstates for down-conversion applications.* Optical Materials, 2019. **94**: p. 415.
76. Li, L., X. Zhou, X. Wei, C.-G. Ma, and M.G. Brik, *Enhanced near-infrared quantum cutting in CaMoO4:Yb3+ phosphors induced by doping with Li+ ions for improving solar cells efficiency.* Materials Chemistry and Physics, 2014. **147**(3): p. 860.
77. Cao, X., L. Li, X. Wei, Y. Chen, W. Zhang, and M. Yin, *CaMoO4: x% Yb3+: A novel near-infrared quantum-cutting phosphors via cooperative energy transfer.* Journal of nanoscience and nanotechnology, 2011. **11**(11): p. 9543.
78. Eilers, J.J., D. Biner, J.T.v. Wijngaarden, K. Krämer, H.-U. Güdel, and A. Meijerink, *Efficient visible to infrared quantum cutting through downconversion with the Er3+–Yb3+ couple in Cs3Y2Br9.* Applied Physics Letters, 2010. **96**(15): p. 151106.
79. Aarts, L., B.M.v.d. Ende, and A. Meijerink, *Downconversion for solar cells in NaYF4:Er,Yb.* Journal of Applied Physics, 2009. **106**(2): p. 023522.
80. Aarts, L., B.v.d. Ende, M.F. Reid, and A. Meijerink, *Downconversion for Solar Cells in YF3:Pr3+, Yb3+.* Spectroscopy Letters, 2010. **43**(5): p. 373.
81. Das, S. and K.C. Mandal, *Optical downconversion in rare earth (Tb3+ and Yb3+) doped CdS nanocrystals.* Materials Letters, 2012. **66**(1): p. 46.
82. Dumont, L., J. Cardin, P. Benzo, M. Carrada, C. Labbé, A.L. Richard, D.C. Ingram, W.M. Jadwisienczak, and F. Gourbilleau, *SiNx:Tb3+–Yb3+, an efficient down-conversion layer compatible with a silicon solar cell process.* Solar Energy Materials and Solar Cells, 2016. **145**: p. 84.
83. Florêncio, L.d.A., L.A. Gómez-Malagón, B.C. Lima, A.S.L. Gomes, J.A.M. Garcia, and L.R.P. Kassab, *Efficiency enhancement in solar cells using photon down-conversion in Tb/Yb-doped tellurite glass.* Solar Energy Materials and Solar Cells, 2016. **157**: p. 468.
84. Huang, X.Y. and Q.Y. Zhang, *Efficient near-infrared down conversion in Zn2SiO4:Tb3+,Yb3+ thin-films.* Journal of Applied Physics, 2009. **105**(5): p. 053521.
85. Yuan, J.-L., X.-Y. Zeng, J.-T. Zhao, Z.-J. Zhang, H.-H. Chen, and X.-X. Yang, *Energy transfer mechanisms in Tb3+, Yb3+codoped Y2O3downconversion phosphor.* Journal of Physics D: Applied Physics, 2008. **41**(10): p. 105406.
86. Zhang, J., H. Xia, Y. Jiang, S. Yang, H. Jiang, and B. Chen, *Efficient Quantum Cutting in Tb3+/Yb3+ Codoped $\alpha $ -NaYF4 Single Crystals Grown by Bridgman Method Using KF Flux for Solar Photovoltaic.* IEEE Journal of Quantum Electronics, 2015. **51**(6): p. 1.
87. Chen, D., Y. Yu, H. Lin, P. Huang, Z. Shan, and Y. Wang, *Ultraviolet-blue to near-infrared downconversion of Nd3+-Yb3+ couple.* Optics Letters, 2010. **35**(2): p. 220.
88. Liu, X., Y. Qiao, G. Dong, S. Ye, B. Zhu, G. Lakshminarayana, D. Chen, and J. Qiu, *Cooperative downconversion in Yb3+–RE3+ (RE=Tm or Pr) codoped lanthanum borogermanate glasses.* Optics Letters, 2008. **33**(23): p. 2858.
89. Xie, L., Y. Wang, and H. Zhang, *Near-infrared quantum cutting in YPO 4: Yb 3+, Tm 3+ via cooperative energy transfer.* Applied Physics Letters, 2009. **94**(6): p. 061905.
90. Zhou, J., Y. Zhuang, S. Ye, Y. Teng, G. Lin, B. Zhu, J. Xie, and J. Qiu, *Broadband downconversion based infrared quantum cutting by cooperative energy transfer from Eu 2+ to Yb 3+ in glasses.* Applied Physics Letters, 2009. **95**(14): p. 141101.
91. Gao, G. and L. Wondraczek, *Near-infrared down-conversion in Mn 2+–Yb 3+ co-doped Zn 2 GeO 4.* Journal of Materials Chemistry C, 2013. **1**(10): p. 1952.

92. Deng, K., T. Gong, L. Hu, X. Wei, Y. Chen, and M. Yin, *Efficient near-infrared quantum cutting in NaYF 4: Ho 3+, Yb 3+ for solar photovoltaics.* Optics express, 2011. **19**(3): p. 1749.
93. Yu, D.C., F.T. Rabouw, W.Q. Boon, T. Kieboom, S. Ye, Q.Y. Zhang, and A. Meijerink, *Insights into the energy transfer mechanism in ${\mathrm{Ce}}^{3+}\ensuremath{-}{\mathrm{Yb}}^{3+}$ codoped YAG phosphors.* Physical Review B, 2014. **90**(16): p. 165126.
94. Chen, D., Y. Wang, Y. Yu, P. Huang, and F. Weng, *Quantum cutting downconversion by cooperative energy transfer from Ce3+ to Yb3+ in borate glasses.* Journal of Applied Physics, 2008. **104**(11): p. 116105.
95. Zhydachevskyy, Y., I.I. Syvorotka, V. Tsiumra, M. Baran, L. Lipińska, A. Wierzbicka, and A. Suchocki, *Quantum efficiency of the down-conversion process in Bi3+–Yb3+ and Ce3+–Yb3+ co-doped garnets.* Solar Energy Materials and Solar Cells, 2018. **185**: p. 240.
96. de la Mora, M.B., O. Amelines-Sarria, B.M. Monroy, C.D. Hernández-Pérez, and J.E. Lugo, *Materials for downconversion in solar cells: Perspectives and challenges.* Solar Energy Materials and Solar Cells, 2017. **165**: p. 59.
97. Getz, M.N., P.-A. Hansen, Ø.S. Fjellvåg, M.A. Ahmed, H. Fjellvåg, and O. Nilsen, *Intense NIR emission in YVO 4: Yb 3+ thin films by atomic layer deposition.* Journal of Materials Chemistry C, 2017. **5**(33): p. 8572.
98. Getz, M., P.-A. Hansen, M.A.K. Ahmed, H. Fjellvåg, and O. Nilsen, *Luminescent YbVO4 by atomic layer deposition.* Dalton Transactions, 2017. **46**(9): p. 3008.
99. Li, Y., X. Wei, H. Chen, Y. Pan, and Y. Ji, *Near-infrared downconversion through host sensitized energy transfer in Yb3+-doped Na2YMg2 (VO4) 3.* Physica B: Condensed Matter, 2015. **478**: p. 95.
100. Zhydachevskyy, Y., V. Tsiumra, M. Baran, L. Lipińska, P. Sybilski, and A. Suchocki, *Quantum efficiency of the down-conversion process in Bi3+–Yb3+ co-doped Gd2O3.* Journal of Luminescence, 2018. **196**: p. 169.
101. Huang, X., J. Wang, D. Yu, S. Ye, Q. Zhang, and X. Sun, *Spectral conversion for solar cell efficiency enhancement using YVO4: Bi3+, Ln3+ (Ln= Dy, Er, Ho, Eu, Sm, and Yb) phosphors.* Journal of Applied Physics, 2011. **109**(11): p. 113526.
102. Wang, Z. and A. Meijerink, *Dye-Sensitized Downconversion.* The Journal of Physical Chemistry Letters, 2018. **9**(7): p. 1522.
103. Liu, J., A.M. Kaczmarek, F. Artizzu, and R. Van Deun, *Ultraefficient Cascade Energy Transfer in Dye-Sensitized Core/Shell Fluoride Nanoparticles.* ACS Photonics, 2019. **6**(3): p. 659.
104. Shao, W., C.-K. Lim, Q. Li, M.T. Swihart, and P.N. Prasad, *Dramatic Enhancement of Quantum Cutting in Lanthanide-Doped Nanocrystals Photosensitized with an Aggregation-Induced Enhanced Emission Dye.* Nano Letters, 2018. **18**(8): p. 4922.
105. Hansen, P.-A., T. Zikmund, T. Yu, J.N. Kvalvik, T. Aarholt, Ø. Prytz, A. Meijerink, and O. Nilsen, *Single-step approach to sensitized luminescence through bulk-embedded organics in crystalline fluorides.* Communications Chemistry, 2020. **3**(1): p. 162.
106. van Wijngaarden, J.T., S. Scheidelaar, T.J.H. Vlugt, M.F. Reid, and A. Meijerink, *Energy transfer mechanism for downconversion in the (${\text{Pr}}^{3+}$, ${\text{Yb}}^{3+}$) couple.* Physical Review B, 2010. **81**(15): p. 155112.
107. Boutinaud, P., R. Mahiou, E. Cavalli, and M. Bettinelli, *Excited state dynamics of Pr3+ in YVO4 crystals.* Journal of Applied Physics, 2004. **96**(9): p. 4923.
108. Boutinaud, P., R. Mahiou, E. Cavalli, and M. Bettinelli, *Luminescence properties of Pr3+ in titanates and vanadates: Towards a criterion to predict 3P0 emission quenching.* Chemical Physics Letters, 2006. **418**(1): p. 185.
109. Boutinaud, P., R. Mahiou, E. Cavalli, and M. Bettinelli, *Red luminescence induced by intervalence charge transfer in Pr3+-doped compounds.* Journal of Luminescence, 2007. **122-123**: p. 430.
110. Boutinaud, P., E. Pinel, M. Dubois, A.P. Vink, and R. Mahiou, *UV-to-red relaxation pathways in CaTiO3:Pr3+*. Journal of Luminescence, 2005. **111**(1): p. 69.

111. Boutinaud, P., E. Pinel, M. Oubaha, R. Mahiou, E. Cavalli, and M. Bettinelli, *Making red emitting phosphors with Pr3+*. Optical Materials, 2006. **28**(1): p. 9.
112. Cavalli, E., F. Angiuli, P. Boutinaud, and R. Mahiou, *Optical spectroscopy and excited state dynamics of CaMoO4:Pr3+*. Journal of Solid State Chemistry, 2012. **185**: p. 136.
113. Cavalli, E., P. Boutinaud, and M. Grinberg, *Luminescence dynamics in CaWO4:Pr3+ powders and single crystals.* Journal of Luminescence, 2016. **169**: p. 450.
114. Komar, J., R. Lisiecki, R. Kowalski, B. Macalik, P. Solarz, M. Głowacki, M. Berkowski, and W. Ryba-Romanowski, *Down- and Upconversion Phenomena in Gd3(Al,Ga)5O12 Crystals Doped with Pr3+ and Yb3+ Ions.* The Journal of Physical Chemistry C, 2018. **122**(24): p. 13061.
115. Kasha, M., *Fifty years of the Jabłoński diagram.* Acta Phys. Polon. A, 1987. **71**: p. 661.
116. Sveshnikova, G.V., S.I. Kol'tsov, and V.B. Aleskovskii, *Fabrication of a layer silicon dioxide of a given thickness on the surface of silicon by molecular lamination.* Zhurnal Prikladnoi Khimii, 1970. **45**(5): p. 1150.
117. Suntola, T. and J. Antson, *FIN 52359 US 4 058 430* 1974: International patent.
118. Tanninen, V.P., M. Oikkonen, and T. Tuomi, *Comparative study of the crystal phase, crystallite size and microstrain in electroluminescent ZnS:Mn films grown by atomic layer epitaxy and electron beam evaporation.* Thin Solid Films, 1983. **109**(3): p. 283.
119. Kong, W., J. Fogarty, and R. Solanki, *Atomic layer epitaxy of ZnS:Tb thin film electroluminescent devices.* Applied Physics Letters, 1994. **65**(6): p. 670.
120. Kong, W., J. Fogarty, R. Solanki, and R.T. Tuenge, *White light emitting SrS:Pr electroluminescent devices fabricated via atomic layer epitaxy.* Applied Physics Letters, 1995. **66**(4): p. 419.
121. Miikkulainen, V., M. Leskelä, M. Ritala, and R.L. Puurunen, *Crystallinity of inorganic films grown by atomic layer deposition: Overview and general trends.* Journal of Applied Physics, 2013. **113**(2): p. 021301.
122. Vee, I., *Fluorholdige hybridmaterialer med atomlagsavsetting: Syntese og karakterisering.* . 2012, University of Oslo.
123. George, S.M., *Atomic Layer Deposition: An Overview.* Chemical Reviews, 2010. **110**(1): p. 111.
124. Delft, J., D. Garcia-Alonso, and W.M.M. Kessels, *Atomic layer deposition for photovoltaics: Applications and prospects for solar cell manufacturing.* Semiconductor Science and Technology, 2012. **27**: p. 074002.
125. Jiang, X., H. Huang, F.B. Prinz, and S.F. Bent, *Application of atomic layer deposite of platinum to solid oxide fuel cells.* Chemistry of Materials, 2008. **20**(12): p. 3897.
126. Gusev, E.P., C. Cabral, M. Copel, C. D'Emic, and M. Gribelyuk, *Ultrathin HfO2 films grown on silicon by atomic layer deposition for advanced gate dielectrics applications.* Microelectronic Engineering, 2003. **69**(2): p. 145.
127. Lausund, K.B. and O. Nilsen, *All-gas-phase synthesis of UiO-66 through modulated atomic layer deposition.* Nature communications, 2016. **7**(1): p. 1.
128. Bratvold, J.E., H. Fjellvåg, and O. Nilsen, *Phase and Orientation Control of NiTiO3 Thin Films.* Materials, 2020. **13**(1): p. 112.
129. Hansen, P.-A., H. Fjellvåg, T.G. Finstad, and O. Nilsen, *Luminescent Properties of Multilayered Eu2O3 and TiO2 Grown by Atomic Layer Deposition***.* Chemical Vapor Deposition, 2014. **20**(7-8-9): p. 274.
130. Fair, R.B., *Rapid thermal processing: science and technology*. 2012: Academic Press.
131. Chen, R., H. Kim, P.C. McIntyre, D.W. Porter, and S.F. Bent, *Achieving area-selective atomic layer deposition on patterned substrates by selective surface modification.* Applied Physics Letters, 2005. **86**(19): p. 191910.
132. Gladfelter, W.L., *Selective metalization by chemical vapor deposition.* Chemistry of Materials, 1993. **5**(10): p. 1372.
133. Wu, B. and A. Kumar, *Extreme ultraviolet lithography: A review.* J. Vac. Sci. Technol. B, 2007. **25**(6): p. 1743.

134. Clark, R., K. Tapily, K.-H. Yu, T. Hakamata, S. Consiglio, D. O'Meara, C. Wajda, J. Smith, and G. Leusink, *Perspective: New process technologies required for future devices and scaling.* APL Materials, 2018. **6**(5): p. 058203.
135. Choi, J.Y., C.F. Ahles, R. Hung, N. Kim, and A.C. Kummel, *Selective atomic layer deposition of MoSix on Si (0 0 1) in preference to silicon nitride and silicon oxide.* Applied Surface Science, 2018. **462**: p. 1008.
136. Mameli, A., Y. Kuang, M. Aghaee, C.K. Ande, B. Karasulu, M. Creatore, A.J.M. Mackus, W.M.M. Kessels, and F. Roozeboom, *Area-Selective Atomic Layer Deposition of In2O3:H Using a μ-Plasma Printer for Local Area Activation.* Chemistry of Materials, 2017. **29**(3): p. 921.
137. Mameli, A., B. Karasulu, M.A. Verheijen, B. Barcones, B. Macco, A.J.M. Mackus, W.M.M.E. Kessels, and F. Roozeboom, *Area-Selective Atomic Layer Deposition of ZnO by Area Activation Using Electron Beam-Induced Deposition.* Chemistry of Materials, 2019. **31**(4): p. 1250.
138. Singh, J.A., N.F.W. Thissen, W.-H. Kim, H. Johnson, W.M.M. Kessels, A.A. Bol, S.F. Bent, and A.J.M. Mackus, *Area-Selective Atomic Layer Deposition of Metal Oxides on Noble Metals through Catalytic Oxygen Activation.* Chemistry of Materials, 2018. **30**(3): p. 663.
139. Patwardhan, S., D.H. Cao, G.C. Schatz, and A.B.F. Martinson, *Atomic Layer Deposition Nucleation on Isolated Self-Assembled Monolayer Functional Groups: A Combined DFT and Experimental Study.* ACS Applied Energy Materials, 2019. **2**(7): p. 4618.
140. Bobb-Semple, D., K.L. Nardi, N. Draeger, D.M. Hausmann, and S.F. Bent, *Area-Selective Atomic Layer Deposition Assisted by Self-Assembled Monolayers: A Comparison of Cu, Co, W, and Ru.* Chemistry of Materials, 2019. **31**(5): p. 1635.
141. Petro, D., H. Ali, E. Hamit, K. Talha Masood, and B. Necmi, *Area-Selective Atomic Layer Deposition of Noble Metals: Polymerized Fluorocarbon Layers as Effective Growth Inhibitors*. 2019.
142. Zhang, Z., T. Dwyer, S.M. Sirard, and J.G. Ekerdt, *Area-selective atomic layer deposition of cobalt oxide to generate patterned cobalt films.* J. Vac. Sci. Technol. A, 2019. **37**(2): p. 020905.
143. Mackus, A.J.M., A.A. Bol, and W.M.M. Kessels, *The use of atomic layer deposition in advanced nanopatterning.* Nanoscale, 2014. **6**(19): p. 10941.
144. Parsons, G.N., *Functional model for analysis of ALD nucleation and quantification of area-selective deposition.* J. Vac. Sci. Technol. A, 2019. **37**(2): p. 020911.
145. Avrami, M., *Kinetics of Phase Change. II Transformation-Time Relations for Random Distribution of Nuclei.* The Journal of Chemical Physics, 1940. **8**(2): p. 212.
146. Nilsen, O., C.E. Mohn, A. Kjekshus, and H. Fjellvåg, *Analytical model for island growth in atomic layer deposition using geometrical principles.* Journal of Applied Physics, 2007. **102**(2): p. 024906.
147. Suntola, T., *Atomic layer epitaxy.* Thin Solid Films, 1992. **216**(1): p. 84.
148. Klepper, K.B., O. Nilsen, and H. Fjellvåg, *Epitaxial growth of cobalt oxide by atomic layer deposition.* Journal of Crystal Growth, 2007. **307**(2): p. 457.
149. Mackus, A.J.M., J.R. Schneider, C. MacIsaac, J.G. Baker, and S.F. Bent, *Synthesis of Doped, Ternary, and Quaternary Materials by Atomic Layer Deposition: A Review.* Chemistry of Materials, 2019. **31**(4): p. 1142.
150. Lakomaa, E.L., S. Haukka, and T. Suntola, *Atomic layer growth of TiO2 on silica.* Applied Surface Science, 1992. **60-61**: p. 742.
151. Nilsen, O., M. Lie, H.F. Fjellvåg, and A. Kjekshus, *Growth of Oxides with Complex Stoichiometry by the ALD Technique, Exemplified by Growth of La1–xCaxMnO3*, in *Rare Earth Oxide Thin Films*, M. Fanciulli and G. Scarel, Editors. 2007, Springer Berlin Heidelberg: Berlin, Germany. p. 87.
152. King, D.M., S.I. Johnson, J. Li, X. Du, X. Liang, and A.W. Weime, *Atomic layer deposition of quantum-confined ZnO nanostructures.* Nanotechnology, 2009(20): p. 195401.
153. King, D.M., X. Du, A.S. Cavanagh, and A.W. Weimer, *Quantum confinement in amorphous TiO2 films studied via atomic layer deposition.* Nanotechnology, 2008(19): p. 445401.

154. Czitrom, V., *One-Factor-at-a-Time versus Designed Experiments.* The American Statistician, 1999. **53**(2): p. 126.
155. Yates, F., *Sir Ronald Fisher and the Design of Experiments.* Biometrics, 1964. **20**(2): p. 307.
156. Skipper, R.A., *SIR RONALD AYLMER FISHER*, in *Philosophy of Biology*, M. Matthen and C. Stephens, Editors. 2007, North-Holland: Amsterdam. p. 37.
157. Efron, B., *R. A. Fisher in the 21st century (Invited paper presented at the 1996 R. A. Fisher Lecture).* Statist. Sci., 1998. **13**(2): p. 95.
158. Plackett, R.L. and J.P. Burman, *THE DESIGN OF OPTIMUM MULTIFACTORIAL EXPERIMENTS.* Biometrika, 1946. **33**(4): p. 305.
159. Kiani, M., M. Yousefi, M. Rashidzadeh, A. Irandoukht, and F. Salehirad, *Influence of synthesis parameters on the properties of nanostructured γ-Alumina using plackett-burman experimental design.* International Journal of Nano Dimension, 2018. **9**(4): p. 386.
160. Anubhav, A., S. Gyanendra, and A.S. Shubhini, *PLACKETT-BURMAN DESIGN AS A TOOL FOR SCREENING AND PROCESS OPTIMIZATION OF RIVASTIGMINE-LOADED LIPID NANOCARRIERS.* Asian Journal of Pharmaceutical and Clinical Research, 2018. **11**(12).
161. Heydari, S., L. Zare, and H. Ghiassi, *Plackett–Burman experimental design for the removal of diazinon pesticide from aqueous system by magnetic bentonite nanocomposites.* Journal of Applied Research in Water and Wastewater, 2019. **6**(1): p. 45.
162. Box, G.E.P. and K.B. Wilson, *On the experimental attainement of optimum conditions.* Journal of the Royal Statistical Society, Series B, 1951. **13**: p. 1.
163. Box, G.E.P. and N.R. Draper, *Response Surfaces, Mixtures, and Ridge Analyses*. Second ed. ed. 2007: Wiley.
164. Melville, W.H., *Powellite; calcium molybdate; a new mineral species.* American Journal of Science, 1891. **Series 3 Vol. 41**(242): p. 138.
165. Spassky, D., S. Ivanov, I. Kitaeva, V. Kolobanov, V. Mikhailin, L. Ivleva, and I. Voronina, *Optical and luminescent properties of a series of molybdate single crystals of scheelite crystal structure.* physica status solidi (c), 2005. **2**(1): p. 65.
166. Groenink, J.A., C. Hakfoort, and G. Blasse, *The Luminescence of Calcium Molybdate.* physica status solidi (a), 1979. **54**(1): p. 329.
167. Zakharko, Y., A. Luchechko, I. Syvorotka, G. Stryganyuk, and I. Solskii, *Anisotropy of optical absorption and luminescent properties of CaMoO4.* Radiation Measurements, 2010. **45**(3): p. 429.
168. Anicete-Santos, M., F.C. Picon, M.T. Escote, E.R. Leite, P.S. Pizani, J.A. Varela, and E. Longo, *Room-temperature photoluminescence in structurally disordered SrWO4.* Applied Physics Letters, 2006. **88**(21): p. 211913.
169. Xiao, B. and M. Schmidt, *Incorporation of Europium(III) into Scheelite-Related Host Matrixes ABO4 (A = Ca2+, Sr2+, Ba2+; B = W6+, Mo6+): Role of A and B Sites on the Dopant Site Distribution and Photoluminescence.* Inorganic Chemistry, 2017. **56**(24): p. 14948.
170. Arakcheeva, A., P. Pattison, G. Chapuis, M. Rossell, A. Filaretov, V. Morozov, and G. Van Tendeloo, *KSm (MoO4) 2, an incommensurately modulated and partially disordered scheelite-like structure.* Acta Crystallographica Section B: Structural Science, 2008. **64**(2): p. 160.
171. Martinez-Garcia, J., A. Arakcheeva, P. Pattison, V. Morozov, and G. Chapuis, *Validating the model of a (3 + 1)-dimensional incommensurately modulated structure as generator of a family of compounds for the Eu2(MoO4)3 scheelite structure.* Philosophical Magazine Letters, 2009. **89**(4): p. 257.
172. Morozov, V., A. Arakcheeva, B. Redkin, V. Sinitsyn, S. Khasanov, E. Kudrenko, M. Raskina, O. Lebedev, and G. Van Tendeloo, *Na2/7Gd4/7MoO4: a Modulated Scheelite-Type Structure and Conductivity Properties.* Inorganic Chemistry, 2012. **51**(9): p. 5313.
173. Morozov, V.A., A.V. Arakcheeva, G. Chapuis, N. Guiblin, M.D. Rossell, and G. Van Tendeloo, *KNd(MoO4)2: A New Incommensurate Modulated Structure in the Scheelite Family.* Chemistry of Materials, 2006. **18**(17): p. 4075.
174. Jiang, P., W. Gao, R. Cong, and T. Yang, *Structural investigation of the A-site vacancy in scheelites and the luminescence behavior of two continuous solid solutions A 1–1.5 x Eu x□*

0.5 x WO 4 and A 0.64–0.5 y Eu 0.24 Li y□ 0.12–0.5 y WO 4 (A= Ca, Sr;□= vacancy). Dalton Transactions, 2015. **44**(13): p. 6175.
175. Logvinovich, D., A. Arakcheeva, P. Pattison, S. Eliseeva, P. Tomeš, I. Marozau, and G. Chapuis, *Crystal Structure and Optical and Magnetic Properties of Pr2(MoO4)3.* Inorganic Chemistry, 2010. **49**(4): p. 1587.
176. Ansari, A.A., A.K. Parchur, M. Alam, J. Labis, and A. Azzeer, *Influence of Surface Coating on Structural and Photoluminescent Properties of CaMoO4:Pr Nanoparticles.* Journal of Fluorescence, 2014. **24**(4): p. 1253.
177. Cavalli, E., P. Boutinaud, R. Mahiou, M. Bettinelli, and P. Dorenbos, *Luminescence Dynamics in Tb3+-Doped CaWO4 and CaMoO4 Crystals.* Inorganic Chemistry, 2010. **49**(11): p. 4916.
178. Gupta, S.K., M. Sahu, P.S. Ghosh, D. Tyagi, M.K. Saxena, and R.M. Kadam, *Energy transfer dynamics and luminescence properties of Eu3+ in CaMoO4 and SrMoO4.* Dalton Transactions, 2015. **44**(43): p. 18957.
179. Cho, K., J. Choi, J.-I. Lee, and J.H. Ryu, *Pulsed-laser-assisted synthesis of a Tm3+/Yb3+ co-doped CaMoO4 colloidal nanocrystal and its upconversion luminescence.* Journal of the Korean Physical Society, 2016. **68**(1): p. 22.
180. Sun, J., D. Cui, G. Sun, B. Xue, and C. Cao, *Near-infrared luminescence and energy transfer in CaMoO4: Ho3+, Yb3+ phosphor.* Journal of Materials Science, 2014. **49**(2): p. 527.
181. Gao, D., Y. Li, X. Lai, Y. Wei, J. Bi, Y. Li, and M. Liu, *Fabrication and luminescence properties of Dy3+ doped CaMoO4 powders.* Materials Chemistry and Physics, 2011. **126**(1): p. 391.
182. Singh, B., A. Parchur, R. Ningthoujam, A. Ansari, P. Singh, and S. Rai, *Enhanced photoluminescence in CaMoO 4: Eu 3+ by Gd 3+ co-doping.* Dalton transactions, 2014. **43**(12): p. 4779.
183. Sinha, S., M.K. Mahata, K. Kumar, S.P. Tiwari, and V.K. Rai, *Dualistic temperature sensing in Er3+/Yb3+ doped CaMoO4 upconversion phosphor.* Spectrochimica Acta Part A: Molecular and Biomolecular Spectroscopy, 2017. **173**: p. 369.
184. Zolotova, E.S., L.N. Trushnikova, B.M. Ayupov, V.V. Sokolov, and V.A. Daletskii, *Na2MoO4-CaMoO4-Ce2/3MoO4 scheelite-like solid solutions.* Inorganic Materials, 2009. **45**(4): p. 432.
185. Verma, A. and S.K. Sharma, *Down-conversion from Er3+-Yb3+ codoped CaMoO4 phosphor: A spectral conversion to improve solar cell efficiency.* Ceramics International, 2017. **43**(12): p. 8879.
186. Huang, F., Y. Gao, J. Zhou, J. Xu, and Y. Wang, *Yb3+/Er3+ co-doped CaMoO4: a promising green upconversion phosphor for optical temperature sensing.* Journal of Alloys and Compounds, 2015. **639**: p. 325.
187. Duncan, R.C., *Continuous Room-Temperature Nd3+: CaMoO4 Laser.* Journal of Applied Physics, 1965. **36**(3): p. 874.
188. Xi, H.H., D. Zhou, H.D. Xie, B. He, and Q.P. Wang, *Raman Spectra, Infrared Spectra, and Microwave Dielectric Properties of Low-Temperature Firing [(Li0. 5Ln0. 5) 1− xCax] MoO4 (Ln= Sm and Nd) Solid Solution Ceramics with Scheelite Structure.* Journal of the American Ceramic Society, 2015. **98**(2): p. 587.
189. Hazra, C., T. Samanta, A.V. Asaithambi, and V. Mahalingam, *Bilayer stabilized Ln 3+-doped CaMoO 4 nanocrystals with high luminescence quantum efficiency and photocatalytic properties.* Dalton Transactions, 2014. **43**(18): p. 6623.
190. Wu, H., Y. Hu, W. Zhang, F. Kang, N. Li, and G. Ju, *Sol–gel synthesis of Eu3+ incorporated CaMoO4: the enhanced luminescence performance.* Journal of Sol-Gel Science and Technology, 2012. **62**(2): p. 227.
191. Li, X., Z. Yang, L. Guan, J. Guo, Y. Wang, and Q. Guo, *Synthesis and luminescent properties of CaMoO4:Tb3+, R+ (Li+, Na+, K+).* Journal of Alloys and Compounds, 2009. **478**(1): p. 684.
192. Vidya, S., S. Solomon, and J.K. Thomas, *Synthesis, sintering and optical properties of CaMoO4: A promising scheelite LTCC and photoluminescent material.* physica status solidi (a), 2012. **209**(6): p. 1067.

193. Thongtem, T., S. Kungwankunakorn, B. Kuntalue, A. Phuruangrat, and S. Thongtem, *Luminescence and absorbance of highly crystalline CaMoO4, SrMoO4, CaWO4 and SrWO4 nanoparticles synthesized by co-precipitation method at room temperature.* Journal of Alloys and Compounds, 2010. **506**(1): p. 475.
194. Hosseinpour-Mashkani, S.S., S.S. Hosseinpour-Mashkani, and A. Sobhani-Nasab, *Synthesis and characterization of rod-like CaMoO4 nanostructure via free surfactant sonochemical route and its photocatalytic application.* Journal of Materials Science: Materials in Electronics, 2016. **27**(5): p. 4351.
195. Grasser, R., E. Pitt, A. Scharmann, and G. Zimmerer, *Optical properties of CaWO4 and CaMoO4 crystals in the 4 to 25 eV region.* physica status solidi (b), 1975. **69**(2): p. 359.
196. Wang, Y., J. Ma, J. Tao, X. Zhu, J. Zhou, Z. Zhao, L. Xie, and H. Tian, *Low temperature synthesis of CaMoO4 nanoparticles.* Ceramics International, 2007. **33**(4): p. 693.
197. Yin, Y., Y. Gao, Y. Sun, B. Zhou, L. Ma, X. Wu, and X. Zhang, *Synthesis and photoluminescent properties of CaMoO4 nanostructures at room temperature.* Materials Letters, 2010. **64**(5): p. 602.
198. Ju, X., X. Li, Y. Yang, W. Li, C. Tao, and W. Feng, *Luminescence properties of core-shell structured SiO2@ CaMoO4: Eu3+ phosphor.* Journal of Solid State Chemistry, 2012. **187**: p. 109.
199. Parchur, A., A. Prasad, A. Ansari, S. Rai, and R. Ningthoujam, *Luminescence properties of Tb 3+-doped CaMoO 4 nanoparticles: annealing effect, polar medium dispersible, polymer film and core–shell formation.* Dalton Transactions, 2012. **41**(36): p. 11032.
200. Ansari, A.A. and M. Alam, *Optical and structural studies of CaMoO4: Sm, CaMoO4: Sm@ CaMoO4 and CaMoO4: Sm@ CaMoO4@ SiO2 core–shell nanoparticles.* Journal of Luminescence, 2015. **157**: p. 257.
201. Sobiesierski, Z., *Photoluminescence Spectroscopy*, in *Epioptics: Linear and Nonlinear Optical Spectroscopy of Surfaces and Interfaces*, J.F. McGlip, D. Weaire, and C.H. Patterson, Editors. 1995, Springer Berlin Heidelberg: Berlin, Germany. p. 133.
202. Gilliland, G., *Photoluminescence spectroscopy of crystalline semiconductors.* Materials Science and Engineering: R: Reports, 1997. **18**(3-6): p. 99.
203. Jellison, G.E., *Data analysis for spectroscopic ellipsometry.* Thin Solid Films, 1993. **234**(1): p. 416.
204. Bragg, W.H. and W.L. Bragg, *The reflection of X-rays by crystals.* Proceedings of the Royal Society of London. Series A, Containing Papers of a Mathematical and Physical Character, 1913. **88**(605): p. 428.
205. Bunaciu, A.A., E.g. Udriştioiu, and H.Y. Aboul-Enein, *X-Ray Diffraction: Instrumentation and Applications.* Critical Reviews in Analytical Chemistry, 2015. **45**(4): p. 289.
206. Gražulis, S., A. Daškevič, A. Merkys, D. Chateigner, L. Lutterotti, M. Quirós, N.R. Serebryanaya, P. Moeck, R.T. Downs, and A. Le Bail, *Crystallography Open Database (COD): an open-access collection of crystal structures and platform for world-wide collaboration.* Nucleic Acids Res, 2012. **40**(Database issue): p. D420.
207. Warren, B.E., *X-ray Diffraction*. 1990: Courier Corporation.
208. Rietveld, H., *A profile refinement method for nuclear and magnetic structures.* Journal of applied Crystallography, 1969. **2**(2): p. 65.
209. Pawley, G.S., *Unit-cell refinement from powder diffraction scans.* Journal of Applied Crystallography, 1981. **14**(6): p. 357.
210. Goldstein, J.I., D.E. Newbury, J.R. Michael, N.W. Ritchie, J.H.J. Scott, and D.C. Joy, *Scanning electron microscopy and X-ray microanalysis*. 2017, New York, NY, USA: Springer New York.
211. Henderson, B. and G.F. Imbusch, *Optical spectroscopy of inorganic solids*. Vol. 44. 2006: Oxford University Press.
212. Tauc, J., *Optical properties and electronic structure of amorphous Ge and Si.* Materials Research Bulletin, 1968. **3**(1): p. 37.
213. Binnig, G., C.F. Quate, and C. Gerber, *Atomic Force Microscope.* Physical Review Letters, 1986. **56**(9): p. 930.

214. Bellitto, V., *Atomic force microscopy: imaging, measuring and manipulating surfaces at the atomic scale*. 2012: BoD–Books on Demand.
215. Beckhoff, B., B. Kanngießer, N. Langhoff, R. Wedell, and H. Wolff, *Handbook of practical X-ray fluorescence analysis*. 2007: Springer Science & Business Media.
216. Fadley, C.S., *X-ray photoelectron spectroscopy: Progress and perspectives.* Journal of Electron Spectroscopy and Related Phenomena, 2010. **178**: p. 2.
217. Smits, F., *Measurement of sheet resistivities with the four-point probe.* Bell System Technical Journal, 1958. **37**(3): p. 711.
218. Sauerbrey, G., *Verwendung von Schwingquarzen zur Wägung dünner Schichten und zur Mikrowägung.* Zeitschrift für Physik, 1959. **155**(2): p. 206.
219. Diskus, M., O. Nilsen, and H. Fjellvag, *Growth of thin films of molybdenum oxide by atomic layer deposition.* Journal of Materials Chemistry, 2011. **21**(3): p. 705.
220. Nilsen, O., H. Fjellvåg, and A. Kjekshus, *Growth of calcium carbonate by the atomic layer chemical vapour deposition technique.* Thin Solid Films, 2004. **450**(2): p. 240.
221. Hansen, P.-A., H. Fjellvag, T. Finstad, and O. Nilsen, *Structural and optical properties of lanthanide oxides grown by atomic layer deposition (Ln = Pr, Nd, Sm, Eu, Tb, Dy, Ho, Er, Tm, Yb).* Dalton Transactions, 2013. **42**(30): p. 10778.
222. Diskus, M., M. Balasundaram, O. Nilsen, and H. Fjellvåg, *Influence of precursors chemistry on ALD growth of cobalt–molybdenum oxide films.* Dalton Transactions, 2012. **41**(8): p. 2439.
223. Getz, M.N., O. Nilsen, and P.-A. Hansen, *Sensors for optical thermometry based on luminescence from layered YVO4: Ln3+ (Ln = Nd, Sm, Eu, Dy, Ho, Er, Tm, Yb) thin films made by atomic layer deposition.* Scientific Reports, 2019. **9**(1): p. 10247.
224. Sønsteby, H.H., H. Fjellvåg, and O. Nilsen, *Functional Perovskites by Atomic Layer Deposition – An Overview.* Advanced Materials Interfaces, 2017. **4**(8): p. 1600903.
225. Kukli, K., M. Ritala, T. Sajavaara, T. Hänninen, and M. Leskelä, *Atomic layer deposition of calcium oxide and calcium hafnium oxide films using calcium cyclopentadienyl precursor.* Thin Solid Films, 2006. **500**(1): p. 322.
226. Drake, T.L. and P.C. Stair, *Vapor deposition of molybdenum oxide using bis(ethylbenzene) molybdenum and water.* J. Vac. Sci. Technol. A, 2016. **34**(5): p. 051403.
227. Moody, M.J., A. Henning, T. Jurca, J.Y. Shang, H. Bergeron, I. Balla, J.N. Olding, E.A. Weiss, M.C. Hersam, T.L. Lohr, T.J. Marks, and L.J. Lauhon, *Atomic Layer Deposition of Molybdenum Oxides with Tunable Stoichiometry Enables Controllable Doping of MoS2.* Chemistry of Materials, 2018. **30**(11): p. 3628.
228. Bertuch, A., G. Sundaram, M. Saly, D. Moser, and R. Kanjolia, *Atomic layer deposition of molybdenum oxide using bis(tert-butylimido)bis(dimethylamido) molybdenum.* J. Vac. Sci. Technol. A, 2014. **32**(1): p. 01A119.
229. Nanayakkara, C.E., A. Vega, G. Liu, C.L. Dezelah, R.K. Kanjolia, and Y.J. Chabal, *Role of Initial Precursor Chemisorption on Incubation Delay for Molybdenum Oxide Atomic Layer Deposition.* Chemistry of Materials, 2016. **28**(23): p. 8591.
230. Mattinen, M., P.J. King, L. Khriachtchev, M.J. Heikkilä, B. Fleming, S. Rushworth, K. Mizohata, K. Meinander, J. Räisänen, M. Ritala, and M. Leskelä, *Atomic layer deposition of crystalline molybdenum oxide thin films and phase control by post-deposition annealing.* Materials Today Chemistry, 2018. **9**: p. 17.
231. Jurca, T., A.W. Peters, A.R. Mouat, O.K. Farha, J.T. Hupp, T.L. Lohr, M. Delferro, and T.J. Marks, *Second-generation hexavalent molybdenum oxo-amidinate precursors for atomic layer deposition.* Dalton Transactions, 2017. **46**(4): p. 1172.
232. de Rouffignac, P. and R.G. Gordon, *Atomic Layer Deposition of Praseodymium Aluminum Oxide for Electrical Applications.* Chemical Vapor Deposition, 2006. **12**(2-3): p. 152.
233. Kondo, H., H. Matsui, K. Furuta, M. Sakashita, and S. Zaima, *Formation of Pr Oxide Films by Atomic Layer Deposition Using Pr(EtCp)3Precursor.* Japanese Journal of Applied Physics, 2010. **49**(4): p. 04DA14.
234. Seppälä, S., J. Niinistö, T. Blanquart, M. Kaipio, K. Mizohata, J. Räisänen, C. Lansalot-Matras, W. Noh, M. Ritala, and M. Leskelä, *Heteroleptic Cyclopentadienyl-Amidinate Precursors for Atomic Layer Deposition (ALD) of Y, Pr, Gd, and Dy Oxide Thin Films.* Chemistry of Materials, 2016. **28**(15): p. 5440.

235. Kukli, K., M. Ritala, T. Pilvi, T. Sajavaara, M. Leskelä, A.C. Jones, H.C. Aspinall, D.C. Gilmer, and P.J. Tobin, *Evaluation of a Praseodymium Precursor for Atomic Layer Deposition of Oxide Dielectric Films.* Chemistry of Materials, 2004. **16**(24): p. 5162.
236. Bosund, M., K. Mizohata, T. Hakkarainen, M. Putkonen, M. Söderlund, S. Honkanen, and H. Lipsanen, *Atomic layer deposition of ytterbium oxide using β-diketonate and ozone precursors.* Applied Surface Science, 2009. **256**(3): p. 847.
237. Stafford, N.A., R. Katamreddy, L. Guerin, B. Feist, C. Dussarrat, V. Pallem, C. Weiland, and R. Opila, *Atomic Layer Deposition of Rare-earth Oxide Thin Films for High-k Dielectric Applications.* ECS Transactions, 2019. **19**(2): p. 525.
238. Bergum, K., A. Magraso, H. Fjellvag, and O. Nilsen, *Thin film fabrication and characterization of proton conducting lanthanum tungstate.* Journal of Materials Chemistry A, 2014. **2**(43): p. 18463.
239. Knapas, K., A. Rahtu, and M. Ritala, *Etching of Nb2O5 Thin Films by NbCl5.* Chemical Vapor Deposition, 2009. **15**(10-12): p. 269.
240. Aarik, J., A. Aidla, K. Kukli, and T. Uustare, *Deposition and etching of tantalum oxide films in atomic layer epitaxy process.* Journal of Crystal Growth, 1994. **144**(1): p. 116.
241. Kvalvik, J.N., K.B. Kvamme, K. Almaas, A. Ruud, H.H. Sønsteby, and O. Nilsen, *LiF by atomic layer deposition—Made easy.* Journal of Vacuum Science & Technology A, 2020. **38**(5): p. 050401.
242. Fjellvåg, Ø.S., *Tynne filmer og nanobelter for batterier, Syntese og karakterisering av katodematerialer for litium- og natriumionbatterier*, in *Department of Chemistry*. 2014, University of Oslo.
243. Kvamme, K.B. and O. Nilsen, *Li_3Po_3 by Atomic Layer Deposition*. 2020: To be submitted.
244. Choi, J.G. and L.T. Thompson, *XPS study of as-prepared and reduced molybdenum oxides.* Applied Surface Science, 1996. **93**(2): p. 143.
245. Magneli, A., *Structures of the ReO3-type with recurrent dislocations of atoms: `homologous series' of molybdenum and tungsten oxides.* Acta Cryst. , 1953. **6**: p. 495.
246. Gruber, H. and E. Krautz, *Untersuchungen der elektrischen Leitfähigkeit und des Magnetowiderstandes im System Molybdän-Sauerstoff.* 1980. **62**(2): p. 615.
247. Leisegang, T., A.A. Levin, J. Walter, and D.C. Meyer, *In situ X-ray analysis of MoO3 reduction.* 2005. **40**(1-2): p. 95.
248. Sawant, K.K., V.P. Mundada, and V.J. Patel, *Development and Optimization of w/o/w Multiple Emulsion of Lisinopril Dihydrate Using Plackett Burman and Box-Behnken Designs.* Journal of Nanomedicine & Nanotechnology, 2017. **08**.
249. Coles, S.R., D.K. Jacobs, J.O. Meredith, G. Barker, A.J. Clark, K. Kirwan, J. Stanger, and N. Tucker, *A design of experiments (DoE) approach to material properties optimization of electrospun nanofibers.* 2010. **117**(4): p. 2251.
250. Nourbakhsh, A., B. Ganjipour, M. Zahedifar, and E. Arzi, *Morphology optimization of CCVD-synthesized multiwall carbon nanotubes, using statistical design of experiments.* Nanotechnology, 2007. **18**(11): p. 115715.
251. Kukovecz, Á., D. Méhn, E. Nemes-Nagy, R. Szabó, and I. Kiricsi, *Optimization of CCVD synthesis conditions for single-wall carbon nanotubes by statistical design of experiments (DoE).* Carbon, 2005. **43**(14): p. 2842.
252. Cao, B., L.A. Adutwum, A.O. Oliynyk, E.J. Luber, B.C. Olsen, A. Mar, and J.M. Buriak, *How To Optimize Materials and Devices via Design of Experiments and Machine Learning: Demonstration Using Organic Photovoltaics.* ACS Nano, 2018. **12**(8): p. 7434.
253. Voznyy, O., L. Levina, J.Z. Fan, M. Askerka, A. Jain, M.-J. Choi, O. Ouellette, P. Todorović, L.K. Sagar, and E.H. Sargent, *Machine Learning Accelerates Discovery of Optimal Colloidal Quantum Dot Synthesis.* ACS Nano, 2019. **13**(10): p. 11122.
254. Kang, Y., L. Li, and B. Li, *Recent progress on discovery and properties prediction of energy materials: Simple machine learning meets complex quantum chemistry.* Journal of Energy Chemistry, 2021. **54**: p. 72.
255. Banko, L., Y. Lysogorskiy, D. Grochla, D. Naujoks, R. Drautz, and A. Ludwig, *Predicting structure zone diagrams for thin film synthesis by generative machine learning*. 2020.

256. Hansen, P.-A., C.S. Granerød, Ø. Prytz, and O. Nilsen, *Controlling luminescence and quenching mechanisms in subnanometer multilayer structure of europium titanium oxide thin films.* Journal of Luminescence, 2019. **215**: p. 116618.
257. Yanguas-Gil, A., J.A. Libera, and J.W. Elam, *Modulation of the Growth Per Cycle in Atomic Layer Deposition Using Reversible Surface Functionalization.* Chemistry of Materials, 2013. **25**(24): p. 4849.
258. Penza, M., M. Tagliente, L. Mirenghi, C. Gerardi, C. Martucci, and G. Cassano, *Tungsten trioxide (WO3) sputtered thin films for a NOx gas sensor.* Sensors and Actuators B: Chemical, 1998. **50**(1): p. 9.
259. Mardare, C.C. and A.W. Hassel, *Review on the Versatility of Tungsten Oxide Coatings.* physica status solidi (a), 2019. **216**(12): p. 1900047.
260. Vitry, D., J.-L. Dubois, and W. Ueda, *Strategy in achieving propane selective oxidation over multi-functional Mo-based oxide catalysts.* Journal of Molecular Catalysis A: Chemical, 2004. **220**(1): p. 67.
261. Ueda, W., D. Vitry, and T. Katou, *Crystalline MoVO based complex oxides as selective oxidation catalysts of propane.* Catalysis Today, 2005. **99**(1): p. 43.
262. Petnikota, S., S.K. Marka, V.V.S.S. Srikanth, M.V. Reddy, and B.V.R. Chowdari, *Elucidation of few layered graphene-complex metal oxide (A2Mo3O8, A=Co, Mn and Zn) composites as robust anode materials in Li ion batteries.* Electrochimica Acta, 2015. **178**: p. 699.
263. Zhu, F., Z. Xiao, F. Zhang, L. Yan, and A. Huang, *Donor doping process and white light generation in CaMoO4 powders with multivalence Pr codoping.* Journal of Luminescence, 2011. **131**(1): p. 22.
264. Mahlik, S., M. Behrendt, M. Grinberg, E. Cavalli, and M. Bettinelli, *High pressure luminescence spectra of CaMoO4: Ln3+ (Ln= Pr, Tb).* Journal of Physics: Condensed Matter, 2013. **25**(10): p. 105502.
265. Verma, A. and S.K. Sharma, *Dual-mode luminescence: a new perspective in calcium molybdate phosphor for solar cell application.* Journal of Materials Science: Materials in Electronics, 2019. **30**(12): p. 11778.

Paper I

Area-selective atomic layer deposition of molybdenum oxide

Kvalvik, J.N, Borgersen, J., Hansen, P.-A. and Nilsen, O. Journal of Vacuum Science & Technology A **38**, 042406 (2020)

JVST A
Journal of Vacuum Science & Technology A

ARTICLE

avs.scitation.org/journal/jva

Area-selective atomic layer deposition of molybdenum oxide

Cite as: J. Vac. Sci. Technol. A 38, 042406 (2020); doi: 10.1116/6.0000219
Submitted: 28 March 2020 · Accepted: 19 May 2020 ·
Published Online: 17 June 2020

Julie Nitsche Kvalvik,[1] Jon Borgersen,[2] Per-Anders Hansen,[1] and Ola Nilsen[1,a)]

AFFILIATIONS

[1]Centre for Materials Science and Nanotechnology, Department of Chemistry, University of Oslo, Postboks 1033, Blindern, 0315 Oslo, Norway
[2]Centre for Materials Science and Nanotechnology, Department of Physics, University of Oslo, Postboks 1048, Blindern, 0315 Oslo, Norway

Note: This paper is a part of the Special Topic Collection on Area Selective Deposition.
[a)]**Electronic mail:** ola.nilsen@kjemi.uio.no

ABSTRACT

Area-selective bottom-up synthesis routes of thin films are required to overcome the current limits in lithography, and such growth can be achieved with high quality and nanometer thickness control by area-selective atomic layer deposition (AS-ALD). However, the current range of materials demonstrated deposited by AS-ALD is limited, and no processes for molybdenum oxide have been available so far. In this work, the authors explore the properties of a new ALD precursor, $MoCl_4O$, for deposition of molybdenum oxides by ALD. $MoCl_4O$ is administered at room temperature during deposition, making it readily available for use. When reacted with a combination of water and ozone, it leads to an AS-ALD process for deposition of MoO_x—the first reported. The process is perfectly selective for growth on glass as compared to Si(100) substrates for deposition temperatures between 200 and 300 °C, with a growth rate of 0.72 Å/cycle at 300 °C. The process is attempted on a range of substrates proving good growth on soda-lime glass and LiF and no growth on Si(100), silica, Na_2CO_3, $CaCO_3$, Li_3PO_3, or Li_2SiO_3. The findings of this study indicate an *activated* process by diffusion of sodium or lithium through the film during growth. The obtained films have further been characterized by x-ray photoelectron spectroscopy, scanning electron microscopy, x-ray diffraction, and atomic force microscopy, revealing films with an RSM roughness of 23 nm with the presence of crystalline MoO_2 (C P/m) when deposited at 300 °C and crystalline Mo_9O_{26} when deposited at 250 °C. The rough MoO_x thin films may be applicable for electrocatalysis, gas sensors, or lithium-ion batteries. The findings of this study enable AS-ALD synthesis of molybdenum oxide with excellent selectivity not dependent on intermittent etching cycles during growth.

I. INTRODUCTION

The semiconductor industry is currently approaching the limits of resolution in lithography—leaving a technology gap that may be filled with precise bottom-up synthesis approaches.[1] One obvious choice to fill this gap is by atomic layer deposition (ALD), or more specifically, area-selective ALD (AS-ALD). ALD, in general, is known to give high quality films with supreme thickness control and conformity. AS-ALD will ease processing in comparison to conventional ALD, as fewer etching steps are required. Despite the fact that the concept has been around for 15 years,[2] we have not seen a true boom in AS-ALD processes until now.[3] This has yet to reach MoO_3, which takes part in many applications also requiring precise manufacturing, such as catalysis,[4–6] nanostructured gas sensors,[7] injection layers in inverted organic photovoltaics,[8] antibacterial coatings,[9] electrochromic devices,[10] and batteries,[11] among others. For applications within electrocatalysis,[12] gas sensors,[13] or lithium-ion batteries,[14] porous or rough MoO_x films can be beneficial. A whole range of techniques has already been employed to deposit MoO_3 thin films, although without area selectivity. This includes thermal evaporation,[15] RF sputtering,[16] flash evaporation,[17] metalorganic chemical vapor deposition,[18] and ALD,[19] which is the subject of this study.

The range of processes for deposition of MoO_3 by ALD is limited, particularly for deposition at higher temperatures as the majority of molybdenum precursors decompose at 180 °C or below. Deposition of MoO_3 by ALD was first reported in 2010 (Ref. 19) using $Mo(CO)_6$ as the Mo source together with O_3 and H_2O in the

range of 152–172 °C, after which the precursor decomposes. Si $(CH_3)_3$cpMo$(CO)_2(\eta^3$-2-methylallyl) is in like manner reported to produce MoO_3 together with O_3 at 250–300 °C.[20] This process does, however, require an initial heating of the Si(100) substrate at 350 °C to prevent a nucleation delay of the following MoO_x deposition. Another recent precursor for deposition of MoO_3 is bis(ethylbenzene)Mo, which together with H_2O shows ALD growth in the range of 135–150 °C.[21] Very recently, $MoO_2(iPr_2AMD)_2$ (Ref. 22) has been demonstrated as a suitable precursor to form MoO_3 up to its decomposition temperature of 175 °C using O_3 as the oxygen source. $(N^tBu)_2(NMe_2)_2Mo$ was introduced as an alternative in 2015 and forms MoO_3 with O_3 in the temperature range of 100–300 °C[23] or 50–350 °C using plasma O_2.[24] The tungsten counterpart of $(N^tBu)_2(NMe_2)_2Mo$ has also been used as an ALD precursor[25] to form WO_3 with H_2O as the coreactant and in combination with $La(thd)_3$ to form the proton-conducting ternary oxide $La_{28-x}W_{4+x}O_{54}$. The same work also mentions using WCl_4O as a W source but was not pursued further as the WCl_4O and H_2O process seemed to stop after a few cycles and had a limited growth rate. Based on the similar chemistry of Mo and W, we wanted to explore if this would also be the case for $MoCl_4O$ or if it would work as an ALD precursor. This is the topic of this work. With $MoCl_4O$, we are now able to expand the MoO_x toolbox to include the $MoCl_4O + (H_2O + O_3)$ process. However, to our surprise, this system exhibits clear signs of area-selective growth, as initial experiments revealed no film on Si(100) substrates, while glass substrates were clearly coated (Fig. 1).

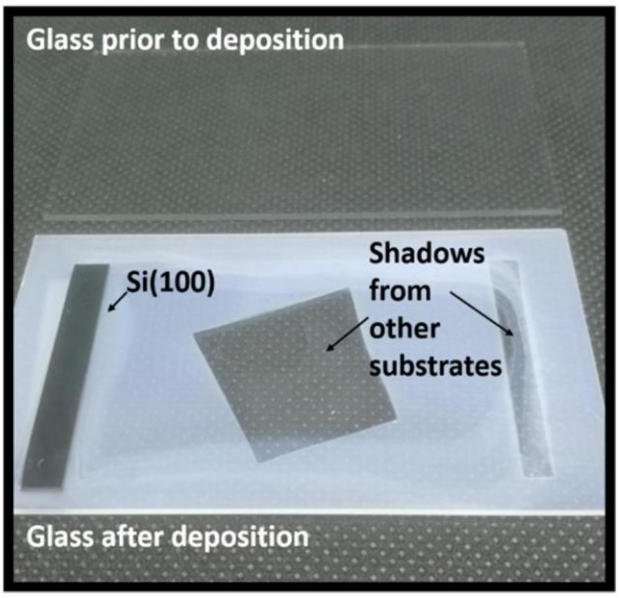

FIG. 1. Picture of an MoO_x thin film on glass and Si deposited at 300 °C using 1000 cycles of $MoCl_4O$ and $(H_2O + O_3)$. The film is clearly visible on the glass plate after deposition as compared to prior to deposition, but no film could be detected on the Si(100) strip.

Area-selective ALD is an emerging field particularly useful in semiconductor processing for electronics where numerous lithography steps are required.[26,27] An overview of the field is given in Ref. 24 and can be summarized as divided into the following approaches: *Inherent* systems, where no extra measures are taken to make the system area-selective; the use of *activators*, using catalytic reactions on the surfaces, plasma enhanced areas, etc., such as for deposition of Fe_2O_3 and NiO by O_2 gas with *t*-butyl ferrocene/nickelocene on Pt and Ir substrates that dissociate O_2, and not on the inert SiO_2, Al_2O_3, and Au substrates;[28] the use of *inhibitors*, such as for deposition of SiO_2 on GeO_2, SiN_x, SiO_2, and WO_3, and not on Al_2O_3, TiO_2, and HfO_2,[29] where acetylacetonate chemoselectively inhibits growth by selective adsorption on the latter surfaces. Of these approaches, using inhibitors is by far the most used.

Other examples using inhibitors include the deposition of TiO_2 on gold substrates using self-assembled monolayers (SAMs) as inhibitors,[30] Ru on Cu lines using amino-functionalized SAMs as inhibitors,[31] and CoO on SiO_2/MgO using polystyrene as inhibitors.[32] The combination of atomic layer etching (ALE) and ALD is also employed to make thicker films only on the desired substrate. For example, Al_2O_3 has been deposited selectively on Si and not on octadecylphosphonic acid (OPDA)-SAM inhibited Cu with intermitting acid etch cycles.[33]

The figure of merit for quantification of the selectivity of a system is termed selectivity, *S*, and is in Ref. 24 defined as *the amount (or rate) of one product relative to the total amount (or rate) of all products formed. S* also varies with the number of ALD cycles used and must therefore be reported together.[27] An example of a reported selectivity is 2000:1 for Pt versus SiO_2 substrates for the previously mentioned Fe_2O_3 system using 300 cycles.[28]

In this study, we further explore the effect of different types of substrates on the selectivity of the $MoCl_4O + (H_2O + O_3)$ system to shed light on possible mechanisms behind our observations.

II. EXPERIMENT

A. Atomic layer deposition

All depositions were performed in an F-120 Sat reactor (ASM Microchemistry), in the temperature range of 200–350 °C. The purging gas was N_2 at 300 cm^3 min^{-1} from gas cylinders (Praxair, 99.999%, further purified through a Mykrolis purifier) providing a background pressure of ~4 mbar. The depositions were carried out using $MoCl_4O$ (Sigma-Aldrich, 97%) as the Mo source and distilled H_2O and O_3 pulsed simultaneously as the O source. O_3 was supplied from an In USA ozone generator (AC-2505) at 15 wt. % O_3 in O_2, using O_2 from a gas cylinder (Praxair, 99.5%). Both $MoCl_4O$ and H_2O were kept at room temperature in external containers, and $MoCl_4O$ was assisted by N_2 carrier gas. Standard pulsing times were 3 s for both $MoCl_4O$ and $O_3 + H_2O$, followed by 3 s purging after $MoCl_4O$ and 5 s after $O_3 + H_2O$, unless otherwise specified. The times were chosen based on experience with similar systems and gave here uniform films and reproducible data. A standard deposition consisted of 1000 cycles at a deposition temperature of 300 °C. The LiF seeding layers were deposited using LiO^tBu (Sigma-Aldrich, 97%) and NH_4F (Sigma-Aldrich, 99.99%) based on an internally developed process.[34] The LiO^tBu and NH_4F precursors were kept at 130 and 95 °C, respectively, and pulsed/purged with 5/5 s and 7/3 s, respectively.

A variety of substrates were used, including Si(100) with a native oxide layer, Si(100) with the following ALD-deposited thin films—$CaCO_3$ [from $Ca(thd)_2$, CO_2 and O_3 (Ref. 35)], Na_2CO_3 [from NaO^tBu, H_2O, and CO_2 (Ref. 36)], Li_3PO_3 [from LiO^tBu, Me_3PO_3, and water, and x-ray photoelectron spectroscopy (XPS) revealing a surface layer of Li_2CO_3], LiF and Li_2SiO_3 [from lithium trimethylsilanolate and H_2O (Ref. 37)]—conventional soda-lime glass containing 15 mol. % Na_2O_3 (Glaswarenfabrik Karl Heckt), and silica. Si(100), glass, and silica substrates were all washed with ethanol and blown dry prior to deposition. The other substrates were left untouched to not alter the films already deposited on them.

B. Thin film characterization

The thicknesses of the films were measured using a J. A. Woollam α-SE spectroscopic ellipsometer in the range of 390–900 nm, with the COMPLETEEASE software and Cauchy models to analyze the data. The models used two layers, one dense in the bottom and one rough on top, and took into consideration that MoO_x is absorbing. For each sample, three spots were measured. It was spot dependent how easy it was to model the ellipsometry data, probably due to variations of the roughnesses of the films. Scanning electron microscopy (SEM) was performed using a HITACHI TM3000 SEM with a working distance of ~9 mm and an acceleration voltage of 15 kV. A Quantax70 energy dispersive x-ray spectrometer equipped with a silicon drift detector and Cu Kα radiation was used for elemental analysis. The acquisition time for each measurement was 5 min. XPS measurements were carried out using a ThetaProbe instrument from ThermoScientific. The incident x-ray beam was Al Kα (1.487 keV) and 4 keV Ar^+ was used for sputtering. The C1s peak at 285 eV stemming from carbon contamination was used as internal standard for fitting of the XPS spectra. X-ray diffraction (XRD) was performed to study the crystallinity of the samples, using a Bruker D8 Discovery Diffractometer, with Cu Kα1 radiation and a Ge(111) monochromator in a traditional Bragg–Brentano setup. Atomic force microscopy (AFM) was performed using a Park Systems XE-70 AFM equipped with a PPP-CONTSCR cantilever in the contact mode. The AFM micrographs were processed with the GWYDDION software. Four-point probe inline resistivity measurements was performed using a Keithley 2400 SourceMeter.

C. Lithography

The LiF films were patterned using photolithography. A Microposit S1813 positive photoresist was applied using a spin coater, before the sample was baked at 120 °C for 60 s on a hot plate. The pattern was exposed in a Heidelberg μPG501 maskless lithography system and developed in the Microposit MF351 developer diluted with three parts de-ionized (DI) water. Following the development, the sample was rinsed for 1 s in DI water and immediately blown dry in N_2 gas. The exposed LiF was etched by immersing the sample in DI water for 1 min, before the photoresist was stripped by soaking in acetone for 4 min. Unfortunately, 1 min of etching time was found to be excessive, and caused a loss of resolution in the pattern, however, still suitable to prove the possible use within lithography.

D. Selectivity calculations

The selectivity is calculated using the relation given in the Introduction, namely, that selectivity is the "the amount (or rate) of one product relative to the total amount (or rate) of all products formed."[27] This translates to the following equation where S is the selectivity, n is the number of cycles, and Θ_1 is the measured fraction covered by nuclei at growth surface relative to the measured fraction at an adjacent nongrowth surface, Θ_2. The full derivation of this is found in Ref. 27,

$$S(n) = \frac{\Theta_1 - \Theta_2}{\Theta_1 + \Theta_2}. \quad (1)$$

The measured fraction covered by nuclei is directly proportional to the deposited film volume. It is therefore possible to get a measure of this by various characterization methods such as spectroscopic ellipsometry, Auger electron spectroscopy, or electron dispersive x-ray spectroscopy (EDS), which is used in this case. Here, the at. % of Mo versus (Si + Mo) is used as θ for films deposited on both glass and Si(100) substrates.

E. Thermodynamic calculations

Thermodynamic calculations were performed using the HSC CHEMISTRY 8 software from Outotec.

III. RESULTS AND DISCUSSION

A. MoO_x thin film growth

Using the standard pulsing and purging times, MoO_x was successfully deposited by atomic layer deposition with similar growth rates on glass (0.72 Å/cycle) and LiF (0.69 Å/cycle) substrates. It was possible to obtain a sufficient dose of $MoCl_4O$ kept at room temperature when extra carrier gas was flushed through the bubbler during pulsing. The films on glass appeared light blue. Based on this, glass was used as the standard substrate for subsequent investigations. A test for chemical vapor deposition growth was performed by pulsing only $MoCl_4O$ and keeping the reaction chamber at 300 °C. This resulted in no detectable film proving that the precursor does not decompose during operation. Initially, shorter pulsing and purging times (1s/ 1s/ 2s/ 3s) than the standard (3s/ 3s/ 3s/ 5s) mentioned in Sec. II. Experiments were tested, but this led to gradients with reduced growth along the flow direction in the reactor chamber. The standard pulsing and purging times were the shortest that also yielded even, reproducible films. No film was obtained using standard pulsing parameters on either Li_2SiO_3, Si(100) with a native oxide layer, $CaCO_3$, Na_2CO_3, Li_3PO_3, or silica substrates, as measured with spectroscopic ellipsometry. See the supplementary material[50] for the measured thicknesses before and after deposition.

The growth per cycle of MoO_x versus deposition temperature as grown on glass substrates is shown in Fig. 2. For 1000 cycles, the growth per cycle rapidly increases when the deposition temperature is increased from 275 to 300 °C, indicating a kinetically limited growth at temperatures below 300 °C. For 5000 cycles, there is a slight increase, although still within the error margin, between 300 and 350 °C.

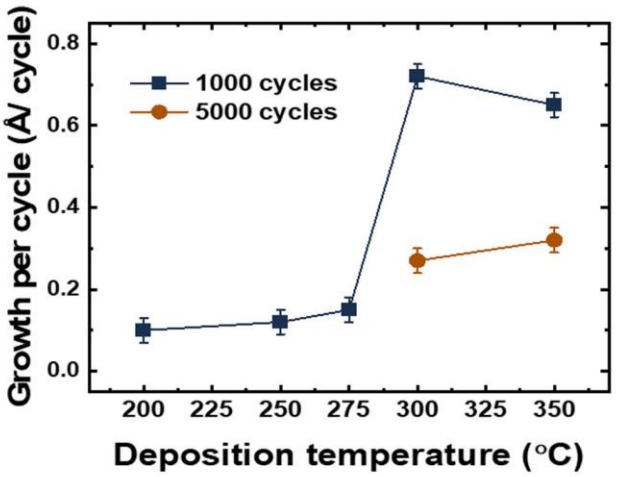

FIG. 2. Growth per cycle on glass vs deposition temperature of MoO_x for the $MoCl_4O/(O_3 + H_2O)$ system using 1000 (squares) or 5000 (circles) ALD cycles. The uncertainties are estimated from the variance in data obtained for 1000 cycles at 300 °C for three separate experiments.

The linearity with respect to the number of ALD cycles was investigated at 300 °C (Fig. 3) proving an overall reduction in growth per cycle with increased film thicknesses. ALD processes are usually regarded as linear with the number of deposition cycles, unless nucleation or evolution of texture affects the available surface area. The current observation with temperature and thickness dependent

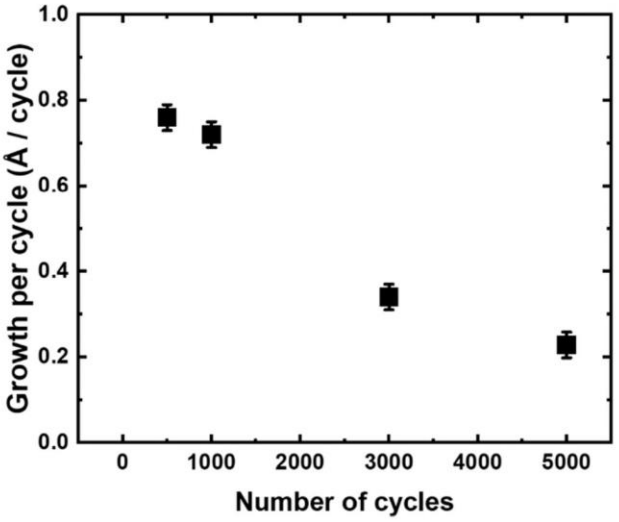

FIG. 3. Growth per cycle of MoO_x vs number of cycles for the $MoCl_4O/(O_3 + H_2O)$ at 300 °C. The uncertainties are estimated from the variance in data obtained for 1000 cycles at 300 °C for three separate experiments.

TABLE I. Growth rate of MoO_x on glass using $MoOCl_4$ and a selection of oxygen sources at a substrate temperature of 300 °C and 1000 cycles, as measured with spectroscopic ellipsometry.

O source	Growth per cycle (Å)
$O_3 + H_2O$ pulsed simultaneously	0.72
Only O_3	0.12
Only H_2O	0.10

growth indicates that the process may be controlled by diffusion of an active component from the substrate itself. This also explains why the growth per cycle increases between 300 and 350 °C for 5000 cycles, as the growth of thicker films is more limited by diffusion, which is in turn enhanced at higher temperatures. See the supplementary material[50] for attempts on modeling the evolution in film thickness based on diffusion limited principles.

As this system exhibits clear selectivity with respect to the substrate material, further investigations were performed to gain more insight into its origin. A first step was investigating the oxygen source, if both O_3 and H_2O play an active part in the growth. When changing the oxygen source to only H_2O or O_3, a clear reduction of the overall growth rates was observed (Table I). A similar dependency is previously reported for when $Mo(CO)_6$ is used as an Mo source, although at a reduced magnitude.[19] For the $Mo(CO)_6$ process, the effects of omitting H_2O was negligible, but a reduction in growth rate of about 75% was observed when omitting O_3.

XRD analysis of the films shows a strong dependency of the crystallinity with deposition temperature (Fig. 4). Films deposited at 250 °C match well with Mo_9O_{26} (P 2/C), while the crystallinity is reduced at 275 °C, and at 300 °C, there is only one clear peak present, and this matches well with MoO_2 (C 2/m, tugarinovite). Mo_9O_{26} is a Magnéli phase with a structure closely related to the

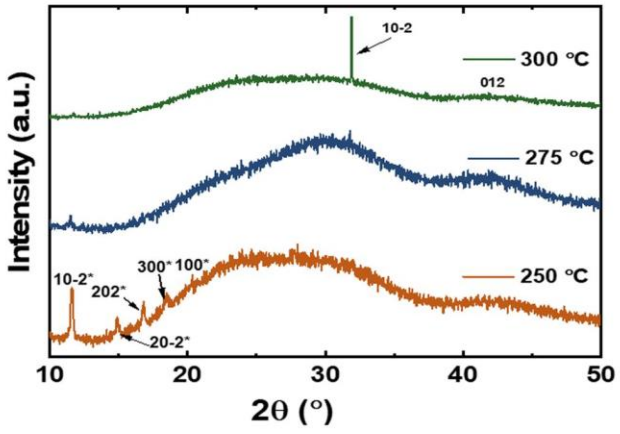

FIG. 4. XRD diffractograms of molybdenum oxide thin films deposited at varying temperatures using 1000 cycles. Selected reflexes from Mo_9O_{26} (P 2/C, with asterisk) (Ref. 42) and MoO_2 (C 2/m, tugarinovite, no asterisk) (Ref. 43) are indexed for comparison.

more common layered α-MoO_3,[38] which consists of zig-zag layers of distorted MoO_6 octahedra.[39] This is similar for Mo_9O_{26}, but this structure also includes crystallographic shear planes as described by Magnéli. The crystallographic shear planes reduce the overall oxidation state for Mo from +6 in α-MoO_3 to approximately +5.8 in Mo_9O_{26} without introducing oxygen vacancies. A previous study from our group, using the $Mo(CO)_6 + (O_3 + H_2O)$ process, showed that the films were amorphous as deposited at 167 °C, but crystallized to the metastable β-MoO_3 when annealed at 400 °C for 8 min and as α-MoO_3 when annealed at 600 °C for 8 min.[40] Another very recent study on MoO_3 from our group identifies the crystallization process as both time and temperature dependent proving crystallization of β-MoO_3 at only 185 °C when annealed for an extended amount of time (24 h).[41] The formation of MoO_2 is further discussed later in the text.

The microstructure of thin films deposited on glass substrates was investigated with SEM and AFM (Fig. 5). The microstructure was similar for all investigated deposition temperatures (200–350 °C), and the micrographs in Fig. 5 are thus representative for all the investigated samples. The topography appears rough and shows some signs of pinholes. The AFM micrograph further shows that some areas are denser with a thickness around 72 nm, but some areas again have taller grains and more pinholes. The occurrence of pinholes reduces slightly with higher deposition temperatures, but the topography remains rough. The RMS roughness is 23 nm as estimated from the AFM micrograph for a film with total thickness of 72 nm. To shed more light on the film quality, a four-point probe inline resistivity measurement was performed on a 114 nm thick film deposited at 300 °C. The film was insulating at room temperature, i.e., the sheet resistance was above 100 MΩ/sq.

XPS was performed on selected samples to investigate the state of molybdenum and to reveal the presence of any impurities that may be embedded in the growth process. The survey spectrum for a sample deposited at 300 °C on glass is shown in Fig. 6. This shows that beside the expected peaks from oxygen and molybdenum, a large amount of sodium is also found in the films. The Cl $p_{3/2}$ peak, which is the peak primarily used for analysis of chlorine by XPS, is normally found around 200 eV and is absent in the spectrum below.

Two XPS scans were performed on two different spots of a sample deposited at 300 °C to investigate the oxidation state of Mo (Fig. 7). For the Mo $3d_{3/2}$ peak, the peak positions are at 236.1 and 235.4 eV for the two scans, both within the expected range for the valance being +6.[44] The same goes for the Mo $3d_{5/2}$ where the peak positions are at 232.8 and 232.1 eV. The observed shift for both Mo 3d peaks between the two scans is less than expected if the valance indeed was different in the two spots.

A depth profile was also obtained by XPS on a MoO_x film deposited on glass at 300 °C, as shown in Fig. 8. It shows a relatively homogeneous distribution of sodium ions throughout the film, probably due to extended diffusion through the 2-h cooling process after the deposition. It should be kept in mind that the

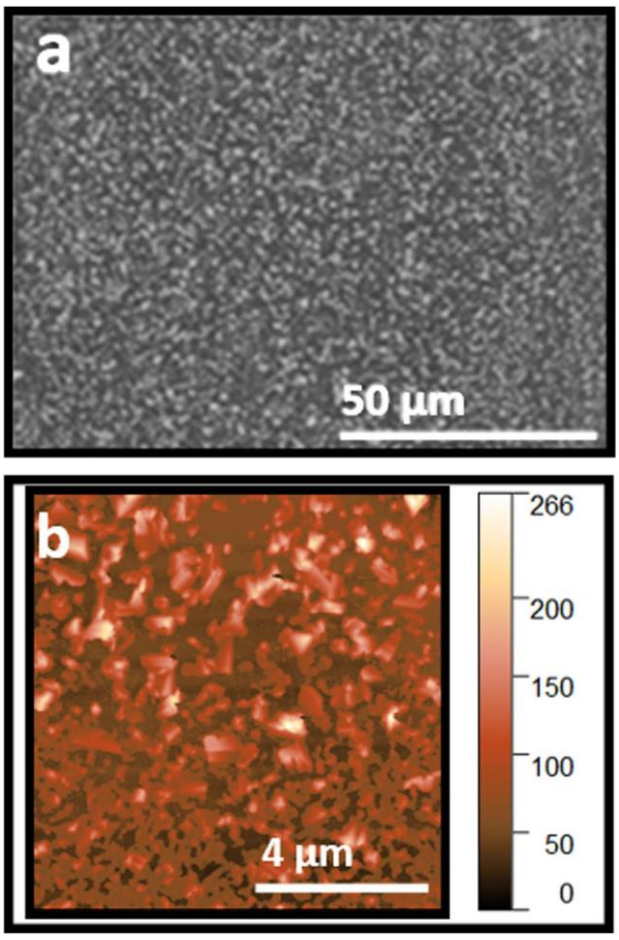

FIG. 5. SEM micrograph (a) of MoO_x deposited on glass at 250 °C and AFM micrograph (b) of MoO_x deposited on glass at 300 °C using 1000 cycles.

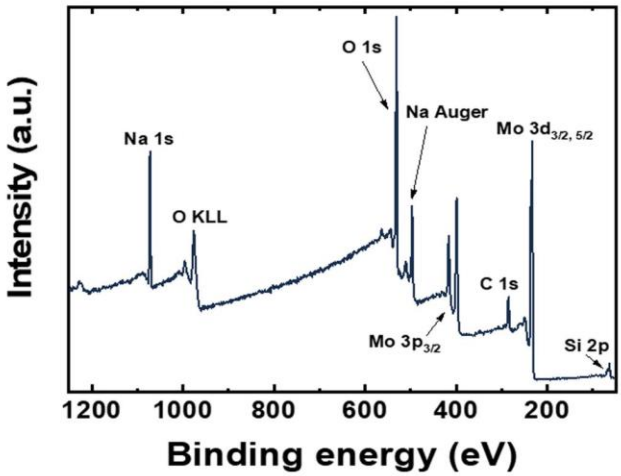

FIG. 6. XPS survey scan of MoO_x thin film deposited at 300 °C on glass.

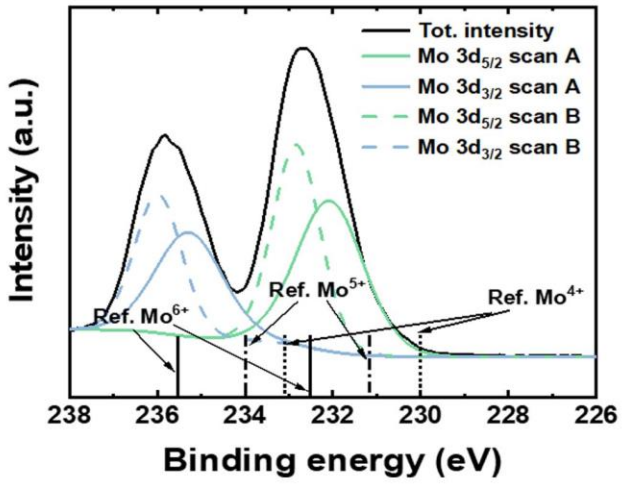

FIG. 7. XPS scans of Mo 3d peaks to identify the oxidation state of molybdenum in an MoO_x thin film deposited at 300 °C on glass. Two scans, A and B, were performed at two different spots on the same sample during the same session. Expected peak positions for Mo^{6+}, Mo^{5+}, and Mo^{4+} from Ref. 44 are included for comparison.

argon sputtering during depth profiling can also affect the distribution of sodium throughout the film. We do observe an accumulation of sodium at the surface of the film with 6.6% Na at zero etch time.

Experiments with prolonged purging times were performed to investigate how diffusion of sodium ions affect the growth rates of the MoO_x thin film. If the growth is dependent on diffusion of sodium through the film, the growth rate should be affected by the purging times, leading to increased growth for longer purges, as this allows for more time for diffusion controlled processes.[45] The results of such an investigation is shown in Table II and support our hypothesis, although with a higher dependency on the purging times than anticipated from Fick's laws of diffusion.

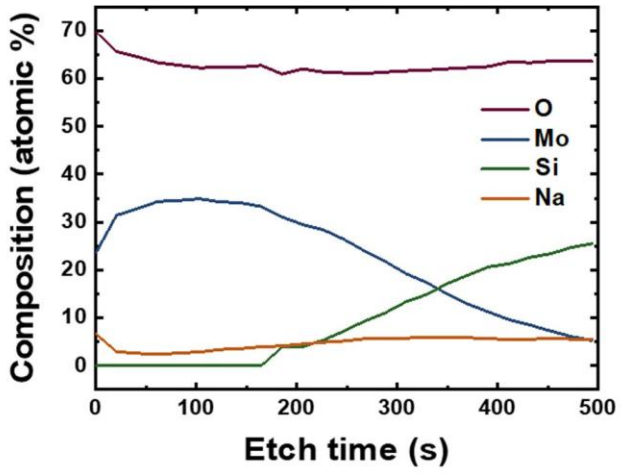

FIG. 8. XPS depth profile of MoO_x thin film as deposited at 300 °C on glass.

TABLE II. Growth rate of $MoCl_4O/(O_3 + H_2O)$ on glass as a function of purging times at a substrate temperature of 300 °C as measured with spectroscopic ellipsometry.

Purging time after $MoCl_4O$ pulse (s)	Purging time after $O_3 + H_2O$ pulse (s)	Total cycle time (s)	Growth per cycle (Å)
3	5	14	0.72
6	10	22	0.83
9	15	30	1.15

B. Area-selective growth

EDS measurements were performed on a number of samples deposited at various temperatures to quantify the selectivity of the process as a function of deposition temperature. Both growth (glass) and nongrowth [Si(100)] surfaces were investigated. As no molybdenum could be detected at the Si(100) surface for depositions at 300 °C or below, the selectivity is here reported as perfect selectivity, i.e., 1. For the film deposited at 350 °C, the selectivity was calculated from the EDS measurements to be 0.85 for glass over Si(100). See the supplementary material[50] for details about this calculation.

To illustrate the selectivity of the system further, a pattern was produced by lithography on a 45 nm thick LiF film made by ALD on Si(100). Thus, both growth and nongrowth areas were present on the same substrate. A standard MoO_x deposition was then performed on top of this patterned surface. An SEM micrograph of the resulting sample is shown in Fig. 9 where the brighter areas correspond to deposition of MoO_x. We found it challenging to perform good lithography on LiF due to its high solubility in water. Yet, samples with clear patterns were obtained.

To further illuminate the selectivity of the $MoCl_4O + (H_2O + O_3)$ system, EDS mapping was performed on an MoO_x film deposited on patterned LiF on Si(100) (Fig. 10). Both molybdenum and fluorine are present within the desired pattern in significant amounts. Attempts to quantify the concentration of molybdenum outside this pattern result in only 0.02 at. %, whereas it revolves around 8 at. % in the pattern itself. The reported values must not be considered absolute concentrations since the EDS analysis volume penetrates through the film and into the substrate. However, they do prove a selectivity for MoO_x growth of around 400 times higher growth on the LiF pattern than in the surrounding area, even with imperfect patterning.

C. Discussion

We have here reported using the oxychloride $MoCl_4O$ for deposition of MoO_x by atomic layer deposition. Equation (2) shows

FIG. 9. SEM micrograph (a, left) illustrating the selectivity of the MoO_x system as deposited on LiF. The pattern is the University of Oslo's logo (b, right). The LiF film under the lines of the logo shown in (b) was removed with lithography prior to deposition of MoO_x. The circle in the micrograph is the area where the EDS measurements in Fig. 10 are taken.

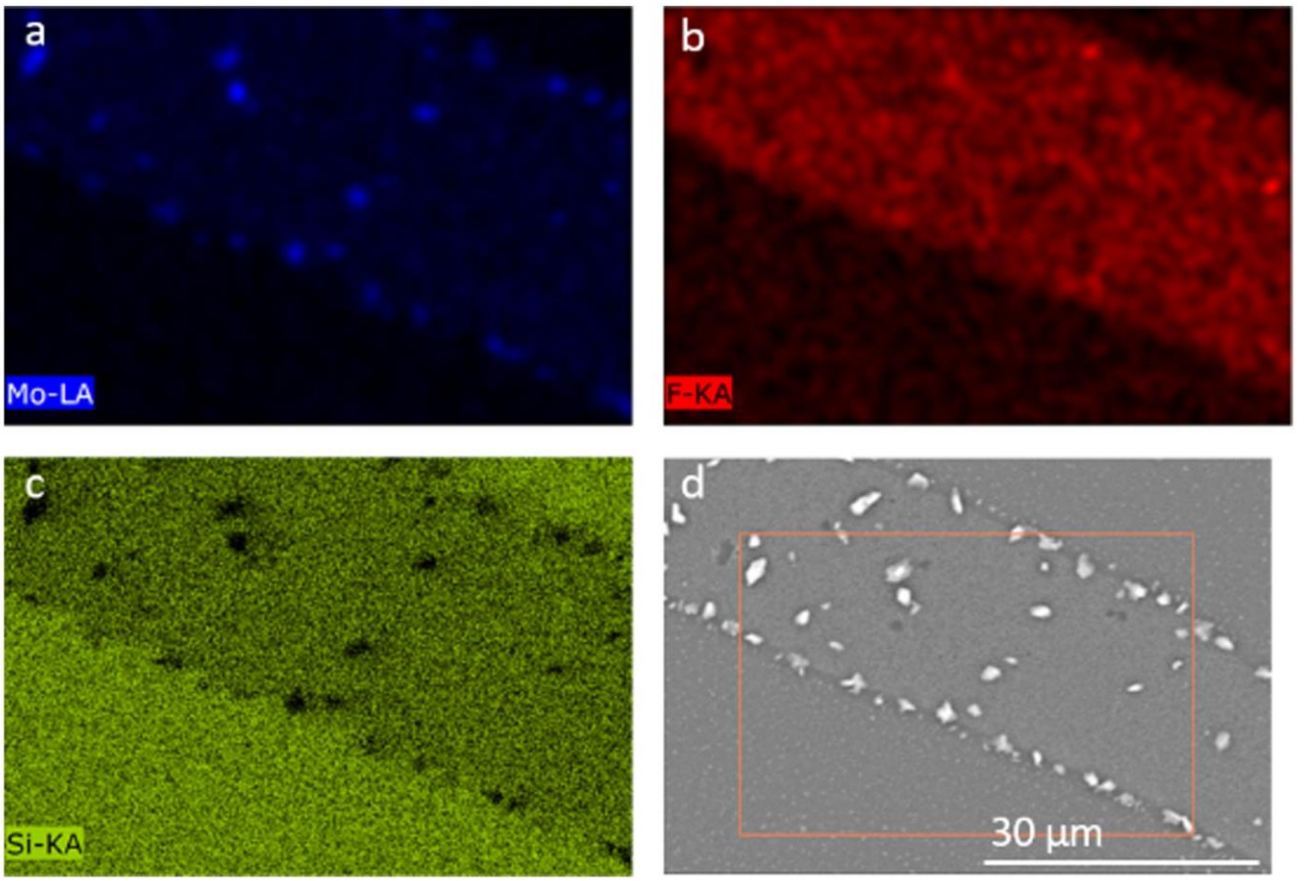

FIG. 10. EDS mapping of molybdenum Lα (a), fluorine Kα as a measure of LiF (b) and silicon Kα (c) in addition to an SEM micrograph of the surrounding area (d) of an MoO_x film deposited at 300 °C on a patterned LiF substrate. The square in subfigure (d) corresponds to the area in which the EDS measurements are performed within.

the proposed reaction between H_2O and $MoCl_4O$,

$$MoCl_4O(g) + 2H_2O(g) \rightarrow MoO_3(s) + 4HCl(g). \quad (2)$$

The calculated equilibrium constant, K, of this reaction is $2.3 \cdot 10^8$, $8.4 \cdot 10^7$, and $3.7 \cdot 10^7$ at 200, 250, and 300 °C, respectively. These large values point to a very favorable reaction, which is consistent with our observations. The equilibrium constant decreases one order of magnitude from 200 to 300 °C but still remain at a very high level. Even though $MoCl_4O$ is known to thermally and photocatalytically decompose to $MoCl_3O$ and Cl_2 already at room temperature, we still observed $MoCl_4O$'s distinct dark green color also after being connected to the ALD reactor in a glass bubbler with inert gas for weeks during deposition campaigns.[46]

A possible reason why $MoCl_4O$ has not previously been explored as an ALD precursor is the failed attempts to use the tungsten analog, WCl_4O, to deposit WO_3. The previous attempts of using WCl_4O as an ALD precursor showed no growth on Si(100), but signs of growth were seen on La_2O_3 and Al_2O_3[25] when H_2O was used as the oxygen source. Likewise, we did not observe growth on Si(100), and based on our study, we would anticipate similar reaction schemes for WCl_4O as we observe for our $MoCl_4O$, i.e., a selective growth on alkali-containing substrates. A difference between the WCl_4O and our system is that the WO_3 films obtained on La_2O_3 and Al_2O_3 contained almost as much chlorine as tungsten. However, this may be connected with that O_3 was not used together with water in the prior study. Moreover, a very recent work studying ALE of W utilizes WCl_6 in combination with O_2 or O_3 to form volatile WCl_4O/WCl_2O_2 in order to etch a W surface[47] and thus the reversed chemistry. Here, thermodynamic modeling reveals that the formation of gaseous WCl_4O or WCl_2O_2 from WCl_6 and WO_3 is favorable at ≥200 °C.

Our study is not the first successful usage of oxychlorides as an ALD precursor. *In situ* generated $NbOCl_3$ has been reported to deposit Nb_2O_5 in combination with water.[48] This was revealed as the probable reason why $NbCl_5$ and water yielded Nb_2O_5 films with large gradients along the flow direction. $NbOCl_3$ was generated from $NbCl_5$ being pulsed into the chamber and reacting with the already present Nb_2O_5 film, thus etching the film. Based on our current findings, we expect that $NbOCl_3$ would work as a precursor for deposition of Nb_2O_5 also when used directly. A similar etching process as observed for $NbCl_5$ on Nb_2O_5 has also been seen for $TaCl_5$ on Ta_2O_5 but less thoroughly investigated.[49]

The XRD investigations show that the type of crystalline phases depends on the deposition temperature, ranging from Mo_9O_{26} (P 2/c) at 250 °C to an XRD amorphous phase at 275 °C and MoO_2 at 300 °C. The average oxidation state of Mo in Mo_9O_{26} is 5.8+, e.g., almost 6+. XPS studies performed on a sample deposited at 300 °C shows that 6+ is the dominant valence of Mo in that sample also. This is in contrast with XRD peaks of MoO_2 for the same sample, where the oxidation state for Mo is 4+. We therefore believe the film mainly consists of an amorphous MoO_3 matrix with embedded crystalline MoO_2 islands, when deposited at 300 °C. The fact that MoO_2 is formed only at high temperatures is consistent with how the equilibrium constant, K, changes as a function of temperature for the reaction in Eq. (3),

$$MoO_3(s) + MoCl_4O(g) \rightarrow MoO_2(s) + MoCl_2O_2(g) + Cl_2(g). \quad (3)$$

Here, K is $6.6 \cdot 10^{-5}$, $9.1 \cdot 10^{-4}$, and $7.9 \cdot 10^{-3}$ at 200, 250, and 300 °C, respectively, proving a two order magnitude change with temperature, suggesting why we observe MoO_2 only at high temperatures.

The growth rate of our $MoCl_4O + (H_2O + O_3)$ system showed a sudden increase from 0.13 to 0.71 Å/cycle for 1000 cycles when the deposition temperature was increased from 275 to 300 °C. Such a high thermal sensitivity of the growth rate point at a thermally activated process, such as solid-state diffusion, where exponential dependency of diffusion rate with temperature is expected.

An unusual trait of this ALD process is that the growth rate per cycle is not constant as a function of number of cycles, i.e., on the thickness of the deposited film. The growth rate slows down when the number of cycles is increased and the film becomes thicker. This means that we do not enter a typical steady-state ALD situation where the entire surface is saturated and the material deposits on itself, but rather a situation where a longer distance to the interface of the substrate limits the growth.

Studies of growth rates versus purge lengths and a nonlinear relationship between the thickness of the deposited film and number of ALD cycles suggest that the growth is limited by diffusion of Li^+/Na^+ ions through the film and that the presence of alkali ions is essential for film growth. The fact that soda-lime glass facilitates growth, but silica does not, also supports this. The XPS depth profile of film deposited on glass does show sodium throughout the entire film, proving that diffusion of sodium has taken place. Since Na_2CO_3, Li_3PO_3, and Li_2SiO_3 coated substrates did not induce film growth, the alkali ion cannot be in any arbitrary matrix. The Na_2CO_3, Li_3PO_3, and Li_2SiO_3 were all expected to be terminated by a thin carbonate layer on its surface. A possible denominator is if these carbonate layers themselves lack the feature to initiate $MoCl_4O + (O_3 + H_2O)$ growth. A more thorough understanding of the growth mechanisms will be a topic for more focused studies.

Also, the SEM micrographs of our thin films deposited on glass and LiF show a grainier appearance and do not cover the surface in an optimal manner when grown on LiF. This suggests that the nucleation may be more favorable on glass than LiF, despite the near equal measured growth rate.

The selectivity of our system is near perfect for glass over Si (100) with a native oxide layer. This is to the best of our knowledge also the first report of selective area atomic layer deposition of any molybdenum containing compound. Moreover, it is indeed extreme that the selectivity retained even for as much as 1000 cycles. It is rare that a system exhibits selectivity over so many cycles, as 250 cycles is typically reported as the maximum number of cycles before extra measures, such as etching steps, are required.[27]

Taking the extreme selectivity into account, this work has thoroughly studied the possible MoO_x growth on Si(100). As all data from EDS, SEM, and XPS point to the same conclusion, that MoO_x does not growth on Si(100) using $MoCl_4O + (O_3 + H_2O)$ at temperatures of 300 °C or less, we have confidence in that the system indeed is perfectly selective within this temperature range.

IV. SUMMARY AND CONCLUSIONS

We have reported on the use of the novel precursor $MoCl_4O$ for deposition of various molybdenum oxides with ALD using deposition temperatures between 200 and 350 °C. The highest growth rate was 0.72 Å/cycle when deposited on soda-lime glass at 300 °C. The $MoCl_4O + (H_2O + O_3)$ process is clearly dependent on the chemistry of the substrate. It shows highly area-selective growth when deposited on substrates containing available lithium or sodium, only growing on glass and LiF and not on Li_3PO_3, $CaCO_3$, Na_2CO_3, Si(100) with a native oxide layer, or silica. Moreover, the system is perfectly selective as measured by EDS for glass over Si (100) with a native oxide layer in the temperature range of 200–300 °C. XPS analysis showed a large presence of sodium in the film deposited on glass and likewise lithium in the film deposited on LiF. This presence of mobile Li^+/Na^+ is most likely the key feature of the nucleation and growth and opens for deposition of patterned structures of molybdenum oxides.

ACKNOWLEDGMENTS

The authors would like to acknowledge the Research Council of Norway for financing this work through the TRALALALA project within the ENERGIX program (No. 244087, Julie Nitsche Kvalvik and Per-Anders Hansen) and the Norwegian Micro- and Nano-Fabrication Facility, NorFab (No. 245963, Jon Borgersen). Furthermore, the authors would like to thank Kristian B. Kvamme, Amund Ruud, and Kjetil Almaas for providing substrates and Kristian Weibye for performing the XPS measurements.

REFERENCES

[1]B. Wu and A. Kumar, J. Vac. Sci. Technol. B **25**, 1743 (2007).
[2]R. Chen, H. Kim, P. C. McIntyre, D. W. Porter, and S. F. Bent, Appl. Phys. Lett. **86**, 191910 (2005).
[3]R. Clark, K. Tapily, K.-H. Yu, T. Hakamata, S. Consiglio, D. O'Meara, C. Wajda, J. Smith, and G. Leusink, APL Mater. **6**, 058203 (2018).
[4]L. Casagrande, L. Lietti, I. Nova, P. Forzatti, and A. Baiker, Appl. Catal. B **22**, 63 (1999).
[5]J. Sonnemans and P. Mars, J. Catal. **31**, 209 (1973).
[6]H. Chang, Q. Wu, T. Zhang, M. Li, X. Sun, J. Li, L. Duan, and J. Hao, Environ. Sci. Technol. **49**, 12388 (2015).
[7]O. M. Hussain and K. S. Rao, Mater. Chem. Phys. **80**, 638 (2003).
[8]M. S. Go, J.-M. Song, C. Kim, J. Lee, J. Kim, and M. J. Lee, Electron. Mater. Lett. **11**, 252 (2015).
[9]C. Zollfrank, K. Gutbrod, P. Wechsler, and J. P. Guggenbichler, Mater. Sci. Eng. C **32**, 47 (2012).
[10]Y. Liu, Y. Lv, Z. Tang, L. He, and X. Liu, Electrochim. Acta **189**, 184 (2016).
[11]U. K. Sen and S. Mitra, RSC Adv. **2**, 11123 (2012).
[12]Y. Jin, H. Wang, J. Li, X. Yue, Y. Han, P. K. Shen, and Y. Cui, Adv. Mater. **28**, 3785 (2016).
[13]V. Guidi, G. Carlo Cardinali, L. Dori, G. Faglia, M. Ferroni, G. Martinelli, P. Nelli, and G. Sberveglieri, Sens. Actuators B Chem. **49**, 88 (1998).
[14]D. Zhao, J. Qin, L. Zheng, and M. Cao, Chem. Mater. **28**, 4180 (2016).
[15]S. K. Deb and J. A. Chopoorian, J. Appl. Phys. **37**, 4818 (1966).
[16]P. F. Carcia and E. M. McCarron, Thin Solid Films **155**, 53 (1987).
[17]C. Julien, A. Khelfa, O. M. Hussain, and G. A. Nazri, J. Cryst. Growth **156**, 235 (1995).
[18]R. M. Guerrero, J. R. V. Garcia, V. Santes, and E. Gomez, J. Alloys Compd. **434**, 701 (2007).
[19]M. Diskus, O. Nilsen, and H. Fjellvag, J. Mater. Chem. **21**, 705 (2011).
[20]C. E. Nanayakkara, A. Vega, G. Liu, C. L. Dezelah, R. K. Kanjolia, and Y. J. Chabal, Chem. Mater. **28**, 8591 (2016).
[21]T. L. Drake and P. C. Stair, J. Vac. Sci. Technol. A **34**, 051403 (2016).
[22]T. Jurca, A. W. Peters, A. R. Mouat, O. K. Farha, J. T. Hupp, T. L. Lohr, M. Delferro, and T. J. Marks, Dalton Trans. **46**, 1172 (2017).
[23]A. Bertuch, G. Sundaram, M. Saly, D. Moser, and R. Kanjolia, J. Vac. Sci. Technol. A **32**, 01A119 (2014).
[24]M. F. J. Vos, B. Macco, N. F. W. Thissen, A. A. Bol, and W. M. M. Kessels, J. Vac. Sci. Technol. A **34**, 01A103 (2016).
[25]K. Bergum, A. Magraso, H. Fjellvag, and O. Nilsen, J. Mater. Chem. A **2**, 18463 (2014).
[26]A. J. M. Mackus, A. A. Bol, and W. M. M. Kessels, Nanoscale **6**, 10941 (2014).
[27]G. N. Parsons, J. Vac. Sci. Technol. A **37**, 020911 (2019).
[28]J. A. Singh, N. F. W. Thissen, W.-H. Kim, H. Johnson, W. M. M. Kessels, A. A. Bol, S. F. Bent, and A. J. M. Mackus, Chem. Mater. **30**, 663 (2018).
[29]A. Mameli, M. J. M. Merkx, B. Karasulu, F. Roozeboom, W. M. M. Kessels, and A. J. M. Mackus, ACS Nano **11**, 9303 (2017).
[30]E. K. Seo, J. W. Lee, H. M. Sung-Suh, and M. M. Sung, Chem. Mater. **16**, 1878 (2004).
[31]I. Zyulkov, V. Madhiwala, E. Voronina, M. Snelgrove, J. Bogan, R. O'Connor, S. De Gendt, and S. Armini, ACS Appl. Mater. Interfaces **12**, 4678 (2020).
[32]Z. Zhang, T. Dwyer, S. M. Sirard, and J. G. Ekerdt, J. Vac. Sci. Technol. A **37**, 020905 (2019).
[33]F. S. Minaye Hashemi, C. Prasittichai, and S. F. Bent, ACS Nano **9**, 8710 (2015).
[34]J. N. Kvalvik, K. B. Kvamme, K. Almaas, A. Ruud, H. H. Sønsteby, and O. Nilsen, "LiF by atomic layer deposition - made easy," J. Vac. Sci. Technol. A (submitted).
[35]O. Nilsen, H. Fjellvåg, and A. Kjekshus, Thin Solid Films **450**, 240 (2004).
[36]Ø. S. Fjellvåg, *Tynne filmer og nanobelter for batterier: Syntese og karakterisering av katodematerialer for litium- og natriumionbatterier* (University of Oslo, Oslo, Norway, 2014).
[37]A. Ruud, V. Miikkulainen, K. Mizohata, H. Fjellvåg, and O. Nilsen, J. Vac. Sci. Technol. A **35**, 01B133 (2017).
[38]A. Magneli, Acta Cryst. **6**, 495 (1953).
[39]O. Bertrand, P. Dufour, N. Floquet, and L. C. Dufoue, Phys. Status Solidi A **71**, 511 (1982).
[40]M. Diskus, O. Nilsen, H. Fjellvåg, S. Diplas, P. Beato, C. Harvey, E. Lantman, and B. Weckhuysen, J. Vac. Sci. Technol. A **30**, 01A107 (2012).
[41]Ø. S. Fjellvåg, A. Ruud, H. H. Sønsteby, O. Nilsen, and H. Fjellvåg, Cryst. Growth Des. **20**, 3861–3866 (2020).
[42]H. Gruber and E. Krautz, Phys. Satus Solidi A **62**, 615 (1980).
[43]T. Leisegang, A. A. Levin, J. Walter, and D. C. Meyer, Cryst. Res. Technol. **40**, 95 (2005).
[44]J. G. Choi and L. T. Thompson, Appl. Surf. Sci. **93**, 143 (1996).
[45]A. Fick, Ann. Phys. **170**, 59 (1855).
[46]"Tungsten and molybdenum tetrachloride oxides," in *Inorganic Syntheses* (John Wiley & Sons, Inc., New York, 1980), pp. 195–199.
[47]W. Xie and G. N. Parsons, J. Vac. Sci. Technol. A **38**, 022605 (2020).
[48]K. Knapas, A. Rahtu, and M. Ritala, Chem. Vap. Depos. **15**, 269 (2009).
[49]J. Aarik, A. Aidla, K. Kukli, and T. Uustare, J. Cryst. Growth **144**, 116 (1994).
[50]See supplementary material at http://dx.doi.org/10.1116/6.0000219 for (1) measured film thicknesses before and after deposition of MoO_x at 300 °C, (2) measured at.% from EDS used for selectivity calculations and (3) modelling of thickness vs number of cycles.

Supporting information for **Area-selective atomic layer deposition of molybdenum oxide**

Julie Nitsche Kvalvik[1], Jon Borgersen[2], Per-Anders Hansen[1] and Ola Nilsen[1*]

[1] Centre for materials science and nanotechnology, Department of Chemistry, University of Oslo, Postboks 1033, Blindern, 0315 OSLO, Norway
[2] Centre for materials science and nanotechnology, Department of Physics, University of Oslo, Postboks 1048, Blindern, 0315 OSLO, Norway

[a)] Electronic mail: ola.nilsen@kjemi.uio.no

1. Thicknesses before and after MoO_x deposition at 300 °C

Film thicknesses as measured with spectroscopic ellipsometry before and after a standard deposition at 300 °C are listed in Table I.

Table I. Thicknesses of films before and after deposition of MoO_x at 300 °C, using 1000 cycles.

Substrate	Film thickness before deposition (nm)	Film thickness after deposition (nm)
Glass	-	72.3
LiF	45.5	114.2
Si(100)	2.3 (native oxide layer)	3.0
$CaCO_3$	52.2	54.0
Na_2CO_3	73.4	72.1
Li_3PO_3	88.6	90.1
Silica	-	Not able to measure any film

2. Measured at.% from EDS used for selectivity calculations

The measured amounts of Mo and Si on glass and Si(100) by EDS with the measured fraction covered by nuclei, θ, for films deposited at 350 °C using 1000 cycles, Table II. Both glass substrate and the Si(100) substrates are from the same ALD-run.

Table II. Amounts of Mo and Si measured on desired and undesired growth area used to calculate the selectivity at 350 °C for 1000 cycles.

	On glass, surface 1, desired growth area	On Si(100), surface 2, undesired growth area
Measured amount of Mo by EDS (at. %)	8.5	1.2
Measured amount of Si by EDS (at. %)	26.7	46.2
θ	0.317	0.026

3. Modelling of thickness vs number of cycles

We have attempted two approaches based on Fick's laws of diffusion to model the film thickness as function of number of cycles. We assume that the growth is proportional to the amount of activation agent at the surface, here Li or Na. The absolute values of the constants fitted has not been the main objective, but rather the overall shape of the curved.

The first assumes a constant concentration of activation agent at source, here the substrate surface, where the concentration at given distance, x, and time, t, can be expressed by:

$$n\,(x,t) = n_0 erfc\left(\frac{x}{\sqrt{Dt}}\right) \quad (1)$$

where n is the concentration, n_0 is the concentration at the interface between the glass substrate and the film, erfc is the complementary error function, x is the distance from the glass/ film interface i.e. film thickness, D is the diffusivity constant and t is the time in number of cycles.

The second approach assumes a finite amount of activation agent at source. The concentration at given distance, x, and time, t, can be expressed by:

$$n(x,t) = \frac{N}{\sqrt{4\pi Dt}} e^{-x^2(4Dt)} \quad (2)$$

where N is the amount of activation agent at source at x=0 and the other factors are the same as for Equation 1. Figure 1 shows the modelled values for the thickness as a function of number of cycles using either Equation 1 (blue) or Equation 2 (grey) in comparison to the real measured data (orange dots). Equation 2 provides the best fit, however, the experimental variation is larger than the difference between the two models, and hence no significant conclusion can be drawn.

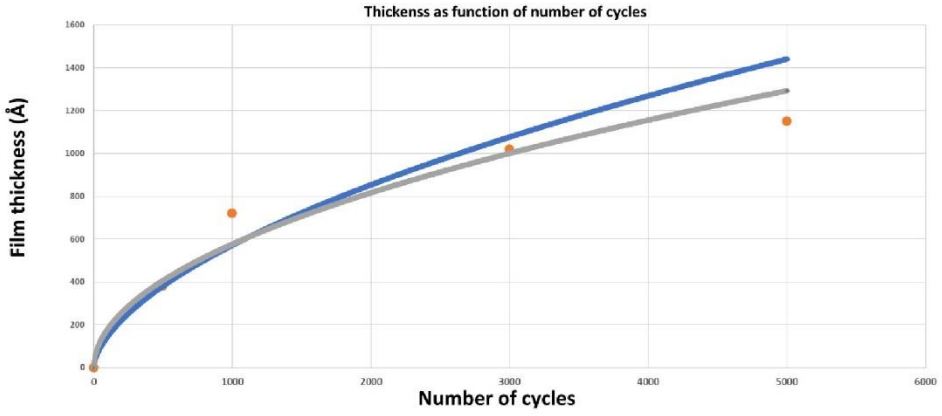

Figure 1. Modelled values for thickness as a function of number of cycles using a constant source approach (blue) and thin film slab approach (grey). The actual measured values are shown in orange.

II

Paper II

Design of experiments approach to luminescent $CaMoO_4$ by atomic layer deposition

Kvalvik, J.N, Hansen, P.-A. and Nilsen, O. Journal of Vacuum Science & Technology A **38**, 052408 (2020)

JVST A
Journal of Vacuum Science & Technology A

ARTICLE

avs.scitation.org/journal/jva

Design of experiments approach to luminescent $CaMoO_4$ by atomic layer deposition

Cite as: J. Vac. Sci. Technol. A 38, 052408 (2020); doi: 10.1116/6.0000327
Submitted: 12 May 2020 · Accepted: 30 July 2020 ·
Published Online: 20 August 2020

Julie Nitsche Kvalvik, Per-Anders Hansen, and Ola Nilsen[a)]

AFFILIATIONS

Centre for Materials Science and Nanotechnology, Department of Chemistry, University of Oslo, Postboks 1033, Blindern, 0315 Oslo, Norway

Note: This paper is part of the 2021 Special Topic Collection on Atomic Layer Deposition (ALD).
[a)]**Electronic mail:** ola.nilsen@kjemi.uio.no

ABSTRACT

Atomic layer deposition (ALD) is evolving beyond binary compounds to complex oxides and doped structures, taking advantage of the nanometer precision ALD provides. In practice, the development of complex ALD-processes usually means performing many ALD-runs, as success at first attempt is unlikely. One factor at a time methods, where only one factor is altered and the rest are kept constant, are most often chosen due to their intuitive communication of control. However, they do have several drawbacks, being slow, neglecting secondary effects, and are usually not randomized—meaning that errors that arise over time can easily be overlooked. We here dig into our statistical toolbox and show how design of experiments (DoE) can be used to efficiently develop an ALD-process to deposit crystalline, luminescent $CaMoO_4$—a proposed material for optoelectronic applications, like light emitting diodes or as a host for solar down-converters. Using DoE enables screening for a wider range of deposition temperatures, pulsed composition, and annealing parameters, by only performing nine ALD-runs in our case. We moreover look into how these parameters affect crystallinity, composition, and the photoluminescence properties and use DoE to show which factors have the greatest effects on these properties. The work also lays out the basic theory of the DoE-field and how to implement DoE in developing ALD-processes, in general, to ease the usage of DoE for the ALD-community.

I. INTRODUCTION

Complex oxides are gaining importance in numerous fields from luminescence,[1,2] catalysis, and enabling oxide based electronics.[3,4] However, synthesis of such materials adds a level of complexity. This is particularly true for deposition by atomic layer deposition (ALD), where there is not necessarily a direct correlation between the pulsed and deposited compositions.[4] Also, optimizing the deposition temperature can be challenging. The ideal starting scenario, if the aim is to develop a novel ternary ALD-process, is that their binary processes have overlapping temperature ranges where they exhibit ALD-growth (ALD-windows). This is not a strict criterion, however, as ALD-windows do change when binary systems are used in combination for ternary or even quaternary processes.[5]

Traditionally, new complex ALD processes have been developed using one factor at a time (OFAT) methods.[6] This means that, for example, the deposition temperature has been altered stepwise, while the other parameters, for example, the pulsing ratio between the components, pulsing and purging times, etc., have been kept constant. Thus, OFAT approaches require a large number of experiments, as the various factors are probed sequentially. In addition, interaction effects may be overlooked, such as how the required pulsing times vary with the deposition temperature. Moreover, OFAT processes are not intrinsically randomized and do, therefore, not reveal errors that arise over time, like developing leaks or clogs. The well-trained experimentalist should of course know that the experiments should be randomized, but we often see that this is not the case in practice, particularly for exploratory experiments where the boundaries are not known in advance, such as temperature range, times, etc.

The weaknesses of OFAT methods can be overcome by performing screening and optimizing using a design of experiments (DoE) framework. DoE applies statistics not only when analyzing the measured data but also to set up the experiments themselves. By changing several factors at a time in a pre-determined and

randomized order, a maximum amount of information is retrieved from a given number of experiments. Since the order of the experiments is randomized, the residuals, namely, the difference between the obtained and predicted value, can be plotted as a function of time to reveal errors that arise over time.

The concept of DoE was first proposed in 1935.[7] Today, Plackett–Burman designs are widely used as screening designs for processes with many factors,[8] whereas various response surface methodologies (RSMs)[9] such as central composite designs (CCDs)[10] are used for optimizations. When using RSM, the existence of a response surface modeled with polynomials with at least two variables is postulated. A measured response for an ALD-system could, for example, be the growth per cycle (GPC). The variables used to model the response surface are termed input or predictor variables. The input variables represent the variables that can be changed between the experiments, such as the deposition temperature or pulse length in an ALD-experiment.

Considering what powerful and relatively easy to use tool DoE is, the extent it is being used in materials science today is surprisingly limited. This is probably related to that it requires some additional knowledge of statics beyond the basics. It also comes with the psychological barrier of giving a computer program the power of deciding your experiments. A program that on overall feels a bit like the black box we researchers typically do not like to relate to. However, in reality, it is still researcher's job to decide on the investigated experimental region and the data density and distribution within it, even when DoE is used. In fact, DoE forces the researcher to plan carefully in advance of performing the experimental series, which reduces the risk of failed experiments and, thus, time and resources.

DoE has been used in the development of electrospinning processes,[11] chemical vapor deposition of carbon nano-tubes,[12] and very recently in a work using synthesis of oleylamine-capped gold nanoparticles as a case study of how DoE can be implemented in nanoparticle synthesis.[13] However, using the DoE methodology is definitely the exception rather than the rule. There are a few examples of DoE being used in the ALD-community. Two factorial central composite designs have been used to map how the film thickness and annealing time of both amorphous TiO_2 (Ref. 14) and ZnO (Ref. 15) affect the optical properties. Moreover, DoE has been used to optimize the sheet resistance of TiN films deposited by plasma enhanced ALD using a full factorial DoE-experiment.[16] The input variables used there were the plasma duration, purge time, and the flows of N_2 and H_2.

We here show how DoE, more specifically a CCD-optimization, can be used to develop an ALD-process for the deposition of the ternary oxide $CaMoO_4$ and guide how similar ALD-challenges can be overcome by clever usage of DoE. $CaMoO_4$ shows interesting optical properties similar to other molybdates and tungstates with the tetragonal Scheelite-structure is proposed as a host material for down-conversion thin films for solar cells. $CaMoO_4$ absorbs UV-light well but is transparent for lower energy photons, while it is easily doped with various lanthanides, making this material a suitable host for down-converting thin films (see the supplementary material[44] for UV-VIS specter of $CaMoO_4$). An important aspect with $CaMoO_4$ and other scheelites is that their intervalence charge transfer states (IVCTs) are high as compared to, for example, vanadates, tungstates, or niobates.[17–22] This is important for the proposed use as a host for down-conversion thin films since it makes it less likely that the host material itself will induce quenching of the excited lanthanides dopants through the IVCT state. However, present synthesis routes do not facilitate making sufficiently high-quality $CaMoO_4$ thin films,[23–27] especially for further doping of the host matrix. ALD is an ideal method for such tasks and making $CaMoO_4$ by ALD should be possible by combining known processes for the deposition of CaO (Ref. 28) and MoO_3.[29] Another argument for why ALD is particularly useful is that it enables control of where the lanthanide dopants are placed in the host matrix, which, in turn, affect the energy transfer and thus luminescence properties, if indeed used as a down-converter on a later stage.

28 shows that $Ca(thd)_2$ (thd = 2,2,6,6-tetramethyl-3,5-heptanedione) + O_3 process yields CaO when deposited at 350 °C, but $CaCO_3$ at 250 °C, also without a CO_2 pulse. In general, β-diketonates, such as $Ca(thd)_2$, are well suited as ALD-precursors, especially at higher deposition temperatures or in combination with O_3.[30] $Ca(thd)_2$ has also been used to deposit $La_{1-x}Ca_xMnO_3$.[5]

The Mo-precursor used, namely, $MoCl_4O$, is much less investigated as an ALD-precursor. The availability of Mo-precursors that both are able to sustain temperatures above 195 °C [adequate sublimation of $Ca(thd)_2$] and work with conventional thermal ALD is very limited. In fact, the only other known option is $(N^tBu)_2(NMe_2)_2Mo$[31] but requires heating and inert handling. $MoCl_4O$ was chosen based on our recent experience with its sufficient vapor pressure at room temperature and use as a precursor to form MoO_x, although in a selective area process.[29]

Here, the pulsing ratio between $Ca(thd)_2$ and $MoCl_4O$, the deposition temperature, the annealing temperature, and annealing time are used as input variables, and the composition measured by energy-dispersive x-ray spectroscopy (EDS), a Pawley-refined x-ray diffraction (XRD) signal of $CaMoO_4$, and photoluminescence (PL) intensity are used as modeled response variables. Through such an analysis, we find that luminescent $CaMoO_4$ thin films can be deposited by ALD at 350 °C using 29 pulsed % of Mo precursor versus Ca precursor and that longer annealing times increase the PL signal. We further comment on how this approach can be transferred to future mapping of complex compounds by ALD.

II. EXPERIMENT

Prior to performing the CCD-experiment, a few initial trials were performed to test if the combination of the binary processes could yield $CaMoO_4$ and to give hints on the span of the input parameters. In general, to start a DoE set without some initial information is not recommended, especially when optimizations are used, as they require a process that is already somewhat established. DoE is not a quick fix for not knowing your chemistry but a tool to tune your process. The initial trials revealed a few points that helped to provide the starting point for the CCD-series:

(i) Using a pulsing ratio of 1:1 with [$MoCl_4O$ + (H_2O + O_3)] versus [$Ca(thd)_2$ + O_3], hereafter termed 1:1 of Mo:Ca, and depositing at 300 °C gave a huge surplus of molybdenum [about 80% Mo as measured by x-ray fluorescence (XRF)].

(ii) Pulsing 1:1 of Mo:Ca did not give any XRD-peaks of $CaMoO_4$.
(iii) Annealing at 1000 °C for 1 h gave rise to unwanted Si-Mo phases.
(iv) Although pulsing 1:2 or 1:3 of Mo:Ca gave a small surplus of calcium when deposited at 300 °C, it showed signs of $CaMoO_4$ in the diffractograms.

The last point in the list above attached weight to that the $MoCl_4O + (H_2O + O_3)$ and $Ca(thd)_2 + O_3$ processes indeed could be combined to form $CaMoO_4$.

The thin films were deposited by ALD using a F-120 Sat reactor (ASM Microchemistry). Si(100) wafers with a 2 nm thick native oxide layer were used as substrates. The deposition temperature was an input variable in the experiment and ranged from 300 to 400 °C. We hoped that increasing the deposition temperature to 400 °C would aid crystallization during deposition. N_2 from gas cylinders (Praxair, 99.999%), passing through a Mykrolis purifier, was used as a purging gas with a flow rate of 300 $cm^3\ min^{-1}$. A background pressure was maintained at 2.7 mbar. The depositions were carried out using the β-diketonate chelate $Ca(thd)_2$ (Strem, 97%) as the Ca-source, $MoCl_4O$ (Sigma-Aldrich, 97%) as the Mo-source, O_3 as an O-source after the $Ca(thd)_2$ pulse, and distilled H_2O and O_3 pulsed simultaneously as the O-source after the $MoCl_4O$-pulse. O_3 was supplied from a In USA ozone generator (AC-2505), which delivers mass 15% O_3 in O_2, using O_2 from a gas cylinder (Praxair, 99.8%). Pulsing and purging times for the various precursors were chosen based on prior experience with deposition of MoO_x (Ref. 29) and $CaCO_3$ (Ref. 28) on the same reactor and are given in Table I.

In this work, a face-centered CCD with four input variables (deposition temperature, pulsed % of Mo, annealing time, and annealing temperature) is used. Such a design with *three* input variables is visualized in Fig. 1. The star points are placed on the surfaces of the interaction cube where each direction represents the level of an input variable. The input variables are coded within this cube to range between −1 and 1, in order to be dimensionless and directly comparable with each other. For example, if the deposition temperature is varied between 200 and 300 °C, −1 is 200 °C, 0 is 250 °C, and 1 is 300 °C. The star points are placed a distance α from the center. The value of α should be chosen with care. It is typically settled after defining the factorial points, which define the range and also the center point. Note that $1 < \alpha$ generates experiments outside the range of the factorial points. A small α gives a larger data density close to the center point. This is beneficial when convinced that the optimum is near the center. On the other hand, the explored region will be smaller and the data density in the periphery be poor when α is small. A face centered design ($\alpha = 1$) as utilized here will not generate experiments outside the predefined ranges of the input variables. Moreover, batching is eased for face centered designs. The default value of α is usually $\sqrt{2}$, however, this may lead to experiments where α carry no physical meaning, like having a negative anneal time. The interested reader is referred to Ref. 32 for further information about CCD, where chapter 12 provides an excellent introduction to response surface methodology (RSM).

TABLE I. Standard pulsing and purging times for ALD synthesis of $CaMoO_4$.

Precursor	Pulse time (s)	Purge time (s)
$MoCl_4O$	3	3
$H_2O + O_3$	3	5
$Ca(thd)_2$	3	2
O_3	2	2

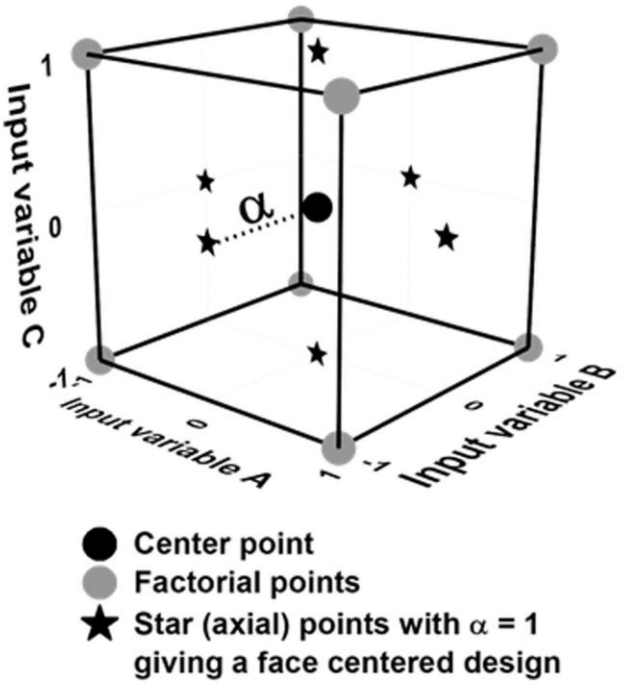

FIG. 1. Illustration of an interaction cube for a CCD with three input variables coded between −1 and 1. The design is face centered with the star points on the faces of the cube.

The pulsed composition of $MoCl_4O + (O_3 + H_2O)$ relative to the total number of cation cycles was kept between 25% and 33%, as these compositions both showed signs of $CaMoO_4$ in the diffractograms. It is further referred to as pulsed % Mo. 29 pulsed % Mo was approximated with 5 cycles of $MoCl_4O + (O_3 + H_2O)$ to 12 cycles of $Ca(thd)_2 + O_3$ with a pulsing sequence of Mo–Ca–Ca–Mo–Ca–Ca–Ca–Mo–Ca–Ca–Mo–Ca–Ca–Mo–Ca–Ca–Mo–Ca–Ca–Ca. The pulsed % Mo was also an input variable and varied according to the CCD setup. Some of the resulting films were annealed for improved crystallization and luminescence of $CaMoO_4$. The annealing time was either 15 or 30 min, and the annealing temperature was varied between 415 and 800 °C, both being input variables in the CCD setup. We chose 425 °C as the minimum annealing temperature, to span from just above the deposition temperature, and 800 °C as the maximum temperature, since it was significantly below 1000 °C, which led to formation of molybdenum

TABLE II. Overview of input variables with their ranges used in the experimental design.

Input variable	Minimum (coded −1)	Maximum (coded 1)
Deposition temperature (°C)	300	400
Pulsed % of Mo	25	33
Anneal temperature (°C)	425	800
Anneal time (min)	0	30

silicates in the initial studies. A MTI—UL Standard Compact RTP furnace utilizing halogen lamps was used for annealing. The samples were cooled rapidly after annealing. To save time and resources, the syntheses were performed in batches, as described in Table II of the supplementary material.[44] The setup of the experiments and statistical analysis were done using the MINITAB19 software with a face-centered central composite design. Table II gives an overview of the input variables used in the experimental design and their ranges. The full experimental setup as derived from MINITAB19 is given in Table I in the supplementary material.[44]

The selection of response variable(s) to study and how these should be characterized and digitized must be carefully considered prior to starting the investigations. It is all about what material and which properties are desired. If a clear goal is not defined, optimizing a process is futile. Two types of data can be analyzed with MINITAB19, both qualitative data (yes/no) and quantitative data. For the further quantitative statistical analysis, it is vital to have data that convey actual physical, comparable information.

To retrieve structural, compositional, and photoluminescence data of the samples, which were the three responses we desired to study, XRD, EDS, and PL analyses were done on the full set of samples. XRD was performed to investigate the structure of the obtained samples, using a Bruker D8 Discovery Diffractometer, with CuKα_1 radiation and a Ge(111) monochromator in a traditional Bragg–Brentano setup. In order to quantify the XRD data in a manner more suitable for MINITAB19, Pawley refinements were performed.[33] In this manner, potential overlapping peaks from undesired phases were accounted for. In opposition to Rietveld refinements, Pawley refinements can fit diffractograms showing oriented growth, which may occur for ALD-deposited films. The refinements were done using TOPAS.v5 and the data were fitted to COD No. 9009632. Integrated intensities for (011), (112), (013), and (004) peaks were retrieved and summed, prior to loading these data into MINITAB19 for further statistical analysis. EDS was performed using a HITACHI TM3000 scanning electron microscope equipped with a Quantax70 EDS unit. An acquisition time of 1 min was used. Prior to loading the data into MINITAB for further analysis, the content of Ca versus Mo in the samples was calculated. A higher value than 1.0 here, therefore, indicates a calcium surplus. The average of three measurements from different spots was used. The PL measurements were performed using a USB2000+ modular spectrometer from Ocean Optics with a 280 nm diode as the excitation source. All PL measurements were done in one session to make the data comparable. For the CCD analysis of the PL data, the integral between 450 and 850 nm is used. Selected samples were also studied with atomic force microscopy (AFM) to get a measure of the roughness and topography. A Park Systems XE-70 AFM with a CONTSCR tip in a contact mode was used for this, and Gwyddion software was used to process the AFM micrographs. The film thicknesses and, thus, the GPC was measured by spectroscopic ellipsometry (SE) using a J. A. Woollam α-SE spectroscopic ellipsometer. The data were modeled with a Cauchy-function using the COMPLETEEASE software package. XRF was performed to probe for chlorine impurities stemming from the $MoCl_4O$-precursor and to verify the EDS-results, as XRF is considered more accurate but have stricter requirements on sample size, thus limiting our possibility to perform such analysis on the full set of samples. XRF was performed with a PANalytical Axios minerals max spectrometer equipped with OMNIAN and STRATOS softwares, and Omnian standards.

III. RESULTS AND DISCUSSION

A. Optimizing with design of experiments

All the experiments were carried out successfully as listed in Tables I–III in the supplementary material[44] and fitted to a response surface using MINITAB19. There were, however, gradients normal to the flow direction in the chamber for all the experiments yielding $CaMoO_4$. The films around 2 cm from the center of the reaction chamber were typically 50% thinner. Only samples that were centered in the reaction chamber were used for the further analysis and annealing experiments. The residuals for the various responses versus these response surfaces as a function of experiment order are given in Fig. 1 in the supplementary material.[44] As the goal of this work was to identify an ALD-route to obtain crystalline, luminescent $CaMoO_4$ thin films, MINITAB19 was used to optimize the process for two different cases.

(1) Maximize the XRD and PL signals and keep Ca:Mo closest possible to 1:1.
(2) Only maximize the PL signal.

The results of these calculations are given in Table III.

Pareto charts are typically shown when presenting DoE results, as they give an easy visualization of the effects of the various input factors,[34] here given in Fig. 2. Statistically valid effects within our desired confidence interval (95%) have values higher than 2.086 as given with the red dotted lines. For the crystallinity, the statistical analysis leaves no clear conclusions, as no terms have a statistically valid effect. That being said, the secondary effect between deposition temperature and annealing time, followed by

TABLE III. Optimization of the deposition process to maximize XRD and PL signals and keep Ca:Mo close to 1 (i) or only maximize PL signal (ii).

Process parameters	Optimized for case (i)	Optimized for case (ii)
Deposition temperature (°C)	340	349
Pulsed % Mo	30	29
Annealing temperature (°C)	686	626
Annealing time (min)	30	30

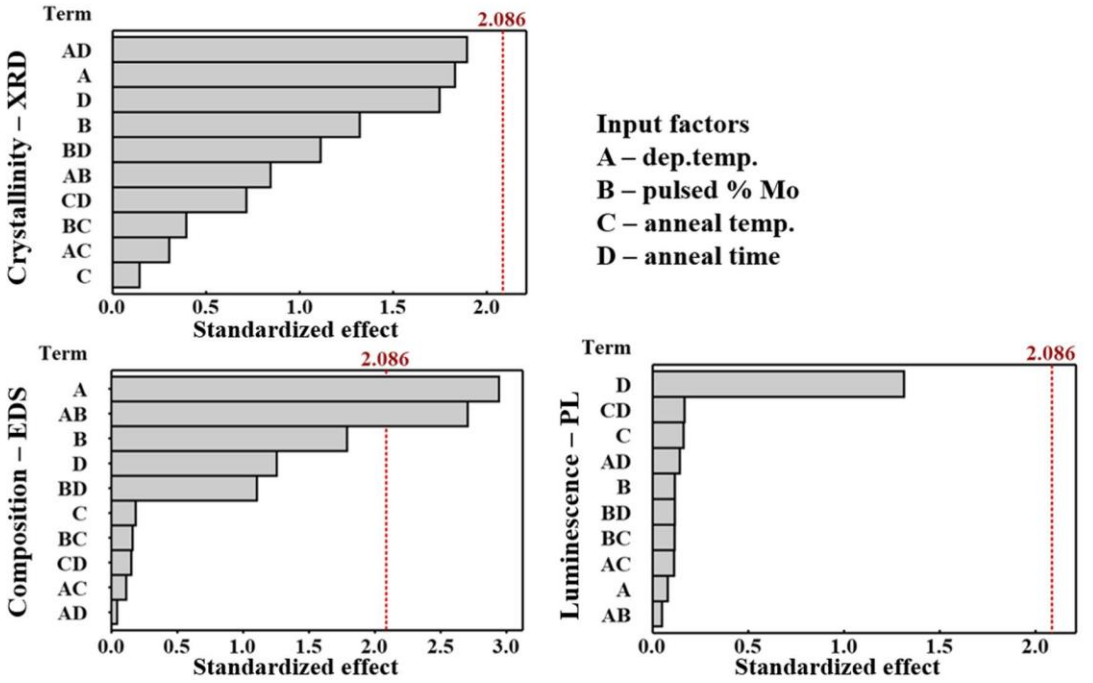

FIG. 2. Pareto charts showing the direct and secondary standardized effects of the input variables on the three responses. The dotted line at 2.086 denotes if the effects are indeed statistically significant or not. Standardized effects are unitless quantities.

these two factors alone, are the parameters closest to being significant. Surprisingly, the least significant effect is the annealing temperature, which seem to have a very limited effect on the crystallinity. This will be a topic in the discussions later. The only terms that show significance for the composition are the deposition temperature and the secondary effect between this and the pulsed percentage of Mo. The deposition temperature of any ALD process will, in turn, affect the packing density of the various precursors, both how many precursors that are available on the surface and their positions, which, in turn, affect how likely it is for $CaMoO_4$ to be deposited. Annealing, especially the annealing temperature, has a very limited effect on the composition, as expected. In like manner as with the crystallinity, no factors are statistically significant for the PL signal. However, the response is much higher for the annealing time than any of the other parameters.

Main effect plots, giving the average of all the measured responses for each level of the input variables, are also typically shown when presenting DoE data.[35] In this case, the main effect plots in Fig. 3, to a large extent paint the same picture as the optimization calculations in Table III for the ALD-deposition parameters. Both the PL and XRD signal maximize at the middle value for the pulsed % Mo (29%). Moreover, the EDS response is closest to 1 for this sample. Pulsing slightly

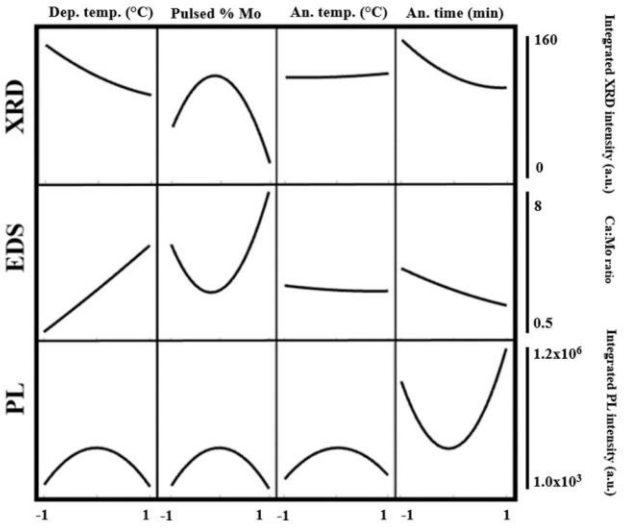

FIG. 3. Main effect plots showing mean values of all the measured responses for the various levels of the coded (−1 to 1) input parameters. The middle of each *x* axis represents coded value 0 for each input variable.

higher or lower content of Mo is according to this giving Ca-dominated thin films, more on this aspect in the discussions. For the deposition temperature, 350 °C seems to be a good compromise giving close to the correct stoichiometry, a high XRD-response and high PL-response.

Moreover, Fig. 3 shed light over the chosen annealing parameters. The composition seems nearly unaffected by annealing. The effect of annealing on the crystallinity is as seen in the Pareto charts also very limited, besides a slight decrease in XRD signal for the longer annealing times. Surprisingly, the PL values are higher for the samples that are not annealed than for the samples annealed for 15 min. We do, however, see the maximum PL values for samples that are annealed for 30 min. This suggests an ongoing crystallographic reorganization of the film where an intermediate microstructure is unfavorable for PL. The maximum mean PL values are found for an annealing temperature of 612.5 °C. All in all, the means of these experiments suggest that depositing at 350 °C with 29 pulsed % Mo, annealing at 612.5 °C for at least 30 min is a viable route to obtain crystalline, luminescent $CaMoO_4$ thin films by ALD.

B. Thin film growth and characterization

Figure 4 shows the growth rate per cycle (GPC) as a function of deposition temperature for three different pulsed % of Mo. Pulsing 25% or 33% of Mo have similar temperature dependencies on the GPCs with decreasing values from 300 to 350 °C before flattening out between 350 and 400 °C. For 29 pulsed % Mo, the GPC is increasing as a function of temperature between 300 and 400 °C. The GPC is 0.49 Å/cycle at 300 °C but is more than tripled at 400 °C where it is 1.75 Å/cycle. The differences in temperature dependencies of the growth rates for the various pulsed compositions are probably related to which materials and phases are formed for each temperature. The samples found calcium-rich by EDS also had peaks from aragonite and calcite in their diffractograms. As the mean value plots of the EDS measurements in Fig. 3 suggest that samples deposited with both 25 and 33 pulsed % Mo are more calcium rich than the ones deposited with 29 pulsed % Mo. This indicates that the GPC of $CaMoO_4$ is increasing as a function of temperature for this system, whereas deposition of $CaCO_3$ shows the opposite tendency.

Figure 5 compares the XRD diffractograms obtained for films deposited by 29% pulsed Mo at various deposition temperatures. At 300 °C peaks from $CaMoO_3$, the 113-peak from calcite and a broad possible 104-peak from $CaMoO_4$ are found. At 350 °C, the $CaMoO_3$ peaks vanish but a sharp 104-calcite peak arise. Note that this 104-calcite peak is not seen for the samples deposited at 350 °C using 29 pulsed % Mo, that are also annealed, not consistent with an unaffected stoichiometry with annealing. At 400 °C, only peaks from $CaMoO_4$ are found. This is supported by the PL raw data given in Table I in the supplementary material,[44] as the sample deposited at 400 °C using 29% pulsed Mo is the most luminescent as deposited. It is, though, less luminescent than the samples deposited at 350 °C and annealed for 30 min.

Although the growth rate showed different temperature dependencies, there were several general trends for growth of these thin films, one being that the crystallite sizes ranged between 30 and 40 nm for the samples containing crystalline $CaMoO_4$ with a film thickness of ca. 120 nm. As many of the samples were similar with respect to both topography, photoluminescence, and crystallinity, PL, XRD, SEM, and AFM data for a selected sample are compiled in Fig. 6. The selected sample was deposited at 350 °C using 29 pulsed % Mo and was annealed at 612.5 °C for 15 min. It, thus,

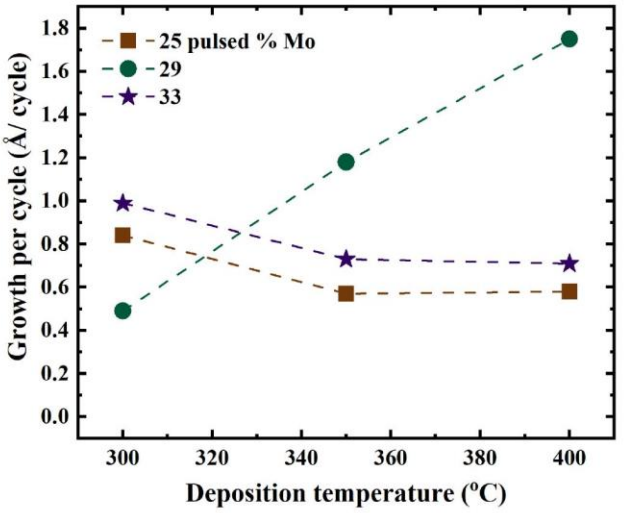

FIG. 4. GPC for $CaMoO_4$ for the various pulsed amounts of Mo vs Ca precursor as a function of deposition temperature.

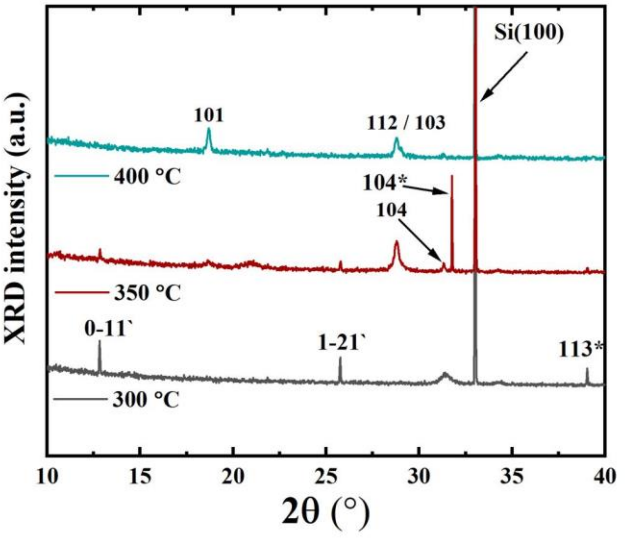

FIG. 5. XRD diffractograms for samples deposited with 29 pulsed % Mo at various deposition temperatures. Indexes marked with * refers to calcite, ` refers to $CaMoO_3$, and no markings refers to the desired $CaMoO_4$ phase.

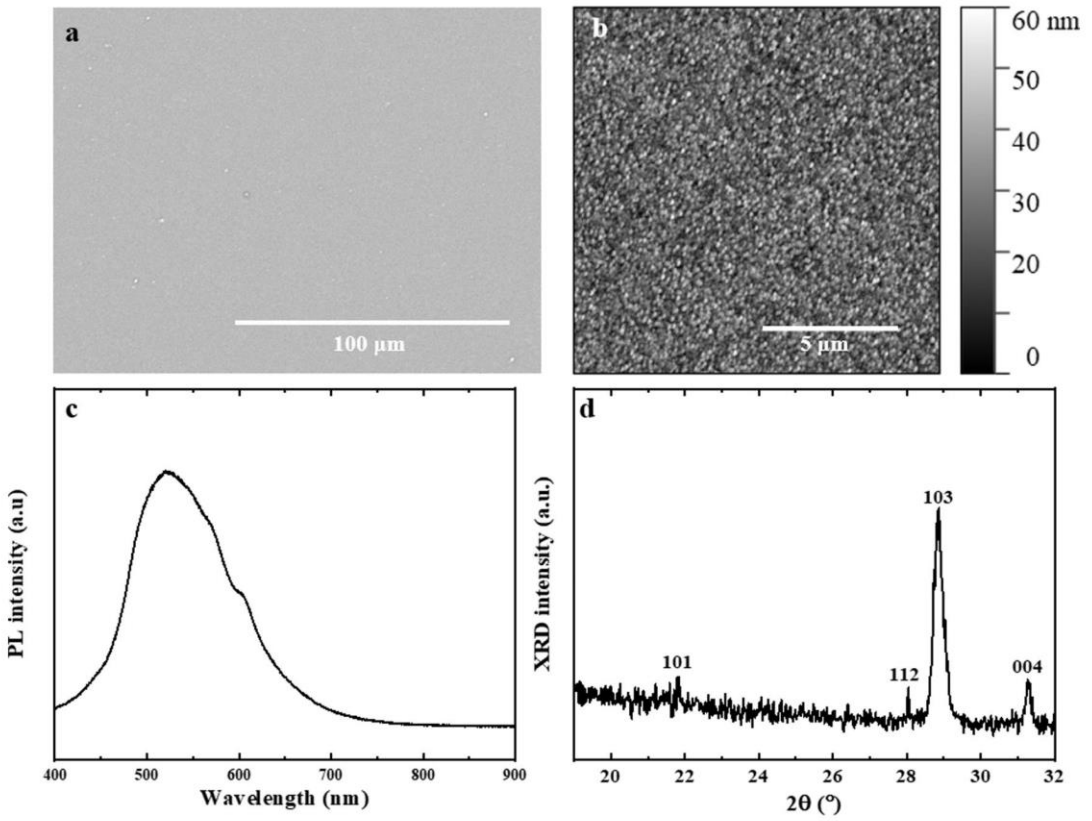

FIG. 6. SEM micrograph (a), AFM micrograph (b), PL spectrum (c), and XRD diffractogram (d) of a sample deposited at 350 °C using 29 pulsed % of Mo and annealed for 15 min at 612.5 °C. The film thickness was measured to be 114.4 nm by spectroscopic ellipsometry.

represents the center point of our imaginary interaction space in the CCD setup.

AFM was used to measure the roughness and topography of selected samples. The roughnesses together with relevant sample information are listed in Table IV. It reveals RMS roughnesses range between 8.9 and 20.0 nm for samples deposited at 350 °C using 29 pulsed % Mo. Annealing does not seem to affect the roughness significantly, but the two samples with the lowest roughness are the ones annealed longest or at the highest temperature. Compared with the crystallite sizes retrieved from Pawley refinements, the RMS roughness is about half of the estimated crystallite size.

XRF analysis was performed on selected samples. Table V shows XRF data for a sample deposited at 350 °C using 29 pulsed % Mo. The measurement was performed prior to annealing. The chlorine content was below 1.5% in all measured samples. The XRF measurements all show a similar over-stoichiometry in this range for Mo, contrary to the EDS measurements.

TABLE IV. RMS roughness and relevant sample parameters for a selection of $CaMoO_4$ thin films deposited simultaneously at 350 °C using 29 pulsed % of Mo vs Ca but with different annealing parameters.

Film thickness (nm)	RMS roughness (nm)	Anneal time (min)	Anneal temperature (°C)
121.8	18.0	0	–
124.2	20.0	15	425
129.3	8.9	15	800
114.4	16.0	15	612.5
135.3	14.3	30	612.5

TABLE V. Mol. % of Mo, Ca, and Cl for a $CaMoO_4$ sample deposited at 350 °C using 29 pulsed % of Mo vs Ca measured by XRF prior to annealing.

Element	Mol. %
Mo	54.1
Ca	45.2
Cl	0.7

C. Discussion

Performing this CCD-experiment enabled us to find a synthesis route to fabricate photoluminescent, crystalline $CaMoO_4$ thin films by ALD—which was the main target of this work. Based on a few initial tests, we investigated a fairly narrow range in pulsed composition but a wider range of deposition temperatures and annealing conditions. An alternative approach to CCD could have been to perform an initial screening design, such as a wide range two-level Plackett–Burman design, especially of pulsed composition. In practice, this would have led to not performing the most successful experiments here, and may not have increased the knowledge of the system significantly. The initial tests proved to be a sufficient starting ground for this CCD-optimization, although the methodology was originally developed for a much simpler system where competitive products do not form to the same degree. Taking into account that the center point of the CCD-setup was replicated six times and that a few experiments had no annealing and, thus, were similar, a total of 21 different combinations of the four input factors have been tried. This was done using only nine ALD-runs and annealing in six batches. A significantly larger set of samples and experiments would have been required using the OFAT approach. More importantly, OFAT will in general not lead to the optimum condition if there is a correlation between the input parameters,[36] meaning that the optimum condition may not have been found at all if we had used OFAT here. We estimate that the number of ALD-runs would easily exceeded 20 for a process like this to be developed without DoE.

29 pulsed % Mo was the pulsed composition that yielded the most luminescent films and also the highest XRD-signal. Moreover, the temperature dependency was different for this pulsed composition than 25 or 33 pulsed % Mo, where 29 pulsed % Mo increase with temperature and the others decrease. This dependency with GPC, in combination with the gradients along the sides of the reaction chamber, suggests that the process is very sensitive toward the pulsed composition. We believe that the deposited composition is different on the sides of the reaction chamber due to fluid dynamics. The fact that the pulsing sequence for 29 pulsed % Mo actually consists of two Mo–Ca–Ca–Ca (= 25 pulsed % Mo) and three Mo–Ca–Ca (= 33 pulsed % Mo) units underlines this sensitivity further. We are surprised of this extreme sensitivity toward the pulsing composition, providing excess Ca on both sides of 29 pulsed % Mo. However, the randomized sequence of depositions moreover support that this extreme sensitivity toward pulsed composition is indeed a real effect. We expect that deviations from ideal composition will lead to formation of the slower growing $CaCO_3$, and that we grow $CaMoO_4$ in the center of the reaction chamber but more $CaCO_3$ to the sides. The GPC of $CaCO_3$ using $Ca(thd)_2$ and O_3 is reported as 0.45 Å/cycle at 300 °C and decreases to around 0.40 Å/cycle at 400 °C.[28] This decrease is less than what we see in the present dataset but may account for some of it.

We have recently reported the $MoCl_4O + (H_2O + O_3)$ process which grows selectively on LiF and conventional glass substrates[29] but show no signs of growth on $CaCO_3$ and Si(100) substrates among others. The MoO_x films deposited on LiF and glass had significant concentrations of Li^+ and Na^+, respectively, and we, therefore, believe that the growth of these films is limited by diffusion from the substrates. In the current work, calcium seems to also play a role since a high content of Mo was indeed possible, even though prior experiments has shown that a significant deposition of MoO_x was not possible on $CaCO_3$. This may be one piece to the puzzle for explaining the high sensitivity for growth with the pulsed composition we observe in this work. Any deviations from an ideal composition may lead to etching through formation of volatile molybdenum oxochlorides.[29]

There is an obvious discrepancy between the composition measured by XRF and EDS. The EDS measurements suggest a significant over-stoichiometry of Ca for most samples. Re-measuring a sample that by EDS is measured to have 66% Ca versus (Mo + Ca) gives around 45% Ca by XRF. The XRF results are closer to the desired one to one stoichiometry between Ca and Mo. One difference between those measurement methods is the size of the volume being measured, where XRF measures the entire volume of the mounted sample and EDS is measuring a much more limited interaction volume.[37] In general, XRF is regarded to have a significantly higher precision[38] and we, therefore, believe that the over-stoichiometry of Ca may be less pronounced than suggested from the EDS data. The quantification of the EDS data may also suffer from the fact that the largest signal came from the Si-substrate since the electron penetration depth was longer than the film thickness.

The effect of annealing time on the crystallinity and photoluminescence were somewhat surprising, as annealing for 15 min yielded less luminescent films than not annealing at all or annealing for 30 min. Furthermore, the films became less XRD-crystalline with longer annealing times. This may be due to clustering of defects in the films or decomposition of the films leading to formation of $CaCO_3$ and reactions between Mo and the Si-substrate to form Mo-Si phases such as Mo_5Si_3.[39]

In general, the literature shows a huge divergence in annealing conditions for synthesis of $CaMoO_4$, ranging from heating the samples at 900 °C for 2 h[40] to 200 °C for 2 h.[27] The latter work also found that heating at 600 °C for 10 min is giving less luminescent films than heating at 200 °C for 2 h, which is contradicting our findings where 612.5 °C provides highly luminescent films. This divergence in published literature is yet another reason why CCD has been very useful here, as it allows for trying many combinations of annealing times and temperatures with few experiments.

The origin of the green luminescence at room temperature for Scheelite-structured molybdates is still disputed in the literature. It is suggested to stem from both oxygen deficient complexes,[41] defect centers with oxygen interstitials.[42] For the similar $CaWO_4$, it is suggested to stem from distorted WO_4-tetrahedra due to oxygen.[43] It is also more recently shown that more disorder leads to a higher luminescence at room temperature.[27] This is consistent with our findings visualized in Fig. 3—that even if the crystallinity is slightly decreased for the samples annealed for the longest times, the PL signal still increases significantly.

IV. SUMMARY AND CONCLUSIONS

A route for deposition of luminescent $CaMoO_4$ by ALD was successfully developed using a DoE-approach, using $MoCl_4O$, $Ca(thd)_2$, O_3, and H_2O as precursors. The optimization suggests that

depositing at 349 °C with 29% pulsed Mo and annealing at 626 °C for 30 min yields the most luminescent films. The growth is highly sensitive to the pulsed composition, and the actual run closest to the optimum used 29 pulsed % Mo at a deposition temperature of 350 °C, providing a growth rate of 1.2 Å/cycle. This work shows how DoE can be used to slash the number of required experiments to obtain a route for deposition of complex materials by ALD and provides a starting ground for further similar developments.

ACKNOWLEDGMENTS

The authors are deeply grateful to statistician Øystein Evandt for his support and input on the DoE-sections of this paper. David Wragg is also thanked for his insight into Pawley refinements. Moreover, the authors would like to acknowledge the Research Council of Norway for financing this work through the TRALALALA project (Project No. 244087) within the ENERGIX program.

REFERENCES

[1]M. Getz, P.-A. Hansen, M. A. K. Ahmed, H. Fjellvåg, and O. Nilsen, Dalton Trans. **46**, 3008 (2017).
[2]M. N. Getz, O. Nilsen, and P.-A. Hansen, Sci. Rep. **9**, 10247 (2019).
[3]J. E. Bratvold, H. H. Sønsteby, O. Nilsen, and H. Fjellvåg, J. Vac. Sci. Technol. A **37**, 021502 (2019).
[4]H. H. Sønsteby, H. Fjellvåg, and O. Nilsen, Adv. Mater. Interfaces **4**, 1600903 (2017).
[5]O. Nilsen, M. Lie, H. F. Fjellvåg, and A. Kjekshus, in *Growth of Oxides with Complex Stoichiometry by the ALD Technique, Exemplified by Growth of* $La_{1-x}Ca_xMnO_3$, *in Rare Earth Oxide Thin Films*, edited by M. Fanciulli and G. Scarel (Springer Berlin Heidelberg, Berlin, 2007), pp. 87–100.
[6]V. Czitrom, Am. Statistician **53**, 126 (1999).
[7]F. Yates, Biometrics **20**, 307 (1964).
[8]R. L. Plackett and J. P. Burman, Biometrika **33**, 305 (1946).
[9]N. R. Draper, in *Introduction to Box and Wilson (1951) on the Experimental Attainment of Optimum Conditions, in Breakthroughs in Statistics*, Springer Series in Statistics (Perspectives in Statistics), edited by S. Kotz and N. L. Johnson (Springer New York, New York, NY, 1992), pp. 267–269.
[10]G. Box and D. Behnken, Technometrics **2**, 455 (1960).
[11]S. R. Coles, D. K. Jacobs, J. O. Meredith, G. Barker, A. J. Clark, K. Kirwan, J. Stanger, and N. Tucker, Appl. Polym. Sci. **117**, 2251 (2010).
[12]A. Nourbakhsh, B. Ganjipour, M. Zahedifar, and E. Arzi, Nanotechnology **18**, 115715 (2007).
[13]F. Niamh Mac, Y. Ye, Q. Runzhang, G. Federico, and G. Stefan, e-print ChemRxiv (2019).
[14]D. M. King, X. Du, A. S. Cavanagh, and A. W. Weimer, Nanotechnology **19**, 445401 (2008).
[15]D. M. King, S. I. Johnson, J. Li, X. Du, X. Liang, and A. W. Weime, Nanotechnology **20**, 195401 (2009).
[16]M. Burke, A. Blake, I. M. Povey, M. Schmidt, N. Petkov, P. Carolan, and A. J. Quinn, J. Vac. Sci. Technol. A **32**, 031506 (2014).
[17]E. Cavalli, P. Boutinaud, R. Mahiou, M. Bettinelli, and P. Dorenbos, Inorg. Chem. **49**, 4916 (2010).
[18]E. Cavalli, P. Boutinaud, and M. Grinberg, J. Lumin. **169**, 450 (2016).
[19]P. Boutinaud, E. Pinel, M. Oubaha, R. Mahiou, E. Cavalli, and M. Bettinelli, Opt. Mater. **28**, 9 (2006).
[20]P. Boutinaud, R. Mahiou, E. Cavalli, and M. Bettinelli, J. Appl. Phys. **96**, 4923 (2004).
[21]P. Boutinaud, R. Mahiou, E. Cavalli, and M. Bettinelli, Chem. Phys. Lett. **418**, 185 (2006).
[22]P. Boutinaud, R. Mahiou, E. Cavalli, and M. Bettinelli, J. Lumin. **122–123**, 430 (2007).
[23]X. Li, Z. Yang, L. Guan, J. Guo, Y. Wang, and Q. Guo, J. Alloys Compd. **478**, 684 (2009).
[24]J. H. Ryu, J.-W. Yoon, C. S. Lim, W.-C. Oh, and K. B. Shim, J. Alloys Compd. **390**, 245 (2005).
[25]W. S. Cho, M. Yashima, M. Kakihana, A. Kudo, T. Sakata, and M. Yoshimura, J. Am. Ceram. Soc. **80**, 765 (1997).
[26]L. Zhu, Y. Mao, Q. Chen, Y. Zou, X. Shen, and G. Liao, J. Mater. Sci. Mater. Electron. **30**, 3639 (2019).
[27]A. P. de Azevedo Marques, V. M. Longo, D. M. A. de Melo, P. S. Pizani, E. R. Leite, J. A. Varela, and E. Longo, J. Solid State Chem. **181**, 1249 (2008).
[28]O. Nilsen, H. Fjellvåg, and A. Kjekshus, Thin Solid Films **450**, 240 (2004).
[29]J. N. Kvalvik, J. Borgersen, P.-A. Hansen, and O. Nilsen, J. Vac. Sci. Technol. A **38**, 042406 (2020).
[30]M. Putkonen and L. Niinistö, "Organometallic precursors for atomic layer deposition," in *Precursor Chemistry of Advanced Materials*, edited by R. A. Fischer (Springer Berlin Heidelberg, Berlin, 2005), pp. 125–145.
[31]A. Bertuch, G. Sundaram, M. Saly, D. Moser, and R. Kanjolia, J. Vac. Sci. Technol. A **32**, 01A119 (2014).
[32]K. Hinkelmann and O. Kempthorne, *Introduction to Experimental Design. Design and Analysis of Experiments* (John Wiley & Sons, Hoboken, NJ, 2008).
[33]G. S. Pawley, J. Appl. Crystallogr. **14**, 357 (1981).
[34]K. K. Sawant, V. P. Mundada, and V. J. Patel, J. Nanomed. Nanotechnol. **8**, 1000442 (2017).
[35]Á. Kukovecz, D. Méhn, E. Nemes-Nagy, R. Szabó, and I. Kiricsi, Carbon **43**, 2842 (2005).
[36]B. Cao, L. A. Adutwum, A. O. Oliynyk, E. J. Luber, B. C. Olsen, A. Mar, and J. M. Buriak, ACS Nano **12**, 7434 (2018).
[37]J. I. Goldstein, D. E. Newbury, J. R. Michael, N. W. Ritchie, J. H. J. Scott, and D. C. Joy, *Scanning Electron Microscopy and X-ray Microanalysis* (Springer New York, New York, 2017), p. 12.
[38]G. R. Lachance and F. Claisse, *Quantitative X-ray Fluorescence Analysis Theory and Application* (John Wiley & Sons, Hoboken, NJ, 1995), p. 7.
[39]C. L. Fu, X. Wang, Y. Y. Ye, and K. M. Ho, Intermetallics **7**, 179 (1999).
[40]E. Cavalli, F. Angiuli, P. Boutinaud, and R. Mahiou, J. Solid State Chem. **185**, 136 (2012).
[41]E. V. Sokolenko, V. M. Zhukovskii, E. S. Buyanova, and Y. A. Krasnobaev, Inorg. Mater. **34**, 499 (1998).
[42]T. Hara, Mater. Chem. Phys. **91**, 243 (2005).
[43]B. M. Sinelkov, E. V. Sokolenko, and V. Y. Zvekov, Inorg. Mater. **32**, 999 (1996).
[44]See the supplementary material at https://doi.org/10.1116/6.0000327 for experimental setup and order, batching of ALD syntheses and annealing experiments, residuals vs experiment order and UV-VIS spectra of CaMoO4 on silica as deposited.

Supplementary material for **A Design of Experiments approach to luminescent $CaMoO_4$ by Atomic Layer Deposition**

Julie Nitsche Kvalvik[1], Per-Anders Hansen[1] and Ola Nilsen[1, a]

[1]Centre for materials science and nanotechnology, Department of Chemistry, University of Oslo, Postboks 1033, Blindern, 0315 OSLO, Norway

a) Electronic mail: ola.nilsen@kjemi.uio.no

1. Experimental setup as retrieved from Minitab, including the measured responses

Supp. Table I below shows the experimental setup as retrieved from MiniTab19 with input variables and measured responses.

Supp. Table I. Overview of experiments (called «runs» by Minitab19) performed in the CCD setup using deposition temperature, pulsed % Mo, annealing temperature and annealing time and the measured responses. The temperatures shown here are in °C. "StdOrder" refers to the starting order of the experiment. The experiment is not blocked (that is, running similar experiments sequentially), explaining why the block-column is 1 for all experiments.

StdOrder	RunOrder	Blocks	Deposition temp. (°C)	Pulsed % Mo	Anneal temp. (°C)	Anneal time (min)	XRD int. $CaMoO_4$	EDS response (Ca:Mo)	PL int. $CaMoO_4$
5	1	1	300	25	800	0	183.859	5.88	47668
12	2	1	400	33	425	30	0	1000	5942
8	3	1	400	33	800	0	6.2	1000	7751
14	4	1	400	25	800	30	70.517	1.8	665878
29	5	1	350	29	612.5	15	112.186	1.49	1526360
6	6	1	400	25	800	0	24.109	7.26	58471
16	7	1	400	33	800	30	0	1000	33934
21	8	1	350	29	425	15	80.1	2	1661070
13	9	1	300	25	800	30	0.482	1.9	2580340
10	10	1	400	25	425	30	31.036	2.11	128739
27	11	1	350	29	612.5	15	70.462	2.13	944621
11	12	1	300	33	425	30	13.36	4.38	238333
30	13	1	350	29	612.5	15	38.02	2.46	485424
23	14	1	350	29	612.5	0	72.858	1.97	437206
17	15	1	300	29	612.5	15	145.134	1.6	276256
18	16	1	400	29	612.5	15	49.704	1.65	1482610
31	17	1	350	29	612.5	15	98.884	1.43	1991080
19	18	1	350	25	612.5	15	18.008	11.38	646808
3	19	1	300	33	425	0	39.507	3.92	18650

24	20	1	350	29	612.5	30	132.129	1.5	24886510
2	21	1	400	25	425	0	24.109	7.26	58571
7	22	1	300	33	800	0	39.507	3.92	18650
1	23	1	300	25	425	0	183.859	5.88	47668
26	24	1	350	29	612.5	15	54.331	2.12	421476
28	25	1	350	29	612.5	15	80.11	2.2	2190520
15	26	1	300	33	800	30	44.031	1.9	744724
20	27	1	350	33	612.5	15	52.885	0.77	819232
22	28	1	350	29	800	15	105.859	1.3	1760980
9	29	1	300	25	425	30	0.482	1.51	203457
4	30	1	400	33	425	0	72.858	1000	7751
25	31	1	350	29	612.5	15	104.706	1.69	1693550

2. ALD synthesis batches

To save time and resources, samples with the same deposition temperature and the same pulsed % Mo, were synthesized as a batch. There were nine batches in total, labelled a-j (Supp. Table II).

Supp. Table II. Batching of samples with the same ALD-deposition parameters.

Batch label	Samples included in batch (RunOrder from MiniTab)	Starting order	Dep.temp. (°C)	puls % Mo
a	1, 9,23,29	1	300	25
b	2, 3, 7, 30	4	400	33
d	5, 8, 11, 13, 14, 17, 20, 24, 25, 28, 31	9	350	33
e	4, 6, 10, 21	2	400	25
f	12, 19, 22, 26	3	300	33
g	15	5	300	29
h	16	6	400	29
i	18	7	350	25
j	27	8	350	33

3. Annealing batches

To save time and resources, samples with the same annealing parameters, where annealed simultaneously. There were five batches in total, labelled K-P. The order of the experiments are derived from starting order given from MiniTab shown in Supp. Table III.

Supp. Table III. Batching of samples with the same annealing parameters.

Annealing starting order	**Sample ID**	**Time (min)**	**Temperature**	**ALD synthesis batch**	**Annealing program (batch)**
1	JNK_CCD-a-1	30	425	a	K
2	JNK_CCD-e-2	30	425	e	K
3	JNK_CCD-f-3	30	425	f	K
4	JNK_CCD-b-4	30	425	b	K
5	JNK_CCD-a-5	30	800	a	L
6	JNK_CCD-e-6	30	800	e	L
7	JNK_CCD-f-7	30	800	f	L
8	JNK_CCD-b-8	30	800	b	L
9	JNK_CCD-g-9	15	612.5	g	M
10	JNK_CCD-h-10	15	612.5	h	M
11	JNK_CCD-i-11	15	612.5	i	M
12	JNK_CCD-j-12	15	612.5	j	M
13	JNK_CCD-d-13	15	425	d	N
14	JNK_CCD-d-14	15	800	d	O
15	JNK_CCD-d-15	30	612.5	d	P
16	JNK_CCD-d-16	15	612.5	d	M

17	JNK_CCD-d-17	15	612.5	d	M
18	JNK_CCD-d-18	15	612.5	d	M
19	JNK_CCD-d-19	15	612.5	d	M
20	JNK_CCD-d-20	15	612.5	d	M
21	JNK_CCD-d-21	15	612.5	d	M
22	JNK_CCD-d-22	15	612.5	d	M

4. Residuals vs. experiment order

Supp. Figure 1 shows that there was no correlation between the residuals between the response surface and the actual observations and the experiment order, indicating that there were no errors arising over time.

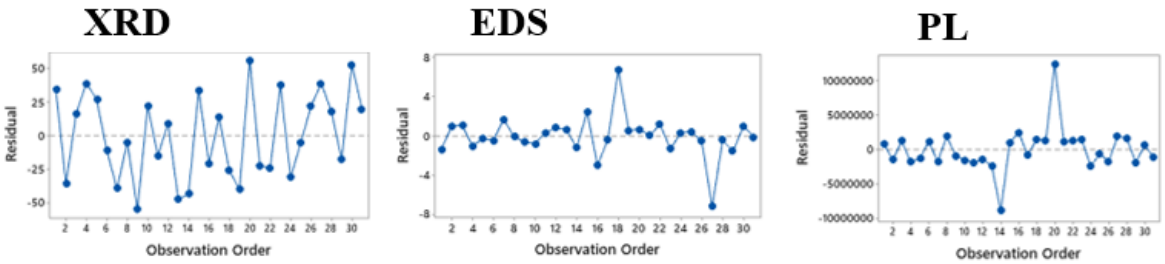

Supp. Figure 6. Residuals between the response surface and the actual observations vs experiment number (=observation order) for the XRD, EDS and PL responses.

5. UV-VIS of $CaMoO_4$ on silica as deposited

Supp. Figure 2 shows a UV-VIS spectrum of $CaMoO_4$ on silica. The film is deposited with 29 pulsed % Mo at 350 °C, but is not annealed.

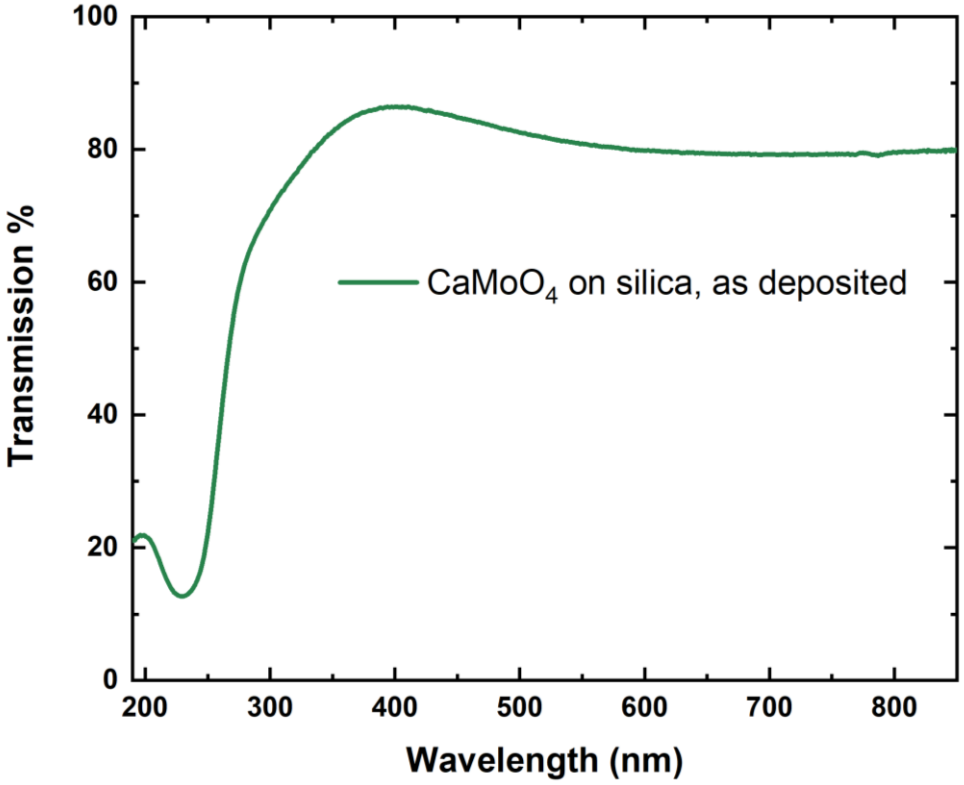

Supp. Figure 7.UV-VIS spectrum of $CaMoO_4$ deposited at 350 °C using 29 pulsed % Mo on silica. No post annealing is performed, as the silica substrate would not have been able to withstand this heat treatment.